MASTERS BY RESEARCH

Investigating the relationship between tidal range power plant size and hydrodynamic impact

Roome, Edward

Award date:
2024

Awarding institution:
Bangor University

PRIFYSGOL
BANGOR
UNIVERSITY

Investigating the relationship between tidal range power plant size and hydrodynamic impact

A thesis submitted to fulfill the requirements of a Master of Science by Research (MScRes)

By Edward Roome

Supervisors: Dr Peter Robins and Dr Martin Austin

School of Ocean Sciences, Menai Bridge, LL59 5AB, UK

Declaration

I hereby declare that this thesis is the results of my own investigations, except where otherwise stated. All other sources are acknowledged by bibliographic references. This work has not previously been accepted in substance for any degree and is not being concurrently submitted in candidature for any degree unless, as agreed by the University, for approved dual awards.

Yr wyf drwy hyn yn datgan mai canlyniad fy ymchwil fy hun yw'r thesis hwn, ac eithrio lle nodir yn wahanol. Caiff ffynonellau eraill eu cydnabod gan droednodiadau yn rhoi cyfeiriadau eglur. Nid yw sylwedd y gwaith hwn wedi cael ei dderbyn o'r blaen ar gyfer unrhyw radd, ac nid yw'n cael ei gyflwyno ar yr un pryd mewn ymgeisiaeth am unrhyw radd oni bai ei fod, fel y cytunwyd gan y Brifysgol, am gymwysterau deuol cymeradwy

E. Roome

Acknowledgements

I would like to thank my supervisors Peter Robins and Martin Austin for their time, knowledge and support during this project. I also thank Simon Neill, his knowledge and expertise in the field of marine renewable energy was invaluable to the success of this project. I am grateful for the assistance provided by Nick Hanousek (Cardiff University) and Bin Guo (National Oceanography Centre, Liverpool); without this collaboration, implementing the chosen methodology would not have been possible. I also thank Alan Davies for conceptualising the project and providing insights into numerical modelling of the North Wales region.

Abstract

Over the past decade, renewable energy initiatives have been widely adopted and integrated into national electricity grids, with solar and wind technologies experiencing exponential growth. To sustainably transition to a carbon-free energy system, nations must build resilient and robust electricity grids from diverse sources of renewable energy. In the UK, tidal range energy holds the potential to predictably and reliably supply an estimated 12% of annual electricity demand. However, converting tidal range energy involves constructing and operating large-scale coastal structures (tidal lagoons or barrages), these structures will redefine near and far-field hydrodynamics and morphodynamics. The relationship between these impacts and the physical characteristics of tidal lagoons (e.g. impoundment surface area) is not trivial, nor is it well understood. In this study, we establish a fully-validated two-dimensional (depth-averaged) shelf-scale TELEMAC tidal model. Six potential lagoon scenarios were simulated, each involving a North Wales-based lagoon design of varying impoundment area (25 - 150 km^2). Far-field modifications to the amplitude of the semi-diurnal constituents exhibited a strong linear relationship with impoundment area and volume (correlation coefficient $R = 0.95$ and $R = 0.96$, respectively). In the case of the largest tidal lagoon (150 km^2), these changes produced a maximum water level increase in the far-field ($2 < \eta_{max} < 3$ cm, in the western Irish Sea) and a reduction in the near-field ($\eta_{max} > -3$ cm, in the eastern Irish Sea and Bristol Channel). Tidal current speeds (and bed shear stresses) were reduced to the west of the structure (resulting in trivial changes to the tidal stream resource), owing to the structures ability to impede on the eastward progression of the tidal wave. We found that the 125 km^2 tidal lagoon uniquely interacts with the diurnal and overtide constituents (O_1, K_1 and M_4), and resulted in a reduction in far-field maximum water levels (but amplifying local levels) – a consideration for future tidal range developments in the region. Reflecting on the correlation between impounded water volume and far-field hydrodynamic changes, our results suggest that, through strategic site selection and embankment placement, future tidal range scheme impact studies should seek to minimise the impounded water volume in order to reduce far-field hydrodynamic impacts, at no cost to power generation.

Contents

Chapter 1

Journal Article

1.1 Introduction

Countries currently face an energy trilemma – ensuring a secure supply of affordable electricity amid a rising demand (Newell et al. 2019) and geopolitical uncertainty (e.g. the Russia-Ukraine war; Benton et al. 2022), whilst mitigating anthropogenic climate change by implementing a low carbon emission future (Ramanathan & Feng 2008). Under international treaty, many nations have agreed to decarbonise their energy systems; if done successfully, this will involve exploiting diverse sources of renewable energy (Shmelev & Van Den Bergh 2016; Borthwick 2016; these justifications are elaborated in the Supplementary Material Section 2.1). Amongst these, tidal range energy offers some nations, including the UK, France, Canada, Australia and Argentina, a vast and untapped resource (25,880 TWh, globally[1]) that is variable throughout the tidal and lunar cycles but, importantly, predictable for decades into the future (Neill et al. 2018). Globally, around 520 MW of ocean renewable energy is currently installed, tidal range contributes 500 MW (Neill et al. 2018), considerably larger than tidal stream which stands at 10 MW (Neill 2024; further discussed in the Supplementary Material Section 2.3.2).

In regions of large tidal range (mean $>$ 5 m; Etemadi et al. 2011), a tidal range power plant is deemed viable and can harness the potential energy stored within the vertical movement of the tide. The plant operates by creating an artificial tidal phase difference (i.e. a hydraulic head) between an impounded water body and the ocean. Sluice gates manage basin water level, and gravity-driven flow through hydroelectric turbines generates electricity, the operation of tidal rang power plants is discussed in detail in the Supplementary Material Section 2.3.1. Globally, there are four operational tidal range power plants, located in

[1]The majority of the tidal range resource is distributed among eleven countries.

France, Korea, Russia and China (Neill et al. 2018)[2], each uses a *barrage* type impoundment perimeter which stretches across an estuary. Alternatively the impoundment can extend along a coastline, or be located offshore, these concepts are referred to as *coastal* or *offshore* tidal lagoons, respectively (Waters & Aggidis 2016*a*). No operational tidal lagoons exist, but they are popular amongst recent tidal range scheme (TRS) proposals, despite their higher (levelised) cost relative to tidal barrages (Waters & Aggidis 2016*b*; Supplementary Material Section 2.3.3). This is primarily because tidal lagoons can be positioned to occupy less valuable ecological space, they are therefore considered to be environmentally benign, relative to tidal barrages (Xia et al. 2010).

Much of Britain's west coast, namely the Bristol Channel/Severn Estuary and eastern Irish Sea, experiences a large tidal range – the Severn Estuary has a tidal range in excess of 12 m at Avonmouth, the second largest globally (Neill et al. 2018). Hence, the United Kingdom's (UK) shelf seas harbour 13% of the global tidal range resource (Neill et al. 2018). In the UK, the development of various TRS proposals has been considered during the past 100 years, particularly in the Severn Estuary (Langston et al. 2010). Because the UK's capacity to generate carbon-free electricity will have to double by 2050 (to achieve the net zero emissions target; Waters & Aggidis 2016*a*), TRS proposals have received a recent surge of attention from industry (NWTE 2013), academia and government (Hendry 2017). It is estimated that the UK's theoretical tidal range resource could supply 12% of annual electricity demand (based on 25 GW of installed capacity; *Wave and Tidal Energy: Part of the UK's Energy Mix* n.d.). However, despite the general success of tidal range projects abroad (e.g. the La Rance Tidal Power Station in France; Frau 1993), the UK is yet to deploy a TRS; the main barriers to development have been capital cost and concerns regarding environmental impact.

Even a modest sized tidal lagoon will impound an area of around 10 km^2. Hence, due to the periodic diversion of such large volumes of water through the sluice gates and hydroelectric turbines, tidal lagoons will redefine local and far-field water levels and flow patterns (Vouriot et al. 2019; Mackie et al. 2021). As a large-scale coastal structure, a TRS modifies the location of the coastline, redefining basin morphology

[2]The Annapolis Royal Tidal Power Station was closed in 2019.

which impedes on macro-tidal processes, resulting in far-reaching impacts on tidal amplitudes. In constricted coastal inlets (i.e. estuaries), the blockage ratio of a TRS increases (a barrage has a 100% blockage ratio at standing). High blockage ratios are associated with significant hydro-environmental impacts which can be exacerbated by the combined operation of proximal TRS (e.g. Mackie et al. 2021; Guo 2022). By altering residence time and mixing rates, tidal lagoons can impact water properties (e.g. salinity and dissolved oxygen) and the advection of substances (e.g. suspended sediments, nutrients, pathogens and pollutants; Evans & Langley 2017). This has implications for the population and distribution of marine organisms, some of which may fail to rapidly adjust to new food web dynamics; a consequence of their specific adaptation to current conditions (Baker et al. 2020). Uncertainty around the magnitude and extent of these hydro-environmental impacts remains one of the main barriers to developing a tidal lagoon project (Elliott et al. 2018; further discussed in the Supplementary Material Section 2.4.2).

Through the application of hydrodynamic modelling, the design parameters of tidal range projects can be assessed and optimised to minimise hydro-environmental impacts (e.g. Cornett et al. 2013), or to maximise electricity generation and usage (e.g. Xue et al. 2021; Zhang et al. 2022). Researchers have investigated the hydro-environmental response to changes in the shape, size (Cornett et al. 2013), location (Mackie et al. 2021), operational mode (Xia et al. 2010) and turbine/sluice arrangement of TRSs (Leech & Ahmadian 2023). However, the unique nature of coastal systems makes the generic application of these results difficult (Pethick et al. 2009). Assessments of individual TRS are required to optimise parameters and ascertain hydro-environmental impacts prior to construction. To the authors knowledge, the relationship between impoundment size and hydro-environmental impact is yet to be characterised for a tidal lagoon on the coast of Britain.

This study addresses the following research gaps:

1. Understanding the sensitivity of mesoscale (10-100 km) hydrodynamic response to tidal lagoon impoundment size.

2. Expanding on (1), we examine the nature of the relationship between impoundment size and hydrodynamic impact for each scenario.

3. Expanding on (1), we examine the impacts of the tidal lagoons on the amplitude of the principle tidal harmonics and their relationship to the tidal lagoon characteristics across far-field and near-field regions. Additional research gaps in this field are explored in the Supplementary Material Section 2.4.3.

1.2 North Wales Tidal Lagoon Site

The North Wales coast is an attractive location for a tidal lagoon for the following reasons: the region experiences a high tidal range[3] (Fig. 1.1), deep waters are found adjacent to a shallow region – favourable for siting hydro-electric turbines and cost-effective embankment construction[4] (NWTE 2013), and opportunities for grid connection. The Colwyn Bay Tidal Lagoon, proposed by North Wales Tidal Energy (NWTE 2013), is the only publicly-available industry-proposed tidal lagoon along the coast of North Wales. However, academics have conducted hydro-environmental assessments for various tidal lagoon designs which have not been proposed by industry (Mackie et al. 2021; shown in the Supplementary Material Section 2.5).

Along the North Wales coast, tidal conditions strongly influence shoreline stability, the risk of coastal flooding, biogeochemical pathways, pollution dispersal and sediment transport (Davies et al. 2023). Tidally-driven currents support a variety of pelagic and benthic habitats, from turbid water columns and bedrock outcrops in the region of the Anglesey turbidity maxima (Bowers et al. 2002), to relatively quiescent regions in which vast mudflats have developed, or subtidal sandbank features (e.g. Constable Bank, described in detail by Davies et al. 2023 and shown in Fig. 1.11). Turbidity maximas are regions of enhanced suspended sediment concentrations, these nutrient dense, productive, regions hold economical importance as nursery areas for marine species. The sensitivity of these environments in respect to tidal lagoon size is yet to be assessed for the North Wales region. In this study, we investigate the impact of impoundment surface area A_s (at mean sea level; MSL) by modelling six tidal lagoons (where A_s ranges from 25-150 km^2); each

[3]At Llandudno, the average neap and spring tidal range is 3.77 m and 7.20 m, respectively (BODC 2017)

[4]Due to the high costs associated with building an embankment in water depths >25 m (Neill et al. 2018)

tidal lagoon is scale-variation of the tidal lagoon proposed by North Wales Tidal Energy (NWTE 2013). The eastern Irish Sea is a relatively shallow region, with a mean water depth of 30 m and several estuaries (which contribute 70% of the total riverine input; Dabrowski & Hartnett 2008). The region of Liverpool Bay receives the largest input of freshwater in the Irish Sea, density-driven residual currents modelled by Polton et al. (2011) peak at 0.1 ms^{-1} – an order of magnitude smaller than those generated by the astronomical tides (Davies et al. 2023). The tidal wave, which is dominated by the M_2 and S_2 constituents, propagates northwards into the Irish Sea from the Celtic Sea; tidal current speeds often exceeding 2 ms^{-1} during spring tides around headlands and through straits (e.g. NW coast of Anglesey and Menai Strait; Robinson 1979; Howarth 2005). Because of the decreased propagation speed c of the tidal wave in shallow water ($c = \sqrt{gh}$), the distance from the Celtic Sea to Liverpool Bay and the wavelength of the semi-diurnal tide – the M_2 harmonic is in near-resonance with the northeast Irish Sea. Therefore, large M_2 amplitudes are observed across the region (e.g. Mersey and Solway Firth; Fig. 1.1). In the eastern Irish Sea, the reduced water depth induces strong non-linear effects and tidal friction which generate the M_4 harmonic (the first harmonic of M_2). When combined with M_2, a flood dominant tidal regime arises (Horrillo-Caraballo et al. 2021); the short-duration flood phase exhibits current velocities 1.2 times greater than the longer ebb phase (Brown et al. 2016). The North Wales coastline is generally sheltered from swell waves (generated in the Atlantic and propagating through the Celtic Sea), however the coastline is exposed to infrequent wind wave events from the north (Neill 2023). The theoretical foundations of these processes are further described in the Supplementary Material Section 2.2.

Across the region, the activities of various economically important industries (e.g. aquaculture, fisheries and marine energy, Fig. 1.1), populated areas (e.g. Colwyn Bay, Llandudno and Liverpool) and infrastructure (e.g. coastal rail and road transport links) are sensitive to changes in tidal conditions (further explored in the Supplementary Material Section 2.5.2). Low coastal relief and a 10-20 mm annual erosion rate (due to an eastward net drift of sediment; Davies et al. 2023) enhances the risk of tidally-driven coastal flooding (evident by the extensive history of flood events from Colwyn Bay to Rhos-on-Sea; Lyddon et al. 2015). The most recent report from the Intergovernmental Panel on Climate Change advises that sea

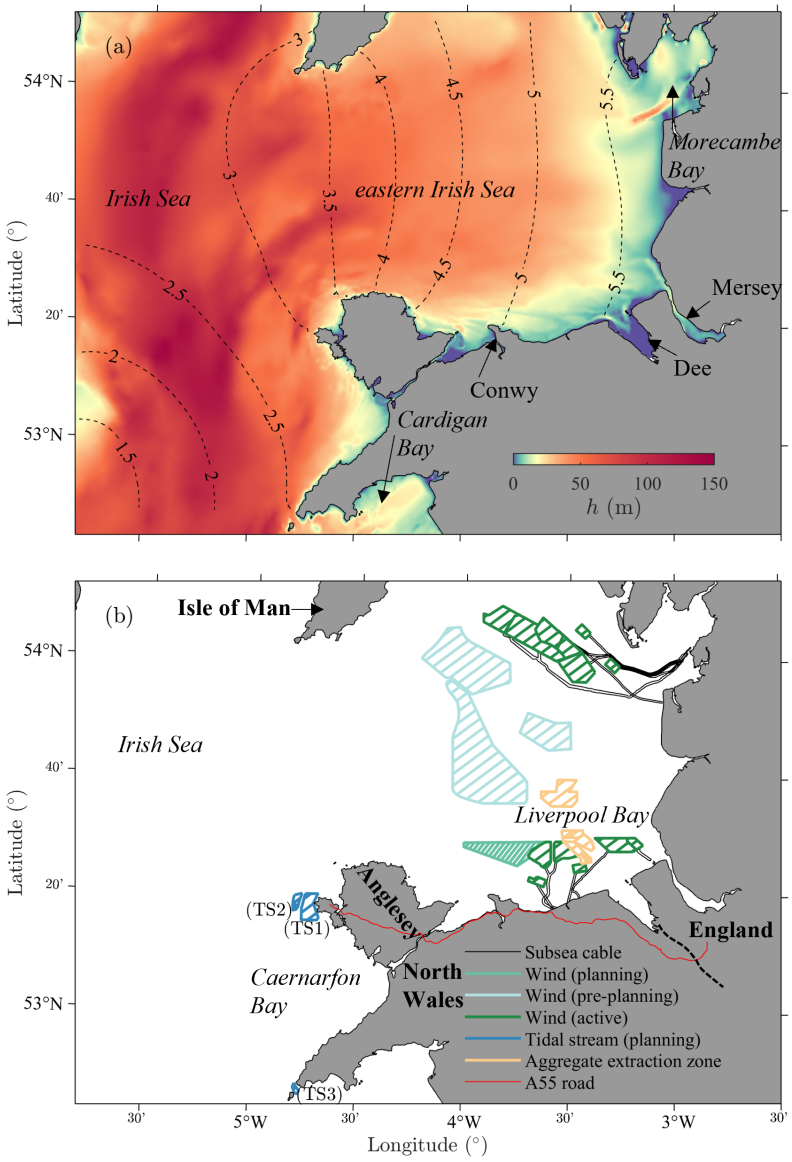

Figure 1.1: Study region. (a) Nearshore water depth (h, presented on a non-linear scale) relative to MSL, black dashed contours show the mean tidal range, calculated from $2 \times \alpha_{M2}$ (where α is amplitude). (b) Key infrastructure in the region of North Wales. Pertinent islands (bold), maritime regions (italics) and estuaries are labelled in (a) and (b). For simplicity, we define the eastern Irish Sea as the region east of the 3.5m contour in (a)

levels may rise between 28 and 101 cm by 2100 (Masson-Delmotte et al. 2021). Sea-level rise and an increase in the intensity of extreme weather events are predicted to exacerbate coastal flooding (Pope et al. 2022), directly by increasing the high water level or indirectly by reducing the capacity for artificial and natural defence (e.g. seawalls or sandbanks) to diffuse wave energy, for example (Neill & Scourse 2009). By altering the present tidal conditions, a tidal lagoon could have a significant impact on beach stability, coastal ecology and flooding. Minimising these impacts whilst maximising electricity generation is key to a successful TRS (Neill et al. 2018).

1.3 Methodology

1.3.1 TELEMAC Modelling System

In this study, we applied the open source FORTRAN code TELEMAC 8.2 (Hervouet 2007). TELEMAC operates on an unstructured fine-element grid, suitable for resolving undulating coastlines and intertidal regions. For the tidal simulation we use TELEMAC-2D – the depth-averaged hydrodynamics module (consistent with previous TRS simulations e.g. Guo et al. 2021). TELEMAC-2D solves the Saint-Venant equations of momentum and continuity (Hervouet 2007). Since the model is depth-averaged, we assume barotropic flow and there is a need to parameterise internal friction. To simulate turbulence, we use the $k - \epsilon$ turbulence model with a conjugate residual solver – Guo et al. (2020) showed the $k - \epsilon$ model to be the most accurate approach for resolving tidal flows around coastal structures (i.e. tidal lagoons). After testing the accuracy of the bed friction methods available in TELEMAC-2D, Manning's Law was the selected parameterisation method (Equation 1.5; Hervouet 2007), subsequent calibration involves tuning the spatially uniform friction coefficient n ($\mathrm{sm}^{\frac{-1}{3}}$) – a value of 0.03 was optimal (results shown in Appendix Table 2.9). Intertidal regions are handled by a wetting and drying algorithm (further described by Breugem 2022); the minimum depth is set to 0.05 m. Spatial discretisation involved applying the quasi-bubble triangle to solve the field and the linear triangle to solve surface elevations (Mewis 1993). Justification for selecting TELEMAC and a further discussion of the modelling system are given in the Supplementary Material Sec-

tion 2.6.

Application to the Irish Sea

The computational domain covers the Irish Sea and extends to the edge of the continental shelf where water depths exceed 300 m (Fig. 1.2a). An unstructured mesh of triangular elements, generated in BlueKenue (Centre 2010), was used to spatially discretise the computational domain (Fig. 1.2b). The node density is decreased from 300 m in the centre of the tidal lagoon to 30 m at the embankment (the lagoon designs are described in the next subsection), the density ranges from 1000 m to 30 m along coastlines (depending on proximity to lagoon) and reduces to 3000 m in the middle of the Irish Sea and 6000 m along each open boundary. The application of TELEMAC-2D to this region is further discussed in the Supplementary Material Section 2.7.

Model bathymetry represents a compilation of multiple datasets, each recalculated relative to MSL and linearly interpolated onto the mesh. Across the wider domain, the EMODnet 2022 bathymetric data was used (at 115 m resolution[5]). In the North Wales region, a combination of: (1) intertidal LiDAR data (at 2 m resolution[6]), (2) MBES data collected by Bangor University (available at <5 m resolution covering various coastal regions[7]), and (3) Admiralty chart data for regions in the eastern Irish Sea which are offshore[8].

When simulating a TRS, open boundaries in the numerical model must be located sufficiently far from the structure so that the forcing conditions (calculated in external models e.g. Egbert & Erofeeva 2002 – without the inclusion of a TRS) are not significantly affected by the operation of a TRS. Secondly, the physical structure and operating procedures of a TRS can induce small changes in shelf resonance (caused by the sudden increase in depth). To capture these potentially important changes, the open boundaries must cover the shelf edge regions (Zhou, Pan & Falconer 2014*a*; Mackie et al. 2021).

Two open boundaries; located in the SW Celtic Sea and NW Atlantic are present in the model domain. At each open boundary, the model is forced with 22 tidal constituents from TPXO9.v5a database (which

[5] https://emodnet.ec.europa.eu/geoviewer/

[6] https://lle.gov.wales/

[7] https://www.imardis.org/

[8] https://digimap.edina.ac.uk/

has an average RMSE of <5 cm in the open ocean – data is provided at 1/6° resolution; Egbert & Erofeeva 2002). The TPXO9.v5a database includes the five principle semi-diurnal (M_2, S_2 and N_2) and diurnal (K_1 and O_1) constituents, which explain the 90.5% of sea-level variation in our study region, as well as the higher harmonics of M_2, namely M_4 and M_6. As discussed in Section 1.2, the magnitude of freshwater driven currents are relatively small (Hadziabdic & Rickards 1999), and since the focus is on meso-scale tidal dynamics, and because the model is 2D (and will not simulate stratification), we neglect freshwater input in the model.

The model has been configured to run in parallelised mode on high performance computers (Supercomputing Wales[9]). The simulation period was 30 days from 2018/04/01 00:00:00, chosen to coincide with an ADCP deployment (the diamond marker in Fig. 1.2b marks the deployment location). Following a sensitivity analysis, we selected a constant time step Δt= 5 s. A 3-day spin-up period is implemented to allow the model to stabilise before the outputs are saved. Due to the size of the model domain, the geographic coordinate system latitude/longitude WGS84 was used; this allows TELEMAC to vary the Coriolis coefficient in accordance with latitude.

Modelling Tidal Lagoons in TELEMAC

We represent each TRS in TELEMAC-2D using T2D-TRS package – a set of user-friendly subroutines designed for simulating the operation of tidal range power plants (as described in Hanousek 2023, based on the work of Guo et al. 2021). T2D-TRS is based on the domain decomposition method, an approach consistent with other tidal range energy modelling studies (e.g. Guo 2022) – the intricacies of this method are described in detail by (Angeloudis, Falconer, Bray & Ahmadian 2016 and in the Supplementary Material Section 2.4). The TRS impoundment was implemented as a subdomain, culverts connect the impoundment domain to the ocean domain and transfer water between basins. Through modification of TELEMAC subroutines (`BUSE.f` – which was initially design to simulate culvert flow) and the development of a new subroutine (`T2D-TRS`), the activation of each culvert is controlled and the discharge is parameterised, in ac-

[9] `https://www.supercomputing.wales/`

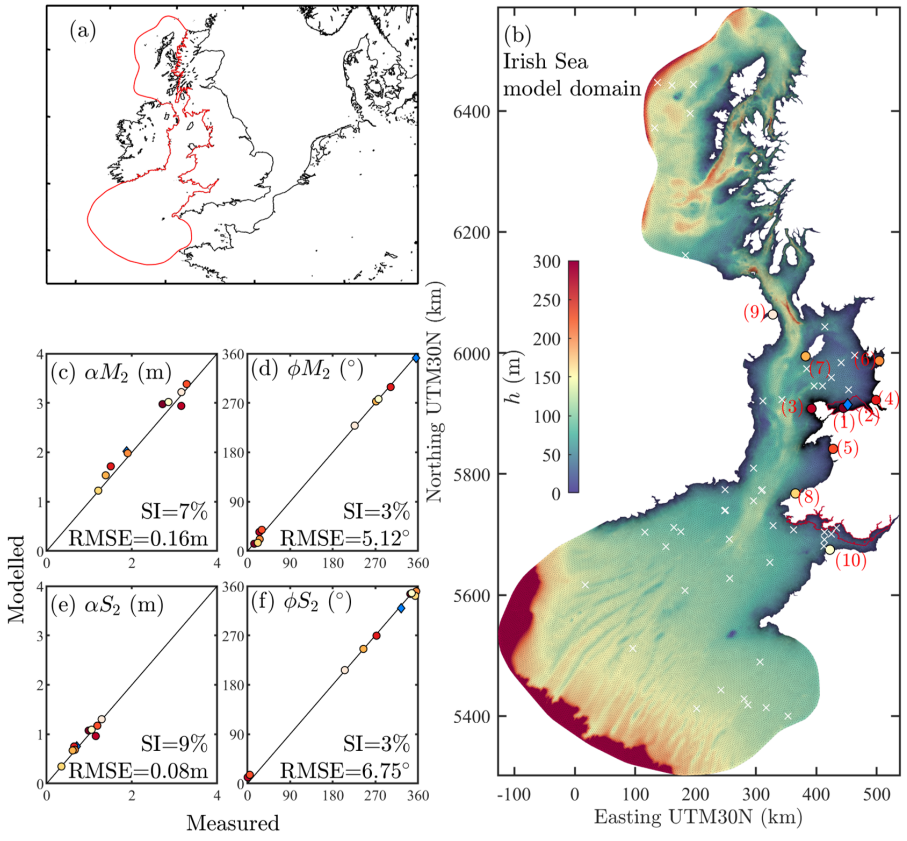

Figure 1.2: (a) The red line outlines the model domain in the context of the North West European Shelf. (b) The baseline (no tidal lagoons) Irish Sea model domain showing the water depth (h) and mesh configuration. The circular markers in (b) show the location of the tidal gauges, the diamond marker shows the location of the ADCP deployment and the white crosses show the current speed validation locations. In (b), the area contoured by the red line denotes the Welsh tidal range resource (DataMap Wales 2022). Scatter plots (c, d, e, f) show the correlation between observed and predicted tidal constituents at each validation site.

cordance with approximations of flow through turbines and sluice gates.

The typical method of turbine parameterisation is to use a turbine specific Hill chart which relates power output P (W) and discharge Q (m^3s^{-1}) to the hydraulic head H (m) (e.g. Angeloudis & Falconer 2017). We implement a turbine parameterisation which is based on a digitised Hill chart for the 9 m diameter Andritz Hydro double regulated bulb turbine (this is the most recent publicly available Hill chart; Aggidis & Feather 2012). Using Equation 1.1 (from Hanousek et al. 2023), Q and P are scaled-down[10] to a diameter $D = 7.2$ m (to retain consistency with the optimised layout for the NWTL by Xue 2021) – the scaled Hill chart is shown in the Appendix (Fig. 2.29).

$$Q_{scaled} = Q_{base} \times \frac{{D_{scaled}}^2}{{D_{base}}^2} \tag{1.1}$$

Following the recommendation by Baker (1991), sluice gates are parameterised by using the Orifice equation (Equation 1.2). Sluice gate discharge Q_{sl} is related to the discharge coefficient C_d (=1.0, consistent with the sensitivity study by Bray et al. 2016), sluice area A_{sl} (=100 m^2) and varying head difference ΔH (m) between the surface elevation of the impoundment η_i and the ocean basin η_o.

$$Q_s = C_d A_{sl} \sqrt{2g\Delta H} \tag{1.2}$$

The following constraints are applied to the layout of the TRS structures: (1) the embankment cannot be placed in water depths >30 m (since the construction costs of the embankment are prohibitive in deeper waters; Neill et al. 2018), (2) turbines and sluice gates must be sited in water depths $>$ 10 m and $>$ 5 m, respectively.

The first tidal lagoon design (Table 1.1, S1) is based on the layout originally proposed by North Wales Tidal Energy (NWTE 2013), and later optimised by Xue (2021), where A_s=150 km^2 and the number of turbines N_t=150. Subsequent scenarios implement smaller tidal lagoons with a layout based on S1 (shown in Fig. 1.4), A_s is reduced to $\approx \frac{5}{6}A_s$, $\frac{4}{6}A_s$, $\frac{3}{6}A_s$,$\frac{2}{6}A_s$ and $\frac{1}{6}A_s$. Because the rated power output varies linearly with the area of the impoundment, the same scaling approach is applied to N_t. The number of sluice gates (N_s) has minimal influence on the power output (Mackie et al. 2021), and meso-scale hydrodynamic

[10] (P is scaled using the same method applied to Q.)

Table 1.1: TRS characteristics for each scenario. L_e is embankment length, V_i is impoundment volume, P_{max} is the installed capacity, $\bar{P}$ is the average power output for each tidal lagoon and $\bar{Q}$ is the mean turbine discharge (calculated over the 30-day simulation period). Consistent with findings from Cornett et al. (2013), the relationship between A_s and $\bar{P}$ demonstrates a positive linear correlation. Due to the complex nature of coastal-seabed topography, V_i does not always exhibit a strong correlation with A_s.

Scenario	A_s (km^2)	L_e (km)	V_i (km^3)	N_t	N_S	P_{max} (MW)	$\bar{P}$ (MW)	$\bar{Q}$ m^3s^{-1}
S0 (Baseline)	-	-		-	-	-	-	
S1	154.2	33.5	1.5	150	7	2,000	415	23,170
S2	124.9	30	1.1	125	7	1,690	355	19,360
S3	98.8	24.4	0.9	100	7	1,460	302	15,940
S4	75.1	22	0.6	75	7	1,030	221	11,910
S5	50.8	17	0.4	50	7	690	151	7,980
S6	25.3	11.6	0.2	25	7	340	77	3,870

impact of bi-directional tidal lagoons, hence we use $N_s = 7$ for all scenarios.

Each tidal lagoon operates in a two-way fixed-head mode (shown in Fig. 1.3 and further described by Angeloudis & Falconer 2017), turbine operation was initiated when $\Delta H > 3.7$ m, with operation ceasing when $\Delta H < 1.4$ m (these are the optimal values for the NWTL (S1), found by Xue 2021). To accurately mimic TRS operation and to eliminate water level oscillations; a non-linear ramp function is used to gradually open and close the sluice gates/turbines. The opening operation was given by a half-sinusoidal function: $f = sin(\pi \frac{t}{2T})$, $0 < t \leq T$, and the closing operation is given by a half cosine function: $f = cos(\pi \frac{t}{2T})$, $0 < t \leq T$ (Zhou, Pan & Falconer 2014*b*), where $T = 0.5$ is the time of opening and closing (in hours). The discharge and power output from the array of turbines in each tidal lagoon is presented in Appendix Fig. 2.30.

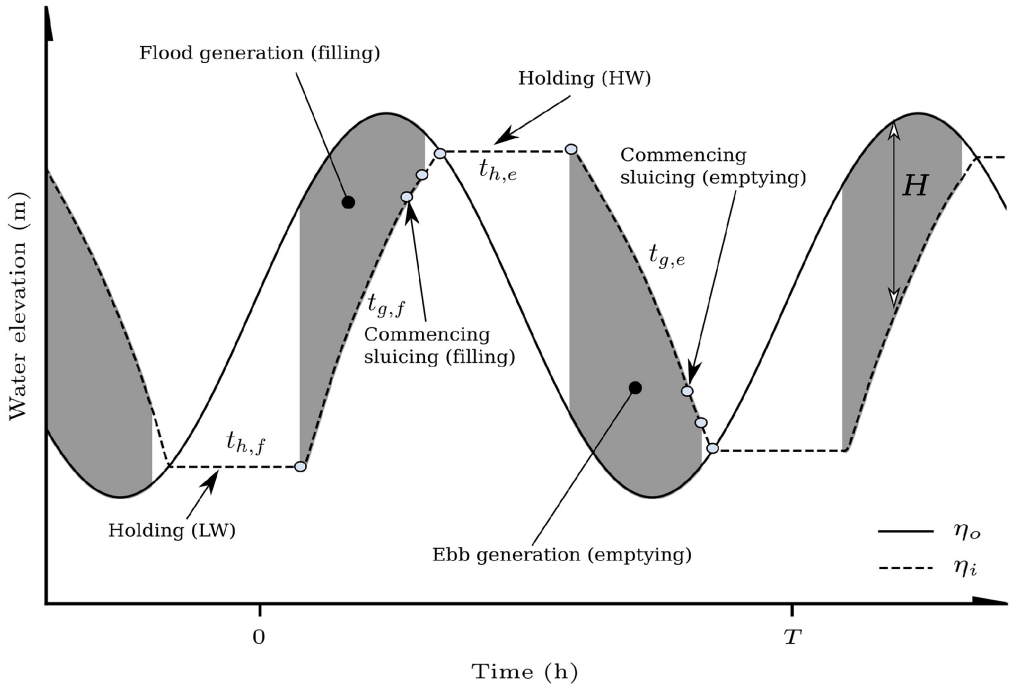

Figure 1.3: The sequence of turbine and sluice gate operation for a two-way tidal range power plant, with a fixed head and excluding pumping. Key control variables are the flood holding $t_{h,f}$, ebb holding $t_{h,e}$, flood generation $t_{g,f}$ and ebb generation $t_{g,e}$ periods (from Baker et al. 2020).

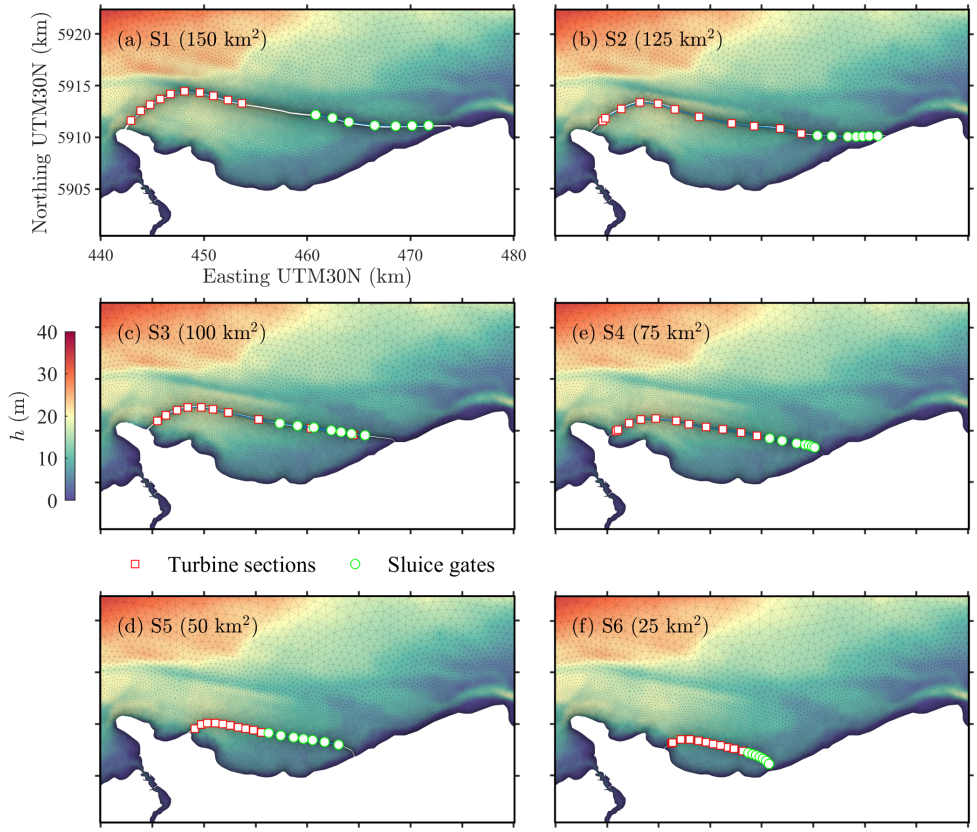

Figure 1.4: Plots (a)-(f) shows the layout of the embankment, turbines and sluice gates for each tidal lagoon scenario. The sensitivity of hydrodynamics impacts to the turbine and sluice gate layout was tested, the changes induced were of insignificant magnitude and regionally constrained to the near-field. Water depth h is relative to MSL.

1.3.2 Calibration and Validation

A timeseries of water level measured at nine tidal gauge stations (BODC 2017) and one ADCP deployment site were used to calibrate and validate the simulated free surface elevation η (at each validation station, located in Fig. 1.2b). Two error metrics, root-mean-squared error $RMSE$ (Equation 1.3) and scatter index SI (Equation 1.4), were used to quantify predictive performance. Model calibration involved tuning the Manning's coefficient to minimise the difference between the measured and observed amplitude α and phase ϕ for the M_2 and S_2 harmonics. A Manning's value of 0.03 produced optimal $RMSE$ of 5.12° and 6.75° for $\bar{\phi_{M2}}$ and $\bar{\phi_{S2}}$ and 0.16 m and 0.08 m for $\bar{\alpha_{M2}}$and $\bar{\alpha_{S2}}$ (complete calibration results are presented in Table 2.8 and 2.9). Validation results for the M_2 and S_2 harmonics at each station are presented in Fig. 1.2c, d, e and f. The five principle constituents are validated at the ADCP deployment site, results are presented in Table 1.2. Results are comparable with recent 2D hydrodynamic models for the region (e.g. Robins et al. 2015; Horrillo-Caraballo et al. 2021; Mackie et al. 2021). Detailed station-specific validation results are given in the Appendix Table 2.10.

$$RMSE = \sqrt{\frac{\sum_{i=1}^{n}(O_i - P_i)^2}{n}} \tag{1.3}$$

$$SI = \frac{RMSE}{\bar{O}} \times 100 \tag{1.4}$$

where O_i is the ith observation, P_i is the ith prediction, $\bar{O}$ is the mean observation and $\bar{P}$ is the mean prediction.

Harmonic analysis is performed on the simulated current speeds (u and v), these are validated at 47 sites where current speed measurements had been harmonically analysed (locations are marked by white crosses in Fig. 1.2). Our model tends to overestimate and underestimate the speed the tidally-driven currents for M_2 and S_2, respectively. SI scores are similar for both harmonics, 10% larger than validation results achieved by (Robins et al. 2015) in the region.

Table 1.2: Validation results for amplitude and phase of the five principle tidal constituents at the ADCP deployment site.

Amplitude α	M_2	S_2	O_1	K_1	N_2
Measured (m)	3.02	1.09	0.10	0.09	0.37
Modelled (m)	2.86	1.05	0.10	0.08	0.42
Difference (Δ)	-0.16	-0.04	0.00	-0.01	0.05
Difference ($\Delta\%$)	-5.34	-3.30	1.73	-6.71	12.55
Phase ϕ					
Measured ($^\circ$)	277.07	347.14	251.80	258.52	324.78
Modelled ($^\circ$)	276.83	346.87	248.39	264.30	319.08
Difference (Δ)	-0.25	-0.27	-3.40	5.78	-5.69
Difference ($\Delta\%$)	-0.09	-0.08	-1.35	2.24	-1.75

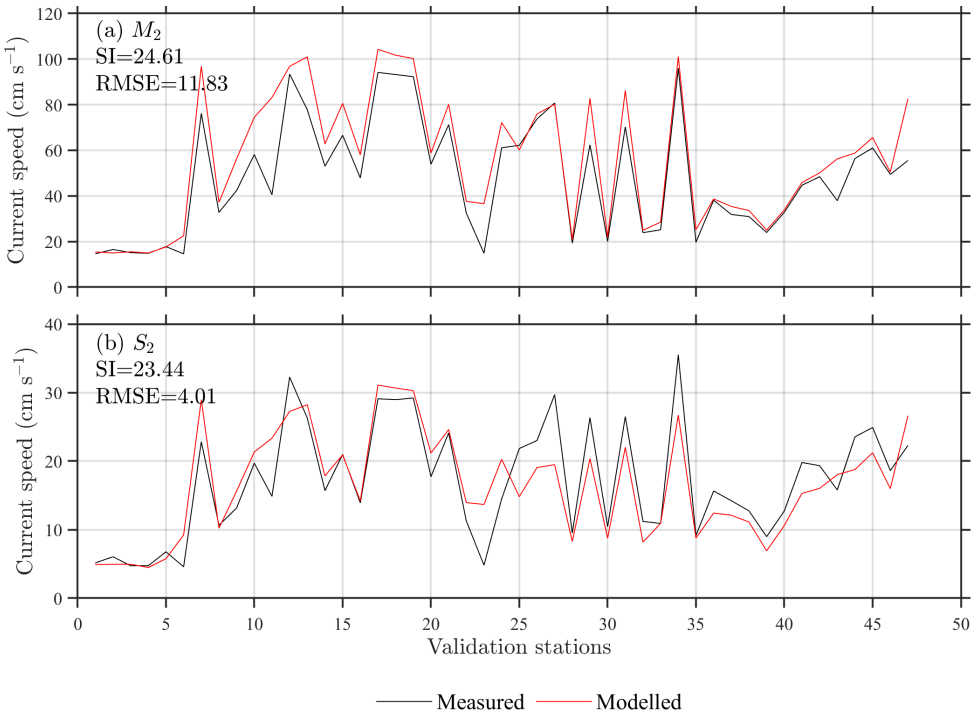

Figure 1.5: (a) M_2 and (b) S_2 current speed amplitudes. Current measurements are accessed from BODC 2017. Sites are ordered from the most northern site (1) to the southern most site (47).

1.3.3 Quantifying the Impact of Tidal Lagoon Impoundment Size

Variations in the lagoon layout in each model scenarios leads to differences in the model grid distribution between simulations. To ascertain the change Δ induced by a tidal lagoon, we linearly interpolate the model outputs: water depth h free surface elevation η and depth-averaged velocity components u, v onto regular 1 x 1 km grids at a 30 minute time step (a suitable compromise which displays changes at the appropriate resolution, whilst representing the typical grid spacing). The data grid for the ambient (baseline) scenario (S0) is then subtracted from each of the other tidal lagoon scenarios (S1-S6). We compare the magnitude of impacts between scenarios at various locations, this involves extracting a timeseries at the desired location using a nearest-neighbour interpolation. To further analyse the model outputs, we calculate additional parameters using the following methodology:

1. *Harmonic constituents*: Harmonic analysis is used to deconstruct the timeseries of η at each node into the harmonic constituents. Using the T_TIDE (Pawlowicz et al. 2002) package, harmonic analysis is performed within MATLAB R2023a.

2. *Bed shear stress*: We calculate bed shear stress τ_b ($\mathrm{kgm^{-1}s^{-2}}$) using the Manning equation:

$$\frac{\tau_b}{\rho} = gn^2 \frac{|\mathbf{u}|\mathbf{u}}{D^{\frac{1}{3}}} \tag{1.5}$$

   where ρ is seawater density ($\mathrm{kgm^{-3}}$), $\mathbf{u}$ is depth-averaged velocity vector ($= \sqrt{u^2 + v^2}$, u and v are the horizontal velocity components; $\mathrm{ms^{-1}}$), D is total water depth (m), n is Manning's coefficient ($\mathrm{sm^{-\frac{1}{3}}}$) and g is acceleration due to gravity (=9.81 $\mathrm{ms^{-2}}$).

1.4 Results and Discussion

1.4.1 Impact on Water Levels

To better understand the impacts of tidal lagoon operation on water levels, η can be deconstructed into the amplitude α and phase ϕ of the principle tidal constituents. Since M_2 is the dominant tidal constituent

(it explains 58% of the observed tidal amplitude, in the region of study), we present the predicted $\Delta\alpha_{M2}$ for each tidal lagoon scenario in Fig. 1.6. Our simulations indicate that the general pattern of α_{M2} amplification and suppression remains largely the same (for S1-S6) – a similar pattern is exhibited in $\Delta\alpha_{S2}$ (shown in Appendix Fig. 2.31). The largest tidal lagoon (S1) is predicted to increase α_{M2} by $1-3$ cm in the western Irish Sea, whilst reducing α_{M2} by $1-2$ cm in the vicinity of the tidal lagoon, along the south-east coast of Ireland, in the Bristol Channel and in Cardigan Bay – all simulated changes are within the range of uncertainty for α_{M2} and α_{S2} (Fig. 1.2). In the Bristol Channel, the $\Delta\alpha_{M2}$ caused by S2 is unexpectedly small (outlying the general trend; Fig. 1.6b), however as a consequence it induces a large reduction in $\Delta\alpha_{M2}$ in the near-field (i.e. Solway Firth shown in Fig. 1.7) these effects are driven by a change in resonant state of M_4 ($\Delta\alpha_{M4}$ is shown in Appendix Fig. 2.32). The magnitude and spatial distribution of our results are consistent with those presented by Guo (2022) (when simulating a tidal lagoon similar in design to S1) and Mackie et al. (2021) (when simulating the combined effects of four Irish Sea tidal lagoons, located at Conwy, Blackpool, Liverpool and Solway Firth).

To quantify the changes to the principle harmonic constituents, we compute the spatial average $\Delta\bar{\alpha}$ and absolute $\Delta|\bar{\alpha}|$ (Fig. 1.7 and 1.8, respectively) over three areas (defined in Fig. 1.6a). The amplitude of each of the semi-diurnal constituents (M_2, S_2 and N_2) is elevated in the far-field (defined as within a 200 km radius of the TRS), $\alpha_{M2\bar{S}2N2}$ increases from 0.1-0.3% (S6) to 0.4-0.5% (S1). In the near-field (within a 50 km radius), $\alpha_{M2\bar{S}2N2}$ reduces from -0.1-0.2% (S6) to -0.35-0.4% (S1; Fig. 1.7b). In accordance with the findings of Cornett et al. (2013), Table 1.3 quantifies a strong linear correlation between $\Delta\bar{\alpha}_{M2S2}$ and the tidal lagoon characteristics in the far-field (S3 outlies this trend), and to a lesser extent in the near-field (S3 and S1 outlie this trend) – S3 and S1 are the optimal scenarios to minimise near-field semi-diurnal constituent disturbances, and thus $\Delta\eta_{max}$. Impoundment volume V_i has the strongest correlation with far-field $\Delta|\bar{\alpha}_{M2S2N2}|$ and $\Delta|\bar{\eta}_{max}|$, whereas near-field changes have a stronger correlation with $\bar{P}$ and $\bar{Q}$ (Table 1.3).

In scenario S2, the tidal lagoon has the unique effect of minimising the disturbance to the amplitude of the diurnal constituents (K_1 and O_1), across all regions (Fig. 1.7, further supported by Fig. 1.8). The far-field

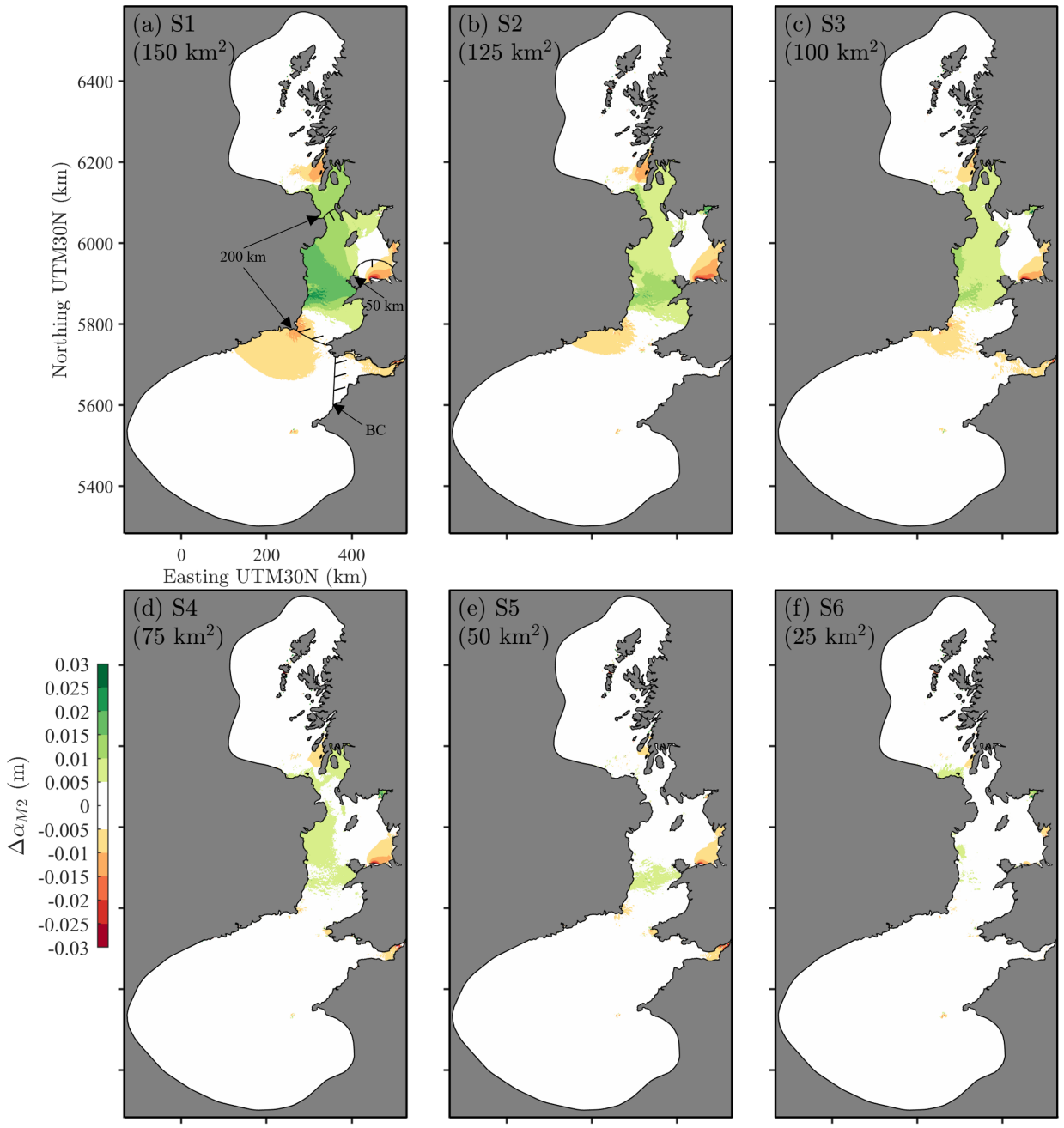

Figure 1.6: The predicted change in the amplitude of the M_2 constituent $\Delta\alpha_{M2}$ (m), under each scenario (a) S1, (b) S2, (c) S3, (d) S4, (e) S5 and (f) S6. The results are interpolated to a 1×1 km grid for visualisation.

Table 1.3: Correlation coefficient R scores between the $\Delta|\bar{\alpha}|$ of principle harmonic constituents (and $|\bar{\eta_{max}}|$) and tidal lagoon characteristics: mean power output $\bar{P}$, mean turbine discharge $\bar{Q}$, impoundment surface area A_s and impoundment volume V_i (calculated over the 30-day simulation period at MSL).

	Far-field (200 km)				Near-field (50 km)			
	$\bar{P}$	$\bar{Q}$	A_s	V_i	$\bar{P}$	$\bar{Q}$	A_s	V_i
$\Delta\|\bar{\alpha_{M2}}\|$	0.97	0.97	0.98	**0.99**	0.70	**0.70**	0.70	0.67
$\Delta\|\bar{\alpha_{S2}}\|$	0.96	0.97	0.98	**0.98**	0.83	**0.90**	0.84	0.86
$\Delta\|\bar{\alpha_{N2}}\|$	0.89	0.90	0.89	**0.91**	0.85	0.86	0.86	0.84
$\Delta\|\bar{\alpha_{K1}}\|$	0.41	**0.41**	0.40	0.38	**0.49**	0.48	0.46	0.41
$\Delta\|\bar{\alpha_{O1}}\|$	**0.34**	0.33	0.31	0.29	**0.64**	0.63	0.61	0.57
$\Delta\|\bar{\eta_{max}}\|$	0.94	0.95	0.96	**0.97**	**0.95**	0.95	0.94	0.92

reduction in the amplitude of diurnal constituents slightly diminishes the impact of the semi-diurnal amplitudes, having a reductive effect on η_{max}. These interactions are also evident in the near-field, however the reduction is of a smaller magnitude, and the $\Delta|\bar{\alpha}|$ of semi-diurnal constituents reaches a maximum for all scenarios. For the diurnal constituents (O_1 and K_1), far-field $\Delta|\bar{\alpha}|$ is poorly correlated with the tidal lagoon characteristics presented in Table 1.3, however the correlation does slightly increase in the near-field. In Fig. 1.9 the spatial pattern of $\Delta\eta_{max}$ is presented, these changes are a product of the combined interaction of the modified harmonic constituents. As the dominant constituent, the $\Delta\alpha_{M2}$ strongly modulates the $\Delta\eta_{max}$ (presented in Fig. 1.6). However, the $\Delta\eta_{max}$ in the Cardigan Bay region is significantly less than $\Delta\alpha_{M2}$ for the same region, the $\Delta\alpha_{O1K1}$ (diurnal constituents) are suppressing $\Delta\eta_{max}$ in this region (Appendix Fig. 2.36 and 2.35).

Simulations by Guo (2022) for the largest tidal lagoon (S1) somewhat agree with our results, although, a direct comparison is difficult since Guo (2022) exclusively presents near-field results. Guo (2022) predicted a reduction in η_{max} between $5 < \eta_{max} < 10$ cm in Liverpool Bay, whereas our model predicts $2 < \eta_{max}$

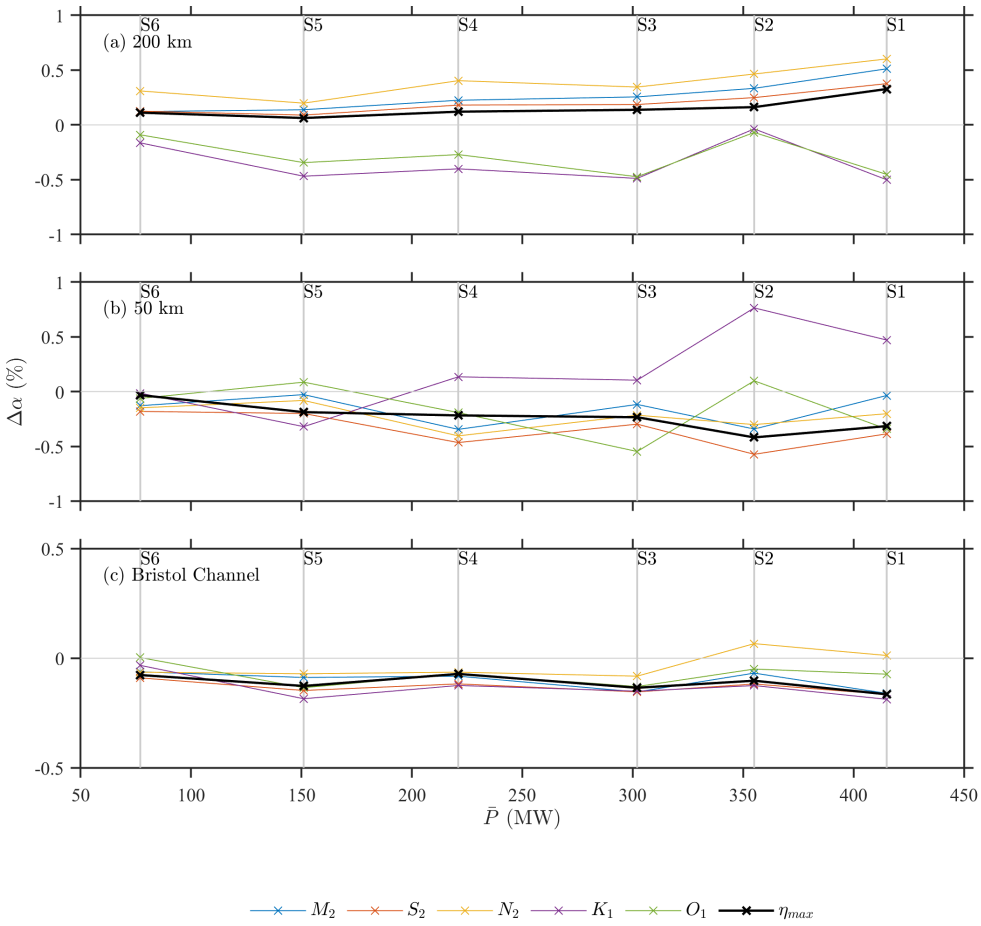

Figure 1.7: The percentage change in amplitude $\Delta\bar{\alpha}$ of tidal constituents (and $\bar{\eta_{max}}$) averaged over various areas: (a) $\approx$ 200 km, and (b) $\approx$ 50 km in radius from each lagoon, and (c) the Bristol Channel (BC) region (shown in Fig. 1.6a). In each calculation, changes inside the lagoon impoundment are omitted. To reduce the effects of local extremes, which especially occur over inter-tidal regions, the 1 x 1 km grids were used for these calculations. Mean power output $\bar{P}$ is calculated over the 30-day simulation period.

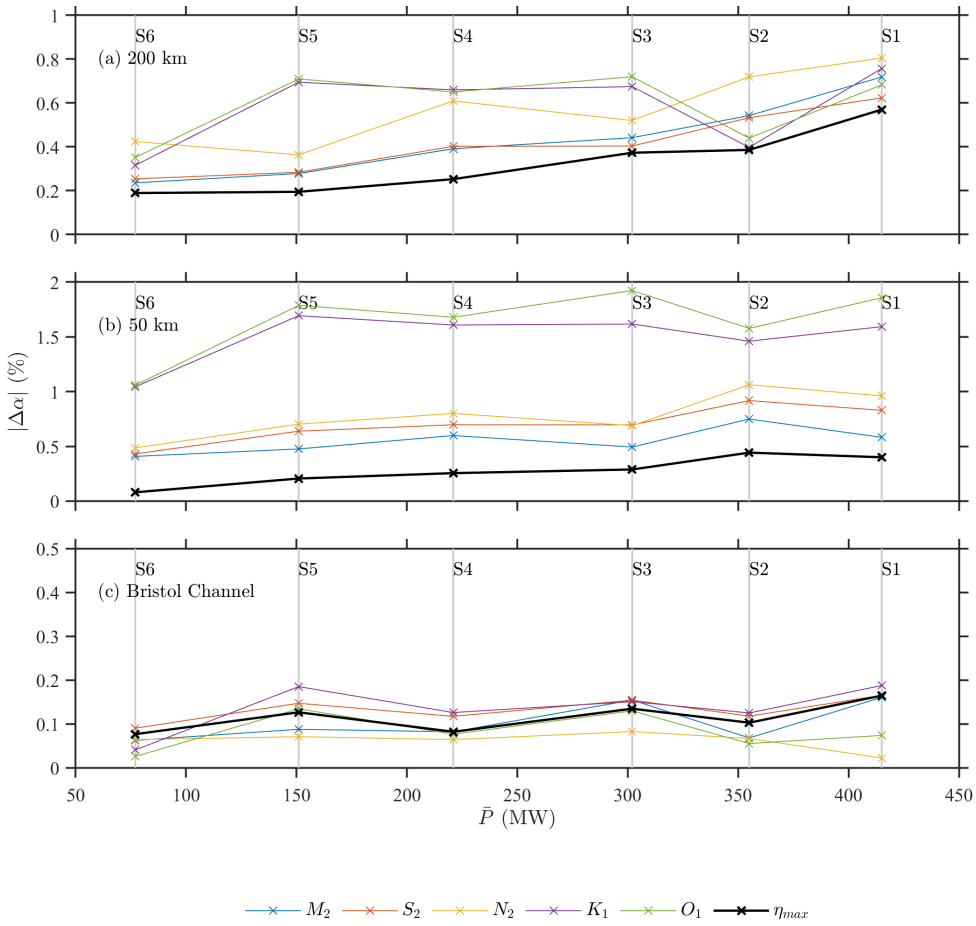

Figure 1.8: The absolute percentage change in amplitude $\Delta|\bar{\alpha}|$ of tidal constituents (and $|\bar{\eta_{max}}|$) averaged over various areas: (a) $\approx$ 200 km, and (b) $\approx$ 50 km in radius from each lagoon, and (c) the Bristol Channel (BC) region (shown in Fig. 1.6a). In each calculation, changes inside the lagoon impoundment are omitted. To reduce the effects of local extremes, which especially occur over inter-tidal regions, the 1 x 1 km grids were used for these calculations. Mean power output $\bar{P}$ is calculated over the 30-day simulation period.

< 3 cm, therefore there is a considerable difference in the magnitude of the prediction. Furthermore, Guo (2022) predicted a decrease in η_{max} across the Cardigan Bay region (between $5 < \eta_{max} < 10$ cm); such a decrease is not evident in our results. The difference in magnitude could be attributed to the different operational schemes, Guo (2022) operates the TRS using a flexible head setup, this ensures continuous operation throughout the neap tides. Thus, the TRS is operating for a larger proportion of the simulation period, potentially causing more severe hydro-environmental impacts. On the other hand, our fixed head setup results in a 'no generation' period at the peak of both neap tides (Appendix Fig. 2.30).

The relationships quantified in Table 1.3 imply that reducing the far-field $\Delta|\bar{\eta_{max}}|$ (whilst maintaining $\bar{P}$) could be achieved by minimising V_i. Because $P \propto A_s H^2$ (where P is the instantaneous potential power), V_i can be reduced at no cost to electricity generation, as long as it does not affect H. Withholding a larger volume of water reduces the basin volume into which the incoming tidal wave can propagate. An ideal impoundment maximises A_s, whilst ensuring the water depth across the majority of the impounded region does not drastically exceed practical limits[11]. It is the impoundment of these deeper regions which do not benefit the TRS power output, nor reduce hydrodynamic impact. Our results indicate that reducing near-field changes (whilst maximising $\bar{P}$) presents a more significant challenge because $\Delta|\bar{\eta_{max}}|$ is strongly correlated with mean turbine discharge $\bar{Q}$ in this region, although some reduction in near-field change may occur through the minimisation of V_i. This relationship can be attributed to the locally-constrained nature of Q (which will increase water levels).

Table 1.4 presents $\Delta\eta_{max}$ at geographically proximal tidal lagoon sites (L1-L6), major docks (D1-D4) and communities vulnerable to coastal flooding (F1-F6), each of which are located in Fig. 1.9a. At every location where η_{max} is predicted to increase (Porthmadog, Solway Firth, Dublin, Belfast and Dundalk) $\Delta\eta_{max} <$ 3 cm. At first, these changes may seem insignificant, however, when coupled with a: surge component, extreme waves and a rising MSL, amplifying the astronomical tide will exacerbate coastal flood risk (Lewis et al. 2011). This is especially relevant for locations where the relative change is larger (e.g. Dundalk and

[11] i.e. The depths required to site low-head hydro electric turbines and sluices gates, often cited as 10 m and 5 m, respectively

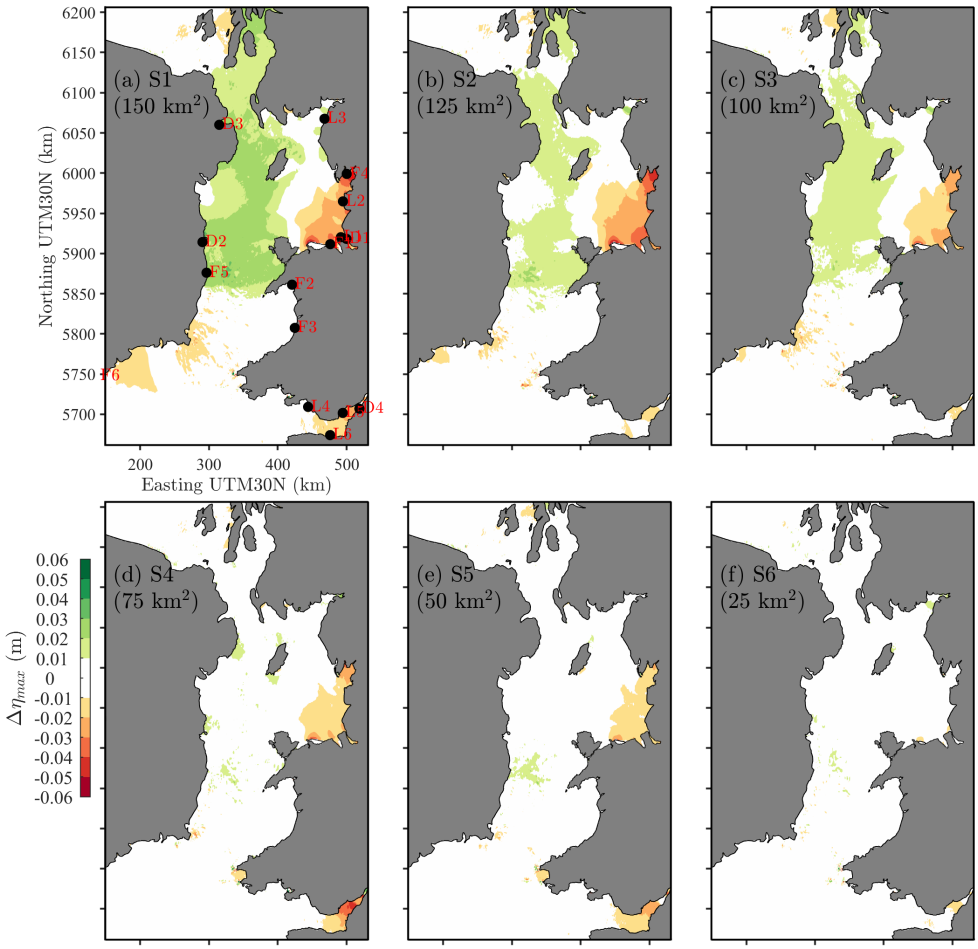

Figure 1.9: Maximum changes in free surface elevation η_{max} (m) for each tidal lagoon scenario (a) S1, (b) S2, (c) S3, (d) S4, (e) S5 and (f) S6. In (a), the location of key sites (referred to in Table 1.4) are shown. Results are interpolated to a 1×1 km grid for visualisation.

Belfast where $\Delta\eta_{max} = 2.03\%$ and 1.02%, respectively; Table 1.4). Our hypothesis, hydrodynamic impact is positively correlated with tidal lagoon impounded size, is supported by the mean absolute change (Table 1.9, RMS) across all sites.

Under scenarios S1 and S2, the largest changes in η_{max} are experienced at most sites (with the exception of Swansea and Watchey, in the Bristol Channel). Scenario S1 has the greatest impact on sites further afield (e.g. D2, D3 and L5), whereas S2 induces the greatest change at near-field sites (e.g. F1). In each scenario, the simulated $\Delta\eta_{max}$ does not exceed 4 cm (the maximum increase, relative to baseline conditions, was 2.03% at Dundalk). Interestingly, the strongest changes at the Bristol Channel locations L4 and L6 are experienced under scenario S5. Our scenarios (S1-S6) negatively interact with η_{max} at five potential tidal lagoon sites (L1, L2, L4, L5 and L6), reducing the available tidal range resource. Since scenario S2 induces the strongest near-field changes, it will cause the largest reduction in the available tidal range resource at eastern Irish Sea tidal lagoon sites. Whereas at site L3 (Solway Firth), NWTL scenarios S1-S6 positively interact with η_{max} (this is supported by the pattern observed in Fig. 1.6).

1.4.2 Impact on Tidal Currents

In the far-field regions, each scenario has similar implications for $\Delta|U_{max}|$. Alternating patches of increased and reduced $\Delta|U_{max}|$ are present along the north of the Isle of Man, St Georges Channel, Bristol Channel and in the North Channel – these values are within the models range of error (Fig. 1.5). These regions could be associated with modifications to tidal phase and the slight shift in location of tidal currents. Near-field changes increase in magnitude with A_s (further evident in Fig. 1.11), whereas the nature of this relationship for far-field changes is less clear. Cornett et al. (2013) explored the link between hydro-environmental impact (namely, tidal range and current speed changes) and $\bar{P}$ for tidal lagoons in the Minas Basin. Simulated changes exhibited a strong linear correlation with the scale of development. These findings are mostly consistent with our results (in respect to water level changes, discussed in Section 1.4.1), however the results presented in Fig. 1.10 and Table 1.5 do not support this idea that changes in current speed exhibit a similar correlation. This could be attributed to the less constrained geometry,

Table 1.4: The change in maximum free surface elevation $\Delta\eta_{max}$ (m) simulated at various key locations in the Irish Sea (shown in Fig. 1.4a). The maximum values at each site are highlighted in bold. Percentage change $\Delta\%$ (given in italics) is calculated relative to the baseline η_{max}.

		Proposed tidal lagoon sites						**Major docks**				**Locations at risk of coastal flooding**					
	Site	Mersey	Blackpool	Solway	Swansea	Cardiff	Watchey	Liverpool	Dublin	Belfast	Bristol	Prestatyn	Porthmadog	Aberystwyth	Morcambe	Dundalk	Cork
	Site ID	L1	L2	L3	L4	L5	L6	D1	D2	D3	D4	F1	F2	F3	F4	F5	F6
	Lat (°)	53.43	53.83	54.75	51.53	51.47	51.47	53.41	53.34	54.65	51.51	53.35	52.9	52.41	54.14	53.00	51.76
	Lon (°)	-3.13	-3.08	-3.45	-3.81	-3.08	-3.34	-3.00	-6.15	-5.87	-2.73	-3.36	-4.18	-4.12	-3.00	-6.03	-8.25
Scenario		Maximum free surface elevation η_{max}															RMS
S0	(m)	4.64	4.79	4.28	4.91	6.78	5.99	4.49	2.01	1.69	7.24	4.53	2.84	2.87	5.63	1.36	1.98	-
S1	Δ (m)	-0.02	-0.03	0	-0.01	**-0.02**	-0.02	-0.02	**0.01**	**0.02**	-0.01	-0.01	0	-0.01	-0.04	**0.03**	**-0.01**	0.016
S1	Δ (%)	*-0.39*	*-0.53*	*0.1*	*-0.16*	*-0.34*	*-0.26*	*-0.47*	*0.62*	*1.02*	*-0.14*	*-0.3*	*0.05*	*-0.19*	*-0.69*	*2.03*	*-0.44*	*0.483*
S2	Δ (m)	**-0.03**	**-0.03**	**0.01**	0	-0.01	-0.01	**-0.02**	0	0.01	0	**-0.03**	0	0	**-0.04**	0.01	-0.01	0.013
S2	Δ (%)	*-0.68*	*-0.63*	*0.15*	*-0.06*	*-0.21*	*-0.17*	*-0.52*	*0.1*	*0.76*	*-0.04*	*-0.56*	*0.16*	*-0.07*	*-0.73*	*0.86*	*-0.31*	*0.376*
S3	Δ (m)	-0.02	-0.02	0.01	0	-0.01	-0.01	-0.02	0.01	0.01	-0.01	-0.02	0	**-0.01**	-0.03	0.01	-0.01	0.0125
S3	Δ *(%)*	*-0.46*	*-0.4*	*0.15*	*-0.09*	*-0.15*	*-0.11*	*-0.34*	*0.38*	*0.58*	*-0.12*	*-0.33*	*-0.17*	*-0.31*	*-0.48*	*0.78*	*-0.32*	*0.323*
S4	Δ (m)	-0.01	-0.02	0.01	0	-0.03	-0.01	-0.01	0.01	0	**-0.02**	-0.02	**0.01**	0	-0.03	0	0	0.011
S4	Δ (%)	*-0.32*	*-0.36*	*0.14*	*-0.1*	*-0.48*	*-0.18*	*-0.24*	*0.25*	*-0.12*	*-0.33*	*-0.36*	*0.22*	*0*	*-0.51*	*0.19*	*0.22*	*0.251*
S5	Δ (m)	-0.02	-0.02	0	**-0.01**	-0.02	**-0.02**	-0.01	0	0	-0.01	-0.02	0	-0.01	-0.02	0.01	0	0.011
S5	Δ (%)	*-0.33*	*-0.32*	*0.03*	*-0.18*	*-0.33*	*-0.27*	*-0.23*	*0.13*	*0.19*	*-0.11*	*-0.43*	*-0.08*	*-0.2*	*-0.31*	*0.44*	*-0.18*	*0.235*
S6	Δ (m)	-0.01	-0.01	0.01	0	-0.01	-0.01	0	0.01	0	-0.01	-0.01	0	0	-0.01	0	0	0.006
S6	Δ (%)	*-0.21*	*-0.12*	*0.21*	*-0.09*	*-0.15*	*-0.15*	*-0.04*	*0.48*	*0.19*	*-0.07*	*-0.19*	*0.08*	*-0.11*	*-0.1*	*0.28*	*0.05*	*0.158*

and lower tidal range, of the Irish Sea (compared to the Minas Basin) which result in a lower blockage effect (as described by Mackie et al. 2021) for Irish Sea tidal lagoons.

Tidal Stream Resource

It is important to consider the impact of TRS on the resource availability of other sources of marine renewable energy. Tidal stream energy is rapidly developing and a number of sites are located in the Irish Sea (Kadiri et al. 2012), for example the recently announced 35 km^2 West Anglesey site is relatively close to the tidal lagoon site (shown in Fig. 1.1, TS1). Power generation is extremely sensitive to hydrodynamic conditions, thus seemingly trivial interactions could significantly reduce power output across an array of tidal stream turbine. For instance, a small change in current speed would have a significant impact on the power output P (of a tidal stream turbine) is a function of U^3.

In Table 1.5, we examine the change in mean and maximum current speed ($|\bar{U}|$ and $|U_{max}|$, respectively) over three sites under scenarios S1-S6. The simulated $\Delta|\bar{U}|$ and $\Delta|U_{max}|$ are generally small ($< 1\%$) at the three sites, the largest $\Delta|U_{max}|$ is a decrease of 2 cm s^{-1} (0.311%) which occurs in S1. These results agree with those presented in Fig. 1.10, supporting the argument that the regions of significant current speed change are locally constrained. The results show a weak correlation between RMS Δ in $|\bar{U}|$ or $|U_{max}|$ and A_s. Analysis of the metrics presented in Table 1.5 suggests that the tidal lagoon design in S2 is the optimal scenario for co-location with tidal stream (maximising $\bar{P}$, whilst minimising reduction in mean and maximum current speed over the three tidal stream sites considered).

Bed Shear Stress

Bed shear stress magnitude can be used as a proxy for erosion and deposition, high bed shear stresses results from a combination of shallow bathymetry and high current speeds (through the relationship described in Equation 1.5). In each tidal lagoon scenario (Fig. 1.11), $\Delta max|\tau_b|$ decreases at the western end of the structure, this region extends further west along the north coast of Anglesey in the larger tidal lagoon scenarios. Each tidal lagoon impedes on the progression of the tidal wave around the Great Orme

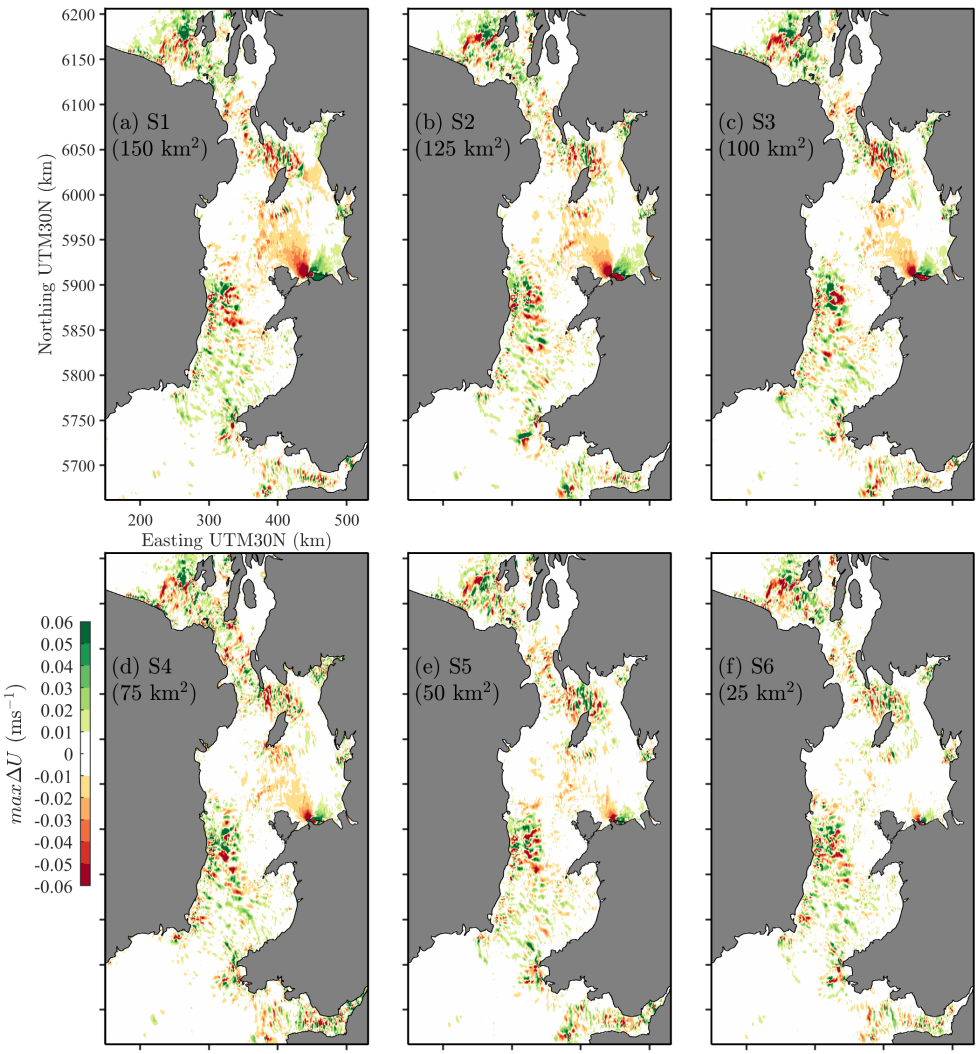

Figure 1.10: The change in maximum current speed $\Delta|U_{max}|$ in each tidal lagoon scenario (a) S1, (b) S2, (c) S3, (d) S4, (e) S5 and (f) S6. Results are interpolated to a 1 x 1 km grid for visualisation.

Table 1.5: Change in magnitude of the mean and maximum tidal current speed ($\Delta|\bar{U}|$ and $\Delta|U_{max}|$, respectively) over the 30-day simulation period, changes are quantified at three tidal stream sites in the Irish Sea leased by the Crown Estate, the location of each site is shown in Fig. 1.1. The maximum values at each site is highlighted in bold. Percentage change ($\Delta\%$) is calculated relative to the baseline $|\bar{U}|$ and $|U_{max}|$, respectively.

		Tidal stream site							
	Site name	West Anglesey		Holyhead Deep		Bardsey Sound			
	Status	Consented		Consented		Pre-planning			
	Site ID	TS1		TS2		TS3			
	Lat (°)	53.30		53.31		52.77			
	Lon (°)	-4.73		-4.79		-4.78			
	Area (km)	35.04		9.17		3.34			
Scenario		$\bar{U}$	U_{max}	$\bar{U}$	U_{max}	$\bar{U}$	U_{max}	RMS $\bar{U}$	RMS U_{max}
S0	(ms^{-1})	1.23	2.54	0.99	2.15	1.34	2.64	-	-
S1	Δ (ms^{-1})	-0.00	0.00	0.00	-0.01	-0.01	-0.02	0.004	0.012
S1	Δ (%)	***-0.18***	*-0.09*	***-0.38***	***-0.64***	*-0.37*	***-0.78***	*0.311*	*0.503*
S2	Δ (ms^{-1})	0.00	0.00	0.00	-0.01	0.00	-0.01	0.002	0.006
S2	Δ (%)	*-0.13*	*-0.12*	*0.07*	*-0.39*	*-0.34*	*-0.26*	*0.178*	*0.255*
S3	Δ (ms^{-1})	0.00	0.00	0.00	-0.01	-0.01	-0.02	0.003	0.01
S3	Δ (%)	*0.01*	*0.10*	*-0.14*	*-0.38*	***-0.46***	*-0.73*	*0.203*	*0.404*
S4	Δ (ms^{-1})	0.00	0.01	0.00	0.00	-0.01	0.00	0.003	0.003
S4	Δ (%)	*0.07*	***0.29***	*0.23*	*0.10*	*-0.41*	*0.07*	*0.234*	*0.152*
S5	Δ (ms^{-1})	0.00	0.01	0.00	0.00	0.00	-0.01	0.002	0.004
S5	Δ (%)	*0.04*	*0.21*	*0.10*	*-0.02*	*-0.30*	*-0.26*	*0.145*	*0.163*
S6	Δ (ms^{-1})	0.00	0.01	0.00	0.00	0.00	-0.01	0.002	0.004
S6	Δ (%)	*-0.01*	*0.10*	*0.12*	*-0.16*	*0.16*	*0.44*	*0.095*	*0.234*

headland and into the areas which are impounded by the tidal lagoon (such as Llandudno Bay and Rhos Bay), reducing tidal current speeds and therefore bed shear stress (a function of current speed squared). Our simulations suggest that the sandbanks in Conwy Bay will experience reduced $max|\tau_b|$. These impacts scale closely with A_s, for example in S6 the region where $\Delta max|\tau_b| > 0.02$, does not extend west beyond the Great Orme. A similar, albeit smaller, region of reduced bed shear stress appears at the eastern end of the structure and in the Mersey estuary.

In agreement with previous TRS simulations (e.g. Mackie et al. 2021), the seabed in the vicinity of the turbines experiences a dramatic increase in $max|\tau_b|$. Due to the offshore location of the embankment, in scenarios S1-S5 the turbine exit jets flow over Constable Bank (an important offshore sandbank from an ecological and coastal defence perspective), this is likely to result in localised scour over the bank and extensive morphological change. Guo (2022) used a conventional quadratic stress law to calculate τ_b in the near-field region of the NWTL. Regions of high τ_b local to the turbines are consistent with Guo (2022) results, and the region of reduced $max|\tau_b|$ at the western end of the structure is supported by Mackie et al. (2021) (from simulations of the Conwy lagoon, where $A_s = 50$ km^2).

1.4.3 Limitations

The TELEMAC-2D model used here is a two-dimensional (depth-averaged) model, forced only by tides. The model does not consider density-flows, wind/wave induced currents, freshwater inflows and atmospheric pressure. Based on previous research (e.g. Fairley et al. 2014), we suspect that the interaction between a TRS and these physical mechanisms (i.e waves) would have insignificant effect on large scale hydrodynamics, therefore we choose to focus solely on tidal dynamics. Due to the computational demands and complexity of the 3D modelling technique, it is only necessary for studies which focus on the near-field impacts of TRSs (Čož et al. 2019) – to the authors knowledge, previous shelf-scale simulations of TRSs have exclusively used 2D models. Current understanding of the 3D flow pattern caused by the turbine exit jets, suggests that it is only significant within 20D of the turbines (in our case, this is a distance of 144 m; Jeffcoate et al. 2017). Because our study focuses on impacts well in excess of this distance, we believe that

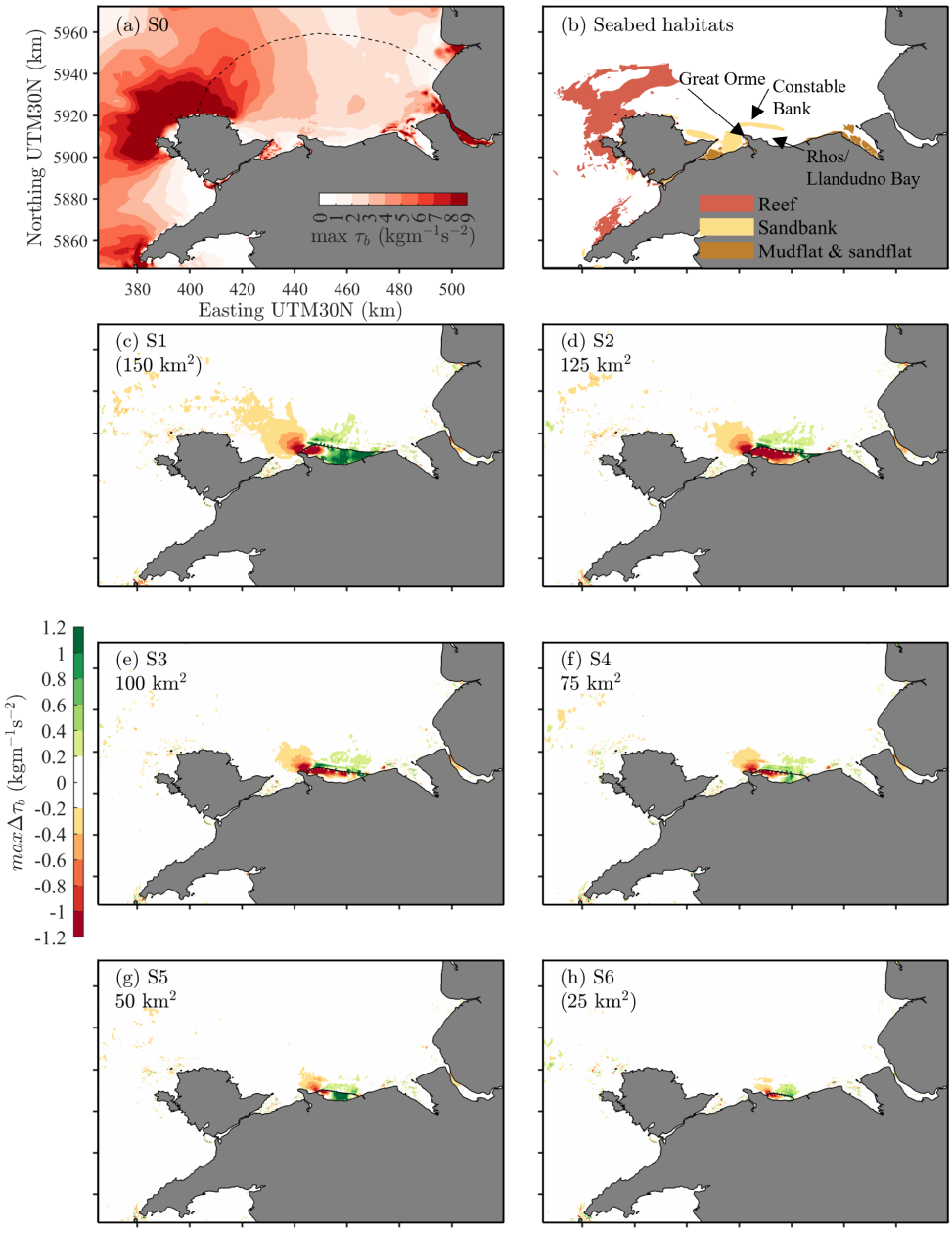

Figure 1.11: The change in magnitude of maximum bed shear stress $\Delta max|\tau_b|$ for each tidal lagoon scenario (c) S1, (d) S2, (e) S3, (f) S4, (g), S5 and (h) S6. (a) Shows the bed shear stress in the baseline scenario (the dashed lined denotes the region within a 50 km radius of each tidal lagoon, referred to in Fig. 1.7). (b) Shows key benthic habitats located within Welsh waters (delineated by Natural Resources Wales; DataMap Wales 2022), these features are sensitive to $\Delta max|\tau_b|$. Key locations are labelled in (b). Results are interpolated to a 250 x 250 m grid for visualisation.

our ignorance to these 3D flows will have a negligible impact on our overall findings. Seabed roughness, which is the combined effect of seabed substrate type and bedform morphology, influences flow strength, turbulent mixing, bed shear stress and sediment transport. In our model, seabed roughness is parameterised using a spatially constant Manning's coefficient, whereas in reality the bed roughness and varies in space and time due to seabed substrate type and bedform morphology. Future research may involve coupling this model with a morphodynamic/sediment transport module which includes a seabed sediment distribution (based on observations) and a parameterisation of spatio-temporal bedform roughness (as described in Davies & Robins 2017).

In this study, each TRS use a fixed head setup, the number of turbines were scaled linearly with impoundment area and the number of sluice gates remained constant. When designing future TRSs, developers would maximise electricity output through use of 0D models to optimise the number and position of turbines and sluice gates. In addition, the TRS would use a flexible operational head, which has been shown to increases power output by up to 10% (Xue et al. 2019; Xue et al. 2020). Introducing a flexible head operational mode in these simulations may increase the time-averaged impact of each lagoon, since it would remove the period of 'no generation' during neap tides (Appendix Fig. 2.30). Optimising these aspects of the TRS was not within the scope of this study.

Pappas et al. (2023) recently showed the importance of selecting a representative simulation period when conducting resource, and environmental impact, assessments for proposed TRS. In our study, we were constrained to within the measurement period of the ADCP deployment. Future studies could use only tidal gauges for validation and implement the method described by Pappas et al. (2023), selecting a tidal month which is representative of the long-term average tidal conditions.

1.5 Conclusions

In this study, we investigate the impact of tidal lagoon impoundment size on water levels and tidal currents. Through the use of harmonic analysis, we describe complex and distinct responses in the amplitude of the principle tidal constituents, to the operation of a tidal lagoon. A fully validated (tidal elevations

and currents) shelf-scale hydrodynamic model, based on the TELEMAC modelling system, is developed. The T2D-TRS package is implemented to simulate six hypothetical tidal lagoon scenarios. Located on the North Wales coast, each tidal lagoon has an impoundment area ranging from 25 - 150 km^2. From the discussion and analysis of our results, the following conclusions are drawn:

- The amplitude of semi-diurnal constituents M_2, S_2 and N_2 are reduced in the near-field (within a 50 km radius of the lagoon) and increased in the far-field (within a 200 km radius of the lagoon).
- In the most extreme scenario (a 150 km^2 lagoon impoundment area) maximum water levels are increased by 2-3 cm in the western Irish Sea, and reduced by 2-4 cm in the eastern Irish Sea, having implications for coastal flood risk, intertidal area extent and the potential tidal range energy resource at other sites.
- A tidal lagoon with a 125 km^2 impoundment area causes a unique amplitude response in M_4, resulting in unusually large near-field changes (which exceed the magnitude of change induced by a 150 km^2 lagoon), whilst far-field changes are significantly reduced in severity (especially in the Bristol Channel).
- Modifications to the amplitudes of the diurnal-constituents O_1 and K_1 are around twice as large in the near-field, these changes weakly correlate with tidal lagoon characteristics, and have only a minor influence on water levels.
- Tidal lagoon impoundment volume exhibits the strongest correlation ($R = 0.97$) with the net far-field change in water levels, whereas the mean turbine discharge shows the strongest correlation ($R = 0.95$) in the near-field.
- Maximum depth-averaged tidal current speeds (and bed shear stresses) will reduce to the northwest of the structure (> 6 cm s^{-1}), whilst current speeds in the vicinity of the turbines will increase – although only trivial changes in the local tidal stream resource are noted, increases in bed shear stress will undoubtedly modify key benthic habitats (causing the erosion of Constable Bank and deposition in the region of Conwy Sands).

Due to the enormous civil engineering challenge and substantial capital cost associated with developing a TRS, the use, and further development, of numerical models offers an excellent opportunity to predict hydro-environmental impacts prior to investment. We believe that there remains a significant potential to optimise tidal lagoon design parameters. Future research could explore the relationships discussed in this study at other tidal range energy sites. In particular, the effect of reducing impoundment volume, whilst keeping impoundment area constant. We suspect that this may reduce hydro-environmental impacts, at no cost to power generation. Tidal range power plants are expected to operate for over a century, therefore the evolution of a TRSs interaction with a rising sea level needs to be assessed – a research gap previously outlined by Barclay et al. (2023).

Chapter 2

Supplementary Material

2.1 Research Background and Rationale

It is scientifically evident and widely acknowledged that humans are modifying the Earth's climate. Since pre-industrial times (1850-1900), global average temperature has risen over 1°C (NOAA 2021)[1]. Anthropogenic climate change is exacerbating the biodiversity crisis, increasing the rate of sea-level rise and ocean acidification, whilst also increasing the frequency and magnitude of unprecedented weather extremes, such as tropical cyclones, storm surges, heatwaves, droughts and episodes of land erosion (Perkins 2015; Arnell et al. 2019). Humans are becoming increasingly affected; for instance, extreme temperatures contributed to 53,000 excess deaths across the European continent in July 2022 (Haines et al. 2006; Mandiá & Nissi 2022). Therefore, climate change presents a plethora of social, environmental, political and economic challenges. One significant challenge is the effective management of climate-induced human migration – trends show that an increasing number of people are fleeing their homelands (due to worsening climate conditions) to relocate closer to the poles (Nerem et al. 2018). To mitigate climate change, international treaties (e.g. The Paris Agreement) have been established, with the ambition of steering political decision making to limit global temperature rise to below 2°C. However, consensus among climate scientists suggests that current policies and planned actions are of insufficient severity to steer global temperatures away from exceeding the 2°C threshold (Rogelj et al. 2016).

Increased atmospheric concentrations of carbon dioxide (CO_2) and other 'greenhouse gasses' are the main driver of anthropogenic climate change (Fahey et al. 2017). High concentrations of atmospheric greenhouse

[1] Climate simulations are unable to explain this rate of warming without including the role of greenhouse-gas pollution (Schiermeier 2010) – there is no evidence to suggest that these changes are caused by natural climate cycles alone.

gasses intensify the 'greenhouse effect'; a natural climate process which modulates the amount of solar energy absorbed by the Earth. The largest contribution to global greenhouse gas emissions is from the combustion of fossil fuels (e.g. coal, oil and gas) to supply energy. The First Industrial Revolution (1760-1840) marked the beginning of widespread fossil fuel use, since then, humans have deeply intergrated hydrocarbons into modern life. In 2021, 61.3% of global electricity was generated using fossil fuels (BP 2021). Due to extensive exploitation and utilisation, fossil fuel reserves are expected to be depleted within 53.5 years for oil, 48.8 years for natural gas, and 139 years for coal (BP 2021). However, global energy demand, namely electricity is predicted to increase due to population growth (global population is predicted to peak in 2064 at 9.7 billion; Vollset et al. 2020), a rise in global living standards (in 2010, 1.27 billion people did not have access to electricity; Agency 2009) and the electrification of fossil fuel powered sectors (Ahmad & Zhang 2020). In the UK, annual electricity usage is forecasted to increase to 423 TWh by 2050 (for context, in 2010 annual demand was 340 TWh), furthermore peak load demand is predicted to double by 2050 (Boßmann & Staffell 2015). Renewable energy has been recognised as part of the wider solution to the trilemma of challenges which cannot be addressed by fossil fuels: rising energy demands, energy security and climate change (Cronin et al. 2018).

Globally, the renewable energy sector has seen substantial growth in the past decades – from 2013 to 2018 the global renewable energy capacity grew by 50%, from 1563 to 2351 GW (IRENA 2020). This growth is forecasted to continue with global renewable capacity projected to increase by a further 75% between 2022 and 2027 (IEA 2022). In addition to the environmental benefits (e.g. reduced air pollution and climate change mitigation), there are wider social and economic advantages associated with switching to renewable energy. Firstly, renewable energy offers the prospect of decentralisation; communities can use their local renewable resource to independently generate power, increasing energy security and resilience. Secondly, renewable energy is denuded of high price volatility, unlike fossil fuels, the price of renewable energy is not influenced by unpredictable developments in international politics and global markets. Lastly, the maturation of renewable technology is driving a steep, continuous decline in levelised cost, which in-turn increases accessibility. For instance, since 2010 the cost of individual solar modules has decreased 91% and

the price of onshore wind (to the consumer) has declined 68% (IRENA 2022).

In 2019 the UK became legally obliged to generate 100% of electricity from non-carbon emitting sources by 2035; part of the UK's net zero by 2050 target (Gov 2019). As of 2019, the UK generates an estimated 308 TWh of electricity per year, around 40% of which is produced using fossil fuels (Department for Business & Strategy 2020). The UK's net zero target, combined with decreasing cost and technology readiness level, have resulted in an increase in demand for carbon-free electricity – this has propelled the UK's renewable sector (namely solar and wind energy; Schmidt et al. 2019). From 2009 to 2020, the UK's onshore and offshore wind electricity generation increased 715%, and by 2021 wind energy supplied 21% of annual electricity usage (at its peak supplying around 50% of national electricity demand; BEIS 2023). However, to meet rising electricity demands and carbon emission targets, the UK requires further expansion and diversification of its renewable energy portfolio (Shmelev & Van Den Bergh 2016). This is evident in the projected expansion of offshore wind, where electricity generation is forecasted to increase five-fold by 2030 (from 10 GW to 50 GW).

For efficient integration into national grid systems, electricity sources must exhibit the following characteristics: predictability (known output at any given time), reliability (a consistent baseload output) and dispatchability (can be turned off and on; Neill & Hashemi 2018). Despite the technological readiness, price competitiveness and recent growth in wind and solar; these renewables deliver an electricity output which is unpredictable over medium to long-term time horizons (i.e. weeks to years; Engeland et al. 2017). Weather conditions (e.g. wind velocity for wind-driven power) determine electricity generation, as a result, reliable forecast of electricity output can be a challenge to acquire given the stochastic nature of local weather (Li et al. 2023). Renewable energy sources which are sensitive to weather conditions are susceptible to sudden 'energy droughts', reducing the reliability of the grid system (Raynaud et al. 2018).

Tidal energy is a predictable, but intermittent and variable, form of marine renewable energy. There is significant potential for tidal energy in the UK's shelf seas – these waters host 13% of the global tidal range resource (Neill et al. 2016). High power density regions of tidal range and tidal stream resource are widely distributed in areas such as the Irish Sea, these resources are almost fully untapped. Two main approaches

to harvesting tidal energy exist; tidal range and tidal stream. Tidal stream energy involves converting the kinetic energy stored within horizontal flow of tidal currents into electricity using turbines, analogous to wind energy. Tidal range energy relies on the use of an artificial impoundment structure (known as a tidal range scheme, TRS, or tidal range power plant). The TRS facilitates a tidally-driven water level difference between the ocean and an impounded water basin. At optimal times in the tidal cycle, water is funnelled between the ocean and the basin, passing through low-head hydroelectric turbines embedded in the structure (generating electricity). Tidal range power plants can be categorised based on their impoundment perimeter, two popular types are barrages and lagoons. However, since the construction of the first tidal barrage in the 1960s, tidal barrages have become associated with substantial environmental disruption due to the high blockage ratio and the innate ecological sensitivity of coastal sites (Xia et al. 2010). Recent commercial and academic attention has been centred on the concept of tidal lagoons[2] – perceived as the next generation of TRS. Tidal lagoons can be sited in less valuable ecological space (they are therefore predicted to cause less environmental disruption).

Despite the great potential for TRS in the UK, the technology has not yet come to fruition due to a handful of technical and economic challenges (Segura et al. 2017). Perspectives from the tidal lagoon industry suggest that the primary barrier to development has been uncertainty around the environmental impacts and sensitivity of these changes to the design parameters of tidal lagoons (e.g. impoundment size). The operation of TRS are understood to alter hydrodynamics both in the local and wider region of the structure. However the far-reaching effects of tidal lagoons on shelf sea processes, in particular macro-tidal dynamics, sediment transport and morphodynamics are yet to be comprehensively characterised. Due to the long lifespan of TRS (often cited as 120 years or more), it is also important to understand how they will interact with multi-decadal processes such as sea level rise and nodal tidal cycles (Neill et al. 2018).

[2]There are no operational tidal lagoons.

2.2 Shelf Sea Dynamics

Shelf seas are the submerged extension of the continental shelf, these regions are geologically distinct abyssal ocean, they are typically defined by shallow water less than 250 m deep. A more abstract definition may delineate a shelf sea by the change in the type and intensity of physical oceanographic processes (Simpson & Sharples 2012). By area, shelf seas make up 9% of the global ocean, encompassing many physiographic regions (e.g. estuaries, coastal lowlands and deltas). Many of these regions provide important services for human societies around the world (Masselink et al. 2014); 22 out of the 32 largest cities are located adjacent to estuaries (Ross 1977). Shelf seas have high rates of biological activity, they support 15-20% of global primary productivity making them critical in the cycling of elements (e.g. sequestering atmospheric carbon; de Haas et al. 2002). The shallow seas are vast food source, providing approximately 20% of the protein intake for a third of the worlds population (Bianchi et al. 2014). Our understanding of these systems is fundamental to our ability to predict how human activities may impact the functioning of benthic and pelagic ecosystems.

The physical processes which operate within shelf seas are dynamic in nature, highly variable in space and time, and sensitive to inital conditions. Generally, there are three inter-linked physical components to shelf sea dynamics: (i) hydrodynamics, (ii) sediment transport and (iii) morphodynamics (Fig. 2.1). Hydrodynamic flows determine the spatial patterns of erosion and deposition (through sediment transport), which in turn promotes morphological adjustment (or bed evolution), this further modifies the flow field due to changes in the roughness of the bed (Wright 1995). Sediment transport is the time-dependant coupling mechanism through which morphological adjustment occurs (Cowell & Thom 1994). If sediment supply and hydrodynamic conditions are relatively stable over long time periods, the morphology of the system will approach, and eventually reach, a quasi-equilibrium state. Over short time periods, perturbations of either natural or anthropogenic origin can upset this balance (Masselink et al. 2014).

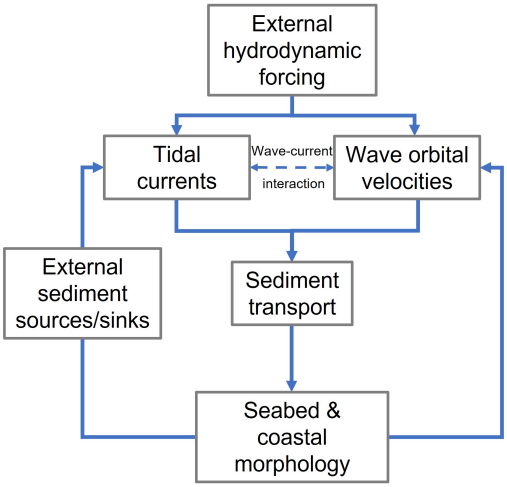

Figure 2.1: A basic model of shelf sea processes and their interactions. External sediment sources can be rivers or coastal erosion, sediment can be removed from the system (sink) when transported off the continental shelf or deposited and compacted.

2.2.1 Hydrodynamic Processes

Shelf sea hydrodynamics are driven by interactions between tidal elevations and currents, wind action, surface waves, geostrophic currents, density currents, internal waves and fresh water discharges (Fig. 2.2) – each of which operate on distinct temporal and spatial scales (Fig. 2.7a and 2.7a). Each shelf sea region has a unique combination of hydrodynamic drivers. For example, across the North-west European shelf, suspended sediment concentration and sediment transport is primarily driven by the asymmetric nature of the tidal currents (Wang 1989; Neill et al. 2017; Franz et al. 2017). Coastline geometry, basin morphology and climate have a strong influence on the relative dominance of each process.

Astronomical Tide

Tides are long-period ocean waves generated by gravitational attraction from the Moon and Sun (Pugh 1996). We can describe how tides are fundamentally generated using the equilibrium tidal model (a commonly used framework; Sverdrup et al. 2006). In the model, we assume that Earth is an idealised body,

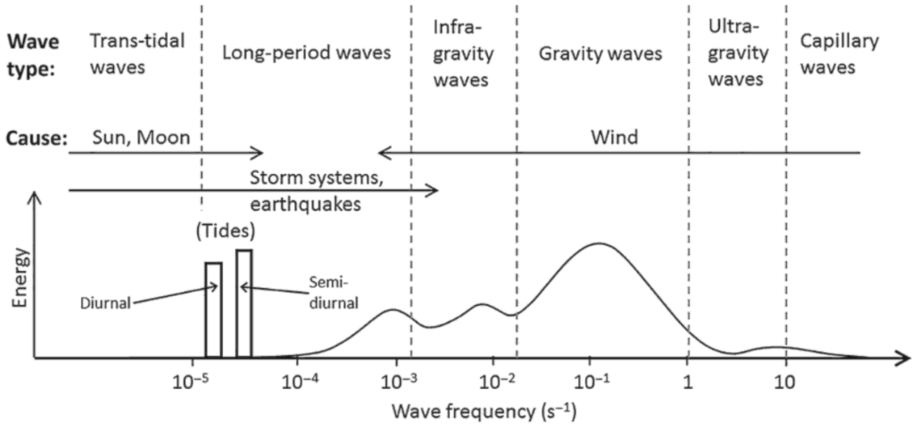

Figure 2.2: Types of ocean wave and their associated frequency and energy (Neill & Hashemi 2018).

Table 2.1: Characteristics of various ocean wave types (Toffoli & Bitner-Gregersen 2017).

Classification	Period band	Generating forces	Restoring forces
Capillary waves	<0.1 s	Wind	Surface tension
Ultragravity waves	0.1–1 s	Wind	Surface tension and gravity
Gravity waves	1–20 s	Wind	Gravity
Infragravity waves	20 s to 5 min	Wind and atmospheric pressure gradients	Gravity
Long-period waves	5 min to 12 h	Atmospheric pressure gradients and earthquake	Gravity
Ordinary tidal waves	12–24 h	Gravitational attraction	Gravity and Coriolis force
Transtidal waves	>24 h	Storms and gravitational attraction	Gravity and Coriolis force

completely covered in a uniform depth of water and the only gravitational influence is the moon. The Earth and the Moon revolve around a common point (known as the centre of gravity; Macmillan 1966); for the Earth-Moon system this centre point is around 1700 km below the surface of Earth (Neill & Hashemi 2018). Newton's law of gravitation defines the gravitational force as inversely proportional to the square of the distance between two masses. Therefore, on Earth, the magnitude of gravitational attraction progressively weakens away from the Moon. Inertia (also known as the centrifugal force) is a fictitious force which directly opposes gravitational attraction. The centrifugal force is experienced equally throughout all rotating bodies, therefore all locations on Earth experience the same magnitude of centrifugal force, whereas the gravitational force decreases away from the common centre of gravity. Therefore, imbalances occur and produce a resultant force which generates two opposing bulges (as shown on the right side of Fig. 2.3).

In reality, multiple celestial body exert varying magnitude of gravitational attraction on the Earth. The gravitational attraction from each tide-generating body produces its own two bulges each of unique frequency and amplitude (known as equilibrium tidal constituents). These tidal constituents combine to produce the resultant tidal curve that can be observed at discrete points across the global ocean. The frequency of the equilibrium constituent is determined by the length of time it takes for the Earth to complete one full revolution relative to the orbiting body. The magnitude of the constituent is based on the proximity and mass of the celestial bodies. The Moon and the Sun produce the dominant gravitational forces – the Moon exerts a force 2.2 times larger than that of the Sun (Rourke et al. 2010). The principal lunar semi-diurnal tide (known as M_2), the main component of the tide in many places, has a period of 12 hour and 25 minutes (half a lunar day). Detailed characteristics of the various other key tidal constituents are shown in Table 2.2.

Periodic variations in the magnitude of tide generating forces arise due to the changing angles (alignment and disalignment) between the Moon and Sun relative to the Earth. For instance, when the Earth, Moon and Sun are aligned (moon syzygy) the gravitational forces act constructively to create high amplitude *spring tides* (Fig. 2.4, a). On the other hand, *Neap tides* (low amplitude tides) occur when the sun and moon are perpendicular to each other (known as a moon quadrature, Fig. 2.4, b). In addition, the Moon

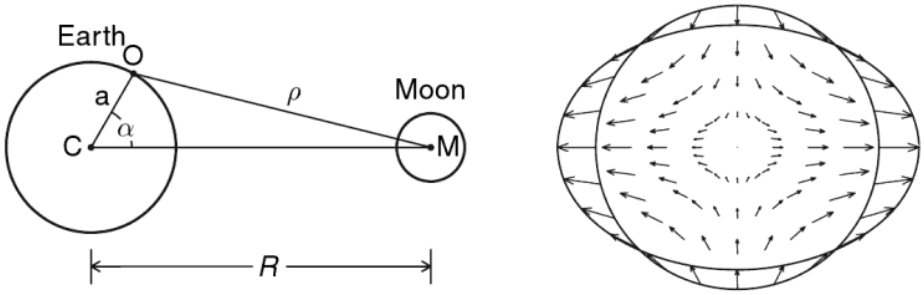

Figure 2.3: A diagram of the tide generating forces. The left diagram is a geometric depiction of generating forces. Force imbalances which generate the tides is shown on the right (modified from Agnew 2010).

and Sun both exhibit elliptical orbits, this causes the distance between each body to change over each orbit. Once a month, the Moon is closest to the Earth at *perigee* and most distant at *Apogee*, this causes one large and one small amplitude spring-neap cycle per month (Fig. 2.4c).

The equilibrium tidal model does not accurately explain the tidal elevations and current velocities observed on Earth. This is because the assumptions made in the equilibrium tidal model neglect the effects of (i) *rotation*, (ii) *friction*, and (iii) *basin topography*. Due to the ignorance of friction, the ocean is considered to instantly respond to changes in tractive forces (Macmillan 1966). In reality the peak of the tidal wave travels at an average speed of around 200 ms^{-1}, not fast enough to remain in the meridian of the moon (a point on the Earth's surfaces moves at 460 ms^{-1}; Twidell 2021). Furthermore, Earth's *rotation* which causes the Coriolis force is not considered, this effect has significant impact on the propagation of tides (Neill & Hashemi 2018). Basin topography (i.e. the presence of continents) blocks, deflects, constricts, amplifies, reflects/resonates, and delays the progression of the tidal waves, therefore the observed tides are largely affected by water depth (further explained below).

The effects of basin topography can be understood by considering the behaviour of a tidal wave in *deep water* and *shallow water*. Deep water tidal waves propagate in a linear fashion, where the frequencies of tidal constituents relate to lunar or solar days, therefore they can be expressed in terms of diurnal and

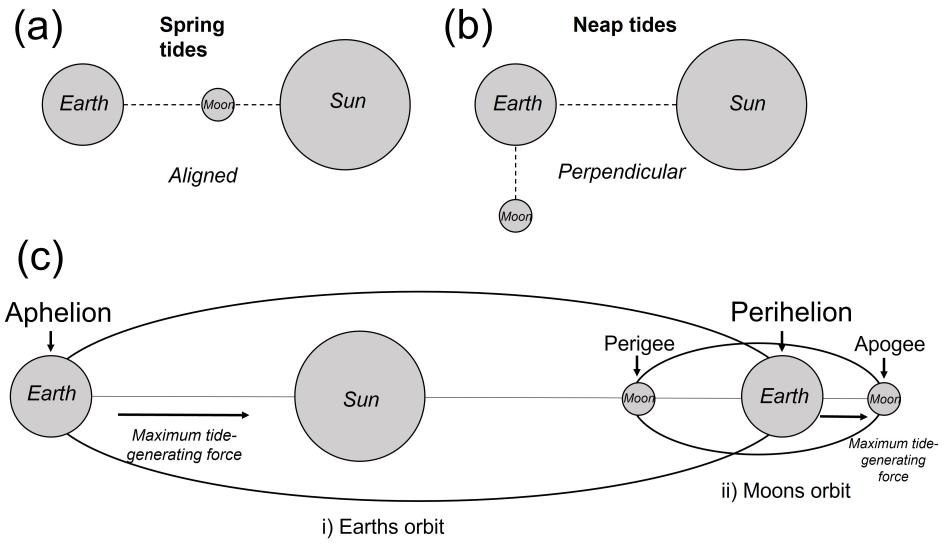

Figure 2.4: Astronomical configurations which drive key tidal cycles, (a) spring tides, (b) neap tides, (c) the (i) equinoctial solar cycle and (ii) monthly lunar cycle.

semi-diurnal components. In these mid-ocean regions, tidal range is usually around 0.6 m and currents are negligible (Twidell 2021). Locations with zero tidal range are known as amphidromic points; these points are typically located in deep offshore waters (Garrison 2012). Surface (barotropic) and internal (baroclinic) tides are observed in the ocean, the latter form due to stratification and generally have little effect on the oscillations of the sea surface (Cummins & Oey 1997).

In shallow waters, the propagation of the tidal wave becomes more complex, due to non-linear forces, interactions with reflected tidal waves, advection (due to advective forces), friction and diffusion (due to turbulence). These processes complicate and distort the tidal signal, as a result, it cannot be described by simple linear superposition of semi-diurnal and diurnal components. Local factors such as seafloor topography and coastline morphology directly influence the local properties of the tidal wave (i.e. amplitude and phase) by either amplifying or suppressing certain tidal constituents (as shown in Fig. 2.5; Egbert & Ray 2003). As a consequence, in some locations, the semi-diurnal constituents are suppressed leading to mixed-semi-diurnal or diurnal tides.

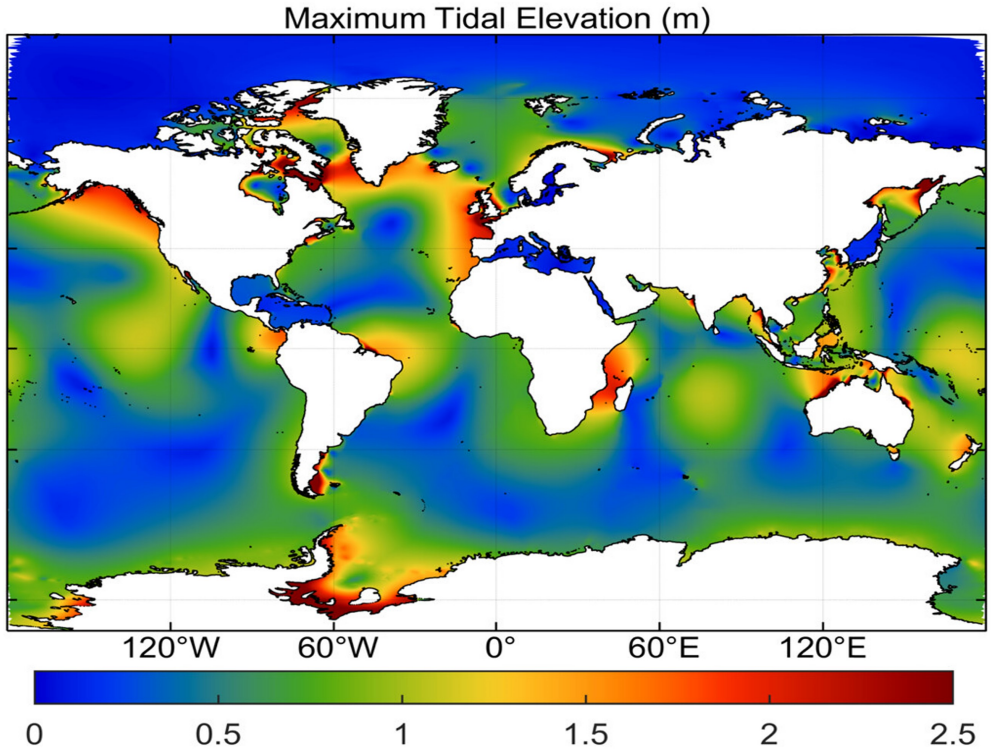

Figure 2.5: Global distribution of tidal elevation (edited from Blakely et al. 2022).

Tidal range varies significantly across the oceans (Hicks 2006). Regions of high tidal range are patchy and synonymous with bays, estuaries and coastlines where local effects such as *resonance*, *funnelling*, *shelving* and *reflection* cause an increase in the amplitude of harmonic constituents (Hammons 1993). Resonance occurs when a fluid body is subject to an impulse at a frequency that is close to its natural frequency (Pugh 1981). The first significant resonant effects arise when the natural frequency (due to coastline geometry) is around one-quarter of the tidal frequency (Huthnance 1980). For example, in the Severn Estuary (UK) the natural frequency is 36,400 $m^{1/2}$ and the tidal frequency is 36,000 $m^{1/2}$ (Twidell 2021), therefore strong resonant effects arise. Funnelling mainly occurs in estuaries, where the rapid decrease in water depth forces water to pile up, increasing water levels away from the estuary mouth (Twidell 2021). Tidal analysis involves defining the amplitude and phase of the periodic geophysical forces which drive the tidal movements. Harmonic analysis (a method of tidal analysis) uses the Fourier method to deconstruct

the tidal signal (from a timeseries of sea level measurements) and find the amplitude and phase of each individual cosine curve (i.e. the harmonic components). The period of the individual cosine waves, which compound to form the tidal wave, can be described in mean solar hours or, by their speed in degrees per mean solar hour (speed = $360°/T$, where T is period). Harmonic analysis is based on the assumption that tidally-driven surface variations can be represented by a number tidal constituents, in the form:

$$H_n cos(w_n t - g_n) \tag{2.1}$$

where n is the component index, H_n is the component amplitude, w_n is the component angular speed $2\pi/T_n$, T_n is the component period, g_n is the component phase lag relative to some defined time zero (commonly taken as the phase lag on the equilibrium tide phase at the Prime Meridian) and t is time (relative to 0 hour at Greenwich Mean Time; GMT; Cartwright & Tayler 1971).

The superposition of tidal constituents can be used to predict water level ζ (at high degrees of accuracy) as a function of time at a specific location, from the following relationship:

$$\zeta = \sum_{n=1}^{N} f_n A_n cos[w_n t - G_n + (V_n + u_n)] \tag{2.2}$$

where f_n is the nodal factor of the tidal constituent, w_n is the frequency of the tidal constituent, $(V_n + u_n)$ is the value of the equilibrium argument of the tidal constituent, V_n is the uniformly changing phase of the constituent at the Greenwich meridian; and u_n is the nodal adjustment of the tidal constituent (Dronkers 1964). Equation 2.2 can be used in numerical modelling to define the water depth h in the shallow water equations (introduced in Section 2.6.1) at the open boundaries of the computational domain.

Analysis of the global tides has revealed 388 distinct tidal frequencies (Casotto & Biscani 2004), although only around 40 harmonic components are necessary to explain the observed tidal signal at one individual location (Butikov 2002). The most influential tidal constituents are shown in Table. 2.2.

Meteorological Effect

A timeseries of sea level, measured at a single location, is unlikely to directly correlate with the amplitude of the astronomical tide. Meteorlogical processes such as air pressure and wind shear can have strong influ-

Table 2.2: Principal tidal constituents and their associated equilibrium amplitudes from Apel (1987). The top 7 tidal constituents describe over 80% of the variability observed in Earth's tides (Kvale 2006).

Tidal constituents	Symbol	Equilibrium amplitude (m)	Period (h)
Semidiurnal			
Principal lunar	M2	0.24	12.42
Principal solar	S2	0.11	12.00
Lunar elliptical	N2	0.046	12.66
Lunar-solar declinational	K2	0.031	11.97
Diurnal			
Lunar-solar declinational	K1	0.14	23.93
Principal lunar	O1	0.10	25.82
Principal solar	P1	0.047	24.07
Lunar elliptical	Q1	0.019	26.87
Long period			
Fortnightly	Mf	0.042	327.9
Monthly	Mm	0.022	661.3
Semiannual	Ssa	0.019	4383

ence on sea level. Atmospheric pressure is inversely related to sea level, hence a reduction in atmospheric pressure will cause a rise in sea level (Pugh 1987). In addition, strong on-shore winds and/or waves can pile water up against the coastline, causing a local increase in sea level (i.e. wind setup and wave setup). A strong alongshore wind combined with the Coriolis force, can raise or lower the sea level (depending on direction). The climatic (or surge) component of sea level displays large spatial and temporal variation; generally, it is larger in the winter, when storms are stronger and more frequent. Large-scale climatic events such as the North Atlantic Oscillation (NAO) have also been shown to influence the variability of sea level (by 96mm per unit NAO index; Wakelin et al. 2003).

Coriolis Effect

The Coriolis effect is considered a fictitious force (akin to the centrifugal force) because it arises due to the use of stationary coordinates in a rotating system. The effect occurs because a point on Earth's Equator is moving faster than at the poles (where there is no motion). Objects moving away from the Equator are deflected to the right, whereas when moving towards the Equator objects are deflected to the left (as depicted in Fig. 2.6). As a result, large-scale oceanographic and atmospheric phenomena (e.g. tidal amphidromic systems) rotate counter-clockwise in the Northern Hemisphere and clockwise in the Southern Hemisphere.

2.2.2 Sediment Transport Processes

Sediment transport arises due to the action of currents and waves on the seabed. The drivers of transport vary in space and time, therefore the transport can be *current-driven*, *wave-driven* or occur under the conditions of *wave-current interaction* (Soulsby 1997). Sediment properties such as grain size, cohesiveness, density and porosity will determine how a sediment bed will respond to hydrodynamic forces. Sediment transport rates are notoriously difficult to predict. This is primarily attributed to the inter-connectivity between each process, for instance sediment motion reduces the energy within the flow, which in-turn decreases the flow velocity and promotes bed evolution which further modifies the flow field.

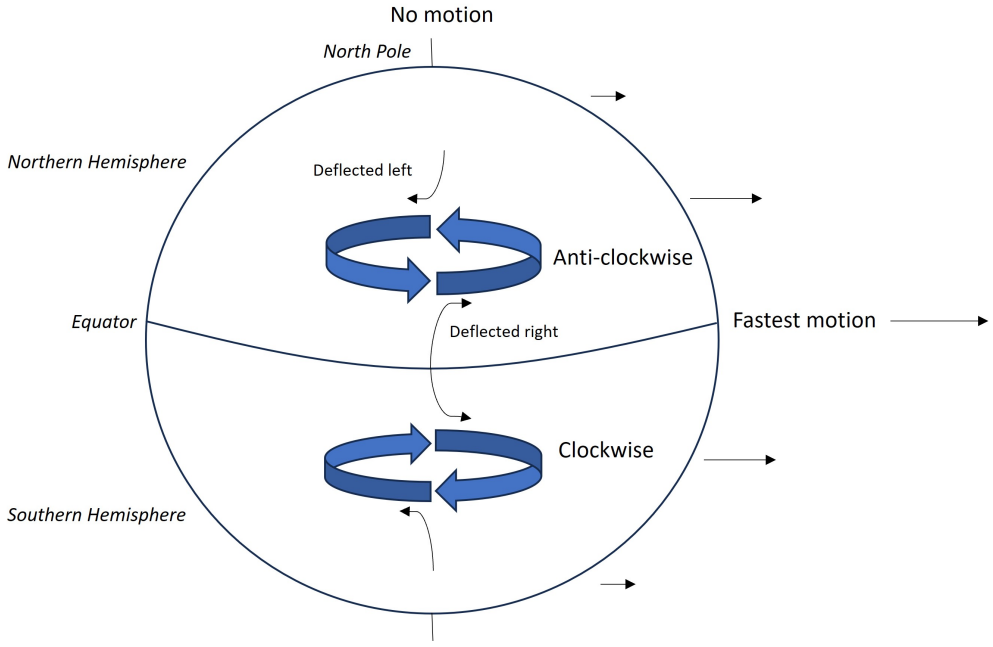

Figure 2.6: A diagrammatic explanation of the driving mechanism behind the Coriolis effect.

When the bed (or boundary) shear stress τ_b exceeds the critical shear stress τ_c (expressed as $\tau_b > \tau_c$), grain motion is initiated at the bed. Sediment particles are transported as *bed load* or *suspended load* (Fredsøe 1993). Bed load transport occurs in a thin near-bed layer where contact between particles and the bed are common and inter-particle interactions influence transport capacity. The suspended load is transported in the water column between the top of the bedload layer and the free surface, the vertical flux of turbulent motion is important to initiate and sustain *suspended load* transport. Sediment suspension occurs when there is sufficient lift to negate inter granular friction, the vertical turbulent flux is then able to carry the particles in suspension. The concentration of suspended sediment has been shown to decrease with distance from the bed, the rate of decrease depends on the ratio between the fall velocity and the bed-shear velocity (Van Rijn 2013).

A variety of semi-empirical sediment transport formulae have been derived. Although the specifics of each equation differ, in general bed shear stress is a function of current speed squared U^2, further to that, the sediment transport (suspended load and bedload) is a function of $U^{3.4}$ (for marine sand; Soulsby 1997).

Therefore, seemingly trivial changes in current velocity can have significant implications for sediment transport rates.

Current-driven Transport

In tidally-driven shelf seas, tidal asymmetry plays a crucial role in defining the magnitude and direction of residual sediment flux. Tidal asymmetry is the deformation (or distortion) of the tidal wave whereby the flood period and the ebb period become unequal. In shallow water, the non-linear forces: friction, advection, inertia force and diffusion due to turbulence, generate compound and overtides. The type of tidal asymmetry (i.e. ebb or flood dominant) depends on the relationship between the phase and amplitude of the principle and additional constituents (Robins & Davies 2010). Generally, shallow systems with large intertidal basin storage tend to be flood-dominant and enhance landward near-bed transport, whereas deep tidal basins with little intertidal basin storage tend to be ebb-dominant Wang et al. 2002. The generation of M_4 and its addition to the M_2 constituent commonly arises in shelf seas which exhibit a semi diurnal regime (Aubrey & Speer 1985; Speer & Aubrey 1985). Therefore, in many shelf seas (such as the North-West European Shelf), tidal asymmetry determines the spatio-temporal pattern of: sediment transport, pollutant dispersal, bio-biochemical pathways and seabed morphological evolution (Pingree & Griffiths 1979; Dronkers 1986; Zhang et al. 2018).

Morphodynamics

Coastal morphodynamics refers to the evolution of the seabeds shape and coastline over time (Neill et al. 2017). Seabed sedimentary structures can be differentiated by spatial scale, from current-generated tidal sandbanks with length scales in the order of kilometers (Dyer & Huntley 1999), to wave ripples which are often measured in centimetres (Fig. 2.7b). The size and shape of each structure determines its hydraulic roughness k_s, which in-turn describes the extent to which it will interact with the flow field, and alter local flow patterns. Large sedimentary structures (such as offshore sandbanks) have the potential to cause wave refraction, diffraction, reflection and breaking, whereas small bed forms (such as wave ripples) have

negligible impact on dominant flow patterns but they can influence the structure of the boundary layer. Morphodynamic change can be artificially induced by sub-marine structures or objects, this is known as scour (erosion) and burial (deposition). Scour and artificial modifications to sedimentary structures can have wider implications for beach stability, coastal ecology and flooding (Neill et al. 2012). For instance, sandbanks mitigate against coastal flooding and erosion by dissipating tidal currents and wind-wave energy. Anthropogenic sea level rise will reduce the ability for sandbanks to dissipate wave energy increasing nearshore wave height and tidal velocity (Neill et al. 2012). It is therefore ever important to develop a comprehensive understanding of the evolution of such features to asses the risk of coastal flooding.

Sediment

As mentioned in Section 2.2.2, knowledge of sediment properties (size, shape and density) is vital in sediment transport prediction. Sediment properties determine the critical bed shear stress required to entrain and transport a particle. Therefore, it is important to discuss methods of grain size classification and the different types of marine sediment.

A common classification is grain size based on the length of a sediment particles longest axis. In shelf seas, sediments can vary from large boulders (>600 mm) to very fine clay (< 0.002 mm). Grain size is commonly measured using the median grain size (d50); the grain diameter for which half of the sample (by mass) is smaller than. Shelf sea sediment can also often be distinguished by origin. Terrigenous material, derived from erosion of the land (termed allochthonous), is most common in shelf seas. Whereas, material produced within the marine environment (termed autochthonous) is generally less widespread. Furthermore, sediments can be either non-cohesive (clastic/granular) or cohesive (floccular). The behaviour of cohesive sediments is influenced by electrostatic forces which complicate processes such as erosion, transportation and deposition.

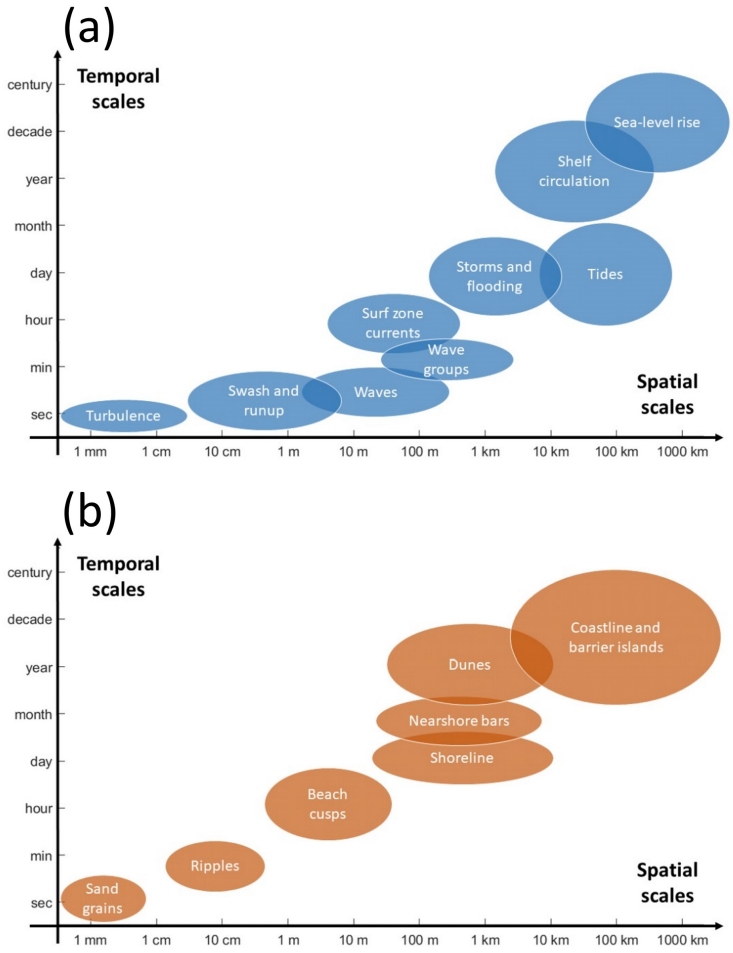

Figure 2.7: Temporal and spatial scales of coastal/shelf sea (a) processes and (b) morphological features (edited from Yates 2019).

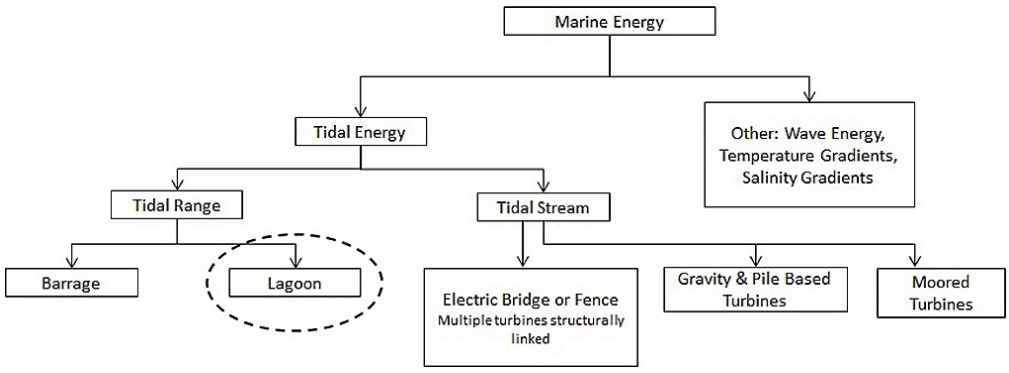

Figure 2.8: Classification of marine renewable energies by Elliott et al. (2018).

2.3 Tidal Energy

Ocean energy or marine energy (used hereafter) refer to the conversion of the energy carried within the ocean body into useful power forms such as electricity. There are four types of marine renewable energy: wave, tidal (stream and range), ocean currents, salinity gradients and temperature gradients (shown in Fig. 2.8; Taveira-Pinto et al. 2020). Wind-generated waves and tides represent a significant renewable energy resource, however several challenges have hindered widespread utilisation. One such challenge is the practical challenges associated with working in the marine environment, this leads to uncompetitively high capital cost of deploying, maintaining and designing MRE devices. These costs (although forecasted to decrease), slow research and development – ocean energy technologies are yet to reach commercial array scale deployment. Tidal power or tidal energy (used hereafter) is a form of marine-based hydropower. Hydropower can be defined as the extraction of energy from the flow of water by driving a hydroelectric turbine (IRENA 2020). Tidal energy benefits from high predictability: tidal cycles times and levels can be predicted on long time horizons (with ignorance to meteorlogical influence), and high power density. Water is around 800 times more dense that air, it has a high energy density which leads to a higher power yield per unit of volume. Predictability is widely recognised as the key advantage to tidal energy, allowing for accurate tidal energy resource estimations.

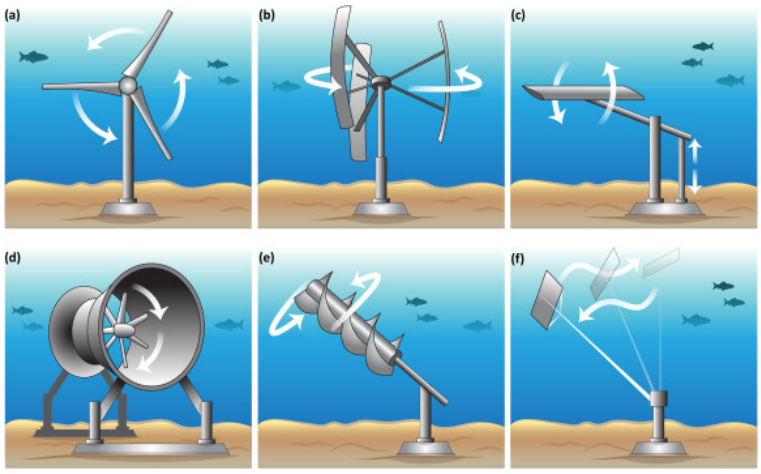

Figure 2.9: A selection of tidal stream energy turbine designs: (a) horizontal axis turbine, (b) vertical axis turbine, (c) oscillating hydrofoil, (d) venturi (or enclosed tip) turbine, (e) Archimedes screw, and (f) tidal kite (Khojasteh et al. 2022).

There are two main approaches to generate tidal energy (i) *tidal stream* and (ii) *tidal range* (Fig. 2.10). Tidal stream energy involves the use of turbines to covert the kinetic energy from the horizontal movement of tidal currents (also known as tidal streams) into useful power (Rourke et al. 2010). The power generation from tidal stream turbine is related to current velocity cubed, therefore tidal stream turbine designs are a key consideration in order to maximise energy conversion (e.g. Fig. 2.9).

2.3.1 Tidal Range Energy

Tidal range energy is derived from the gravitational potential energy created by the difference between the high and low tide (i.e. vertical movement). The conversion of the tides potential energy into useful power requires a semi-enclosed TRS. Selecting the optimal site for a TRS is crucial, a ideal location exhibits: a large mean tidal range (> 5 m, to maximise electricity generation), shallow water depths adjacent to deeper waters (to minimise construction costs) and high grid connectivity (to minimise transmission loss). There are several approaches to TRS design, the most common are the (a) *barrage* and (b) *lagoon* (Fig. 2.10). The main distinction between lagoons and barrages is in the perimeter embankments; lagoon em-

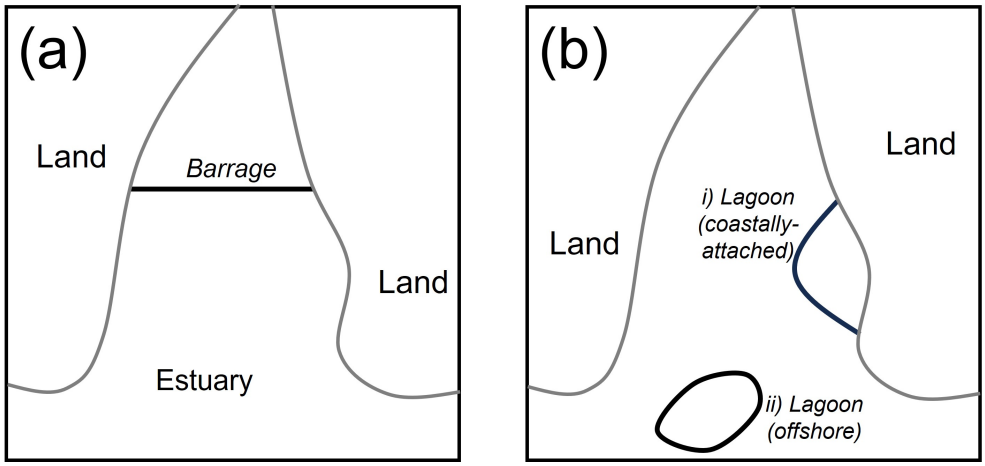

Figure 2.10: These diagrams show the key differences between a barrage (a) and coastally-attached lagoon (b, i) and a offshore lagoon (b, ii).

bankments are constructed to enclose areas either against the coastline or entirely offshore, whereas barrages span across estuaries (Commission et al. 2007).

Despite the nuances of TRS designs, the underlying principle of energy conversion remains constant. A wall (or embankment) encloses a marine area forming an isolated basin. The tide drives a water level difference between the basins, this is known as the hydraulic head h. At optimal time in the tidal cycle (defined by the operational scheme), the water flows through low-head turbines housed in the embankment (Waters & Aggidis 2016*a*). The potential energy E is described in Equation 2.3:

$$E = \frac{1}{2} A g \rho h^2 \tag{2.3}$$

where A is the area of the internal basin, ρ is the density of water and g is acceleration due to gravity (Tousif & Taslim 2011). As evidenced by Equation 2.3, energy yield is strongly related to the head difference between the impounded basin and the sea. Hence, a 1 m increase in head (from 3m to 4 m) results in a 7x increase in potential power (Hammons 1993). The average electric power generation P_{av} depends on the generation time T and the effacing of the energy conversion process ε_g:

$$P_{av} = \varepsilon_g \frac{E}{T} \tag{2.4}$$

The capacity factor CF coefficient is used to quantify the efficiency of different energy sources. The CF is defined as the ratio between the electricity generated ($E_{generated}$) and the maximum electricity ($E_{maximum}$) that could be generated if the system was operating at full efficiency over the same time period.

$$CF = \frac{E_{generated}}{E_{maximum}} \tag{2.5}$$

Several publications have estimated the CF for tidal lagoons (e.g. Petley & Aggidis 2016), results indicate that a CF around 0.2 (20%) is realistic (Todeschini 2017). The low CF is due to the intermittent nature of electricity generation and the variability in power output during generation.

There are a number of modes in which a TRS can be designed to operate. A TRS can be designed to operate in three key distinct modes: *ebb generation* (Fig. 2.11a), *flood generation* or *two-way generation* (Fig. 2.11b). Flood generation is the opposite of ebb generation, however it generally produces significantly less power. When flooding, due to the bathymetric profile, lagoons can accommodate a smaller volume of water in the lower basin (this mode of operation is considered the least favourable), whereas during ebb generation more water is available at the same operation head (Xia et al. 2010).

Pumping can be implemented to transfer water in-between basins at optimal times, increasing the impounded basin water elevation at low tide (for ebb generation) and reducing it at high tide (for flood generation). Yates et al. (2013*b*) found that pumping can increase the energy output, this has been proven by $\approx 10\%$ increase in energy output from the La Rance barrage (Hillairet & Weisrock 1986).

Tidal range structures with multiple, linked-basins have also been considered (the operational sequence of a twin-basin scheme is shown in Fig. 2.11; Angeloudis et al. 2020). This design increases the generation period, providing a near-continuous electricity supply (shown in Fig. 2.11c), at the cost of a decreased energy extraction efficiency relative to single-basin designs.

2.3.2 Resource Distribution

The predictable nature of the astronomical tides allows for accurate energy resource estimation through the use of numerical models. It is estimated that ocean tides dissipate around 2.4 TW of energy globally, only 1.7 TW of energy dissipation occurs in shelf seas (accessible for large scale civil engineering; Egbert

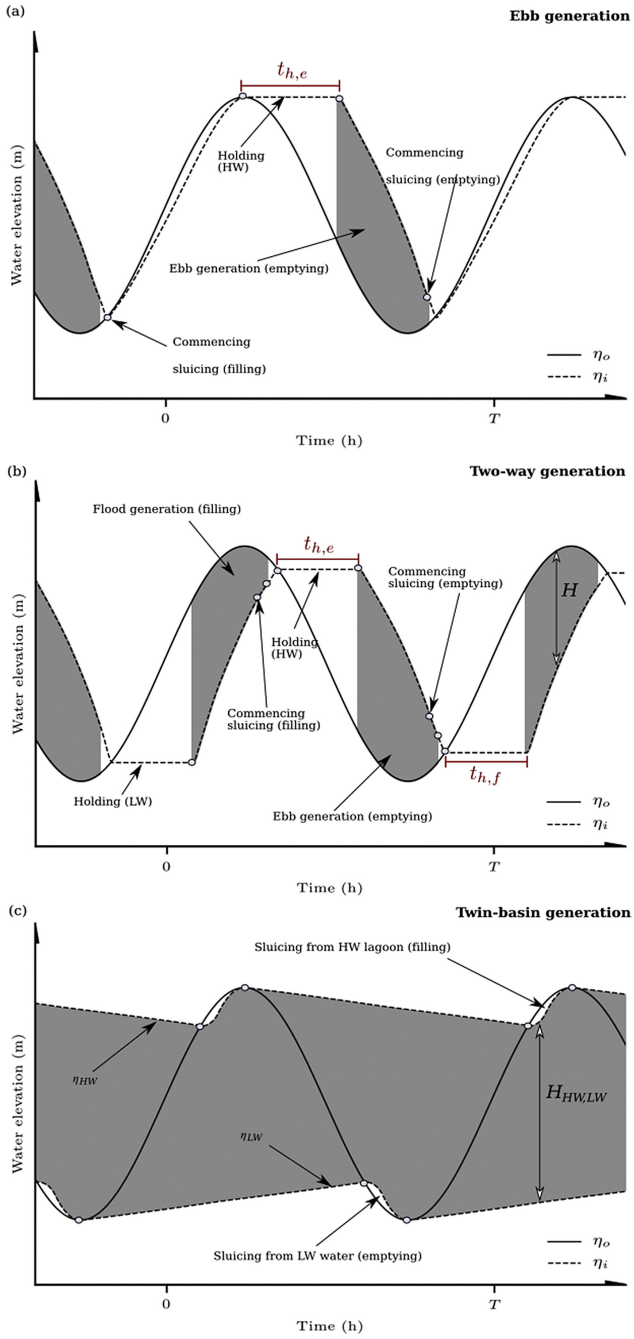

Figure 2.11: The operating sequence for (a) ebb generation (b) two-way and (c) twin basin schemes (Angeloudis et al. 2020).

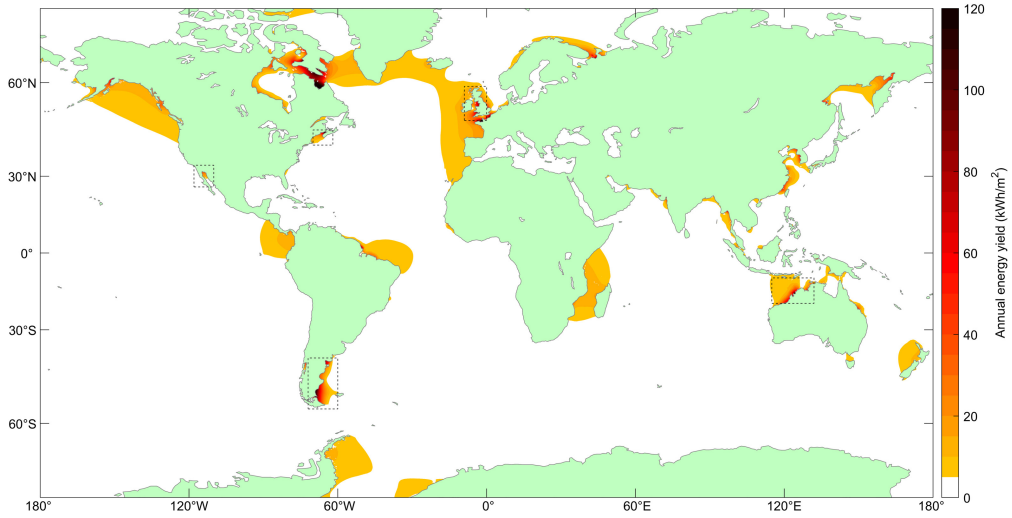

Figure 2.12: Potential annual energy yield globally for tidal energy (Barclay et al. 2023)

& Ray 2000). The shallow water depths over shelf seas amplify the tidal range (as discussed in section 2.2.1), thus the tidal range energy resource is exclusive to shelf sea regions. Principle sites for tidal energy extraction were originally identified by Hammons (1993). More recently, Neill et al. (2018) calculated the theoretical global tidal range resource at approximately 25,880 TWh (for reference, the electricity consumption of the United States in 2022 was 4,296 TWh; Ritchie et al. 2022). However, when realistic constraints are applied (e.g. excluding areas covered by sea ice such as the Hudson Bay), the annual energy resource is around 5,792 TWh – 90% of which is distributed between the following five countries: Australia, Canada, UK, France, and the US (Alaska). The UK's marine renewable energy resource has been described as 'internationally enviable' (Burrows et al. 2009), tidal energy is perhaps the most promising of the available resources. The theoretical or practical tidal range resource can be estimated. Neill & Hashemi (2018) suggested an electricity generation of 734TWh/year. With realistic constraints (excluding areas where water depth >30 m and annual yield is under 50 kWh/m^2), Neill et al. (2018) calculated the UK's total potential energy as 683TWh/year (Fig. 2.13). For context, UK electricity consumption in 2022 was 325 TWh (around half of the theoretical tidal range resource; Ritchie et al. 2022). Practical challenges with developments at this scale will render the theoretical resource an overestimation of the practical re-

source. A more realistic estimation of the power from a fleet of TRS by Estate (2012) estimated an output of 96 TWh/year (barrages) and 25 TWh/year (lagoons). The tidal range resource is also subject to non-astronomical influences (e.g. storm surges) and long-term changes to tidal cycles (e.g. due to sea level rise; these are further discussed by Neill & Hashemi 2018).

2.3.3 Existing and Conceptual Tidal Range Schemes

Harnessing tidal energy is a well-established practice, over the past 800-900 years approximately 750 tidal mills were operational (Minchinton 1979; Murphy 2005), however converting tidal energy into electricity is a relatively new concept. The first tidal barrage, the La Rance Tidal Power Station (located in France), was constructed in 1966 it has a installed capacity of 240 MW, it is arguably the most well-studied tidal barrage (Fig. 2.14; Frau 1993). The largest tidal range power plant currently in operation is the 254 MW Sihwa Lake Tidal Power Station which was constructed in 2011 (Table. 2.3; Wang & Wang 2019). At the end of 2015, the total global installed capacity for tidal power was 520 MW, 494 MW of which was contributed by the two power stations previously discussed (Todeschini 2017). A mere 10 MW of the remaining installed capacity is from tidal stream schemes (Neill 2024), there are also various multipurpose tidal power stations China which have small contributions, bringing the total global tidal range installed capacity to 500 MW (Xuemin 1985).

Tidal barrages are built across a marine area (joining two opposite coastlines) with a funnel like morphology (commonly an estuary) in locations with a high tidal range. Barrages are the most cost effective TRS design, they take advantage of coastal morphology to achieve a low embankment length to impounded water volume ratio. However, since a barrage must span across an entire estuary, suitable sites are sparse. In the early discussions of tidal barrages, developers became aware of the significant near and far-field environmental impacts after barrage construction (Mettam 1978). The concept of a tidal lagoon arose from the exploration of novel impounded designs as an alternative to tidal barrages (Waters & Aggidis 2016*a*). Tidal lagoons are considered as the next generation of tidal power plants, they offer a lower capital cost and reduced environmental impacts.

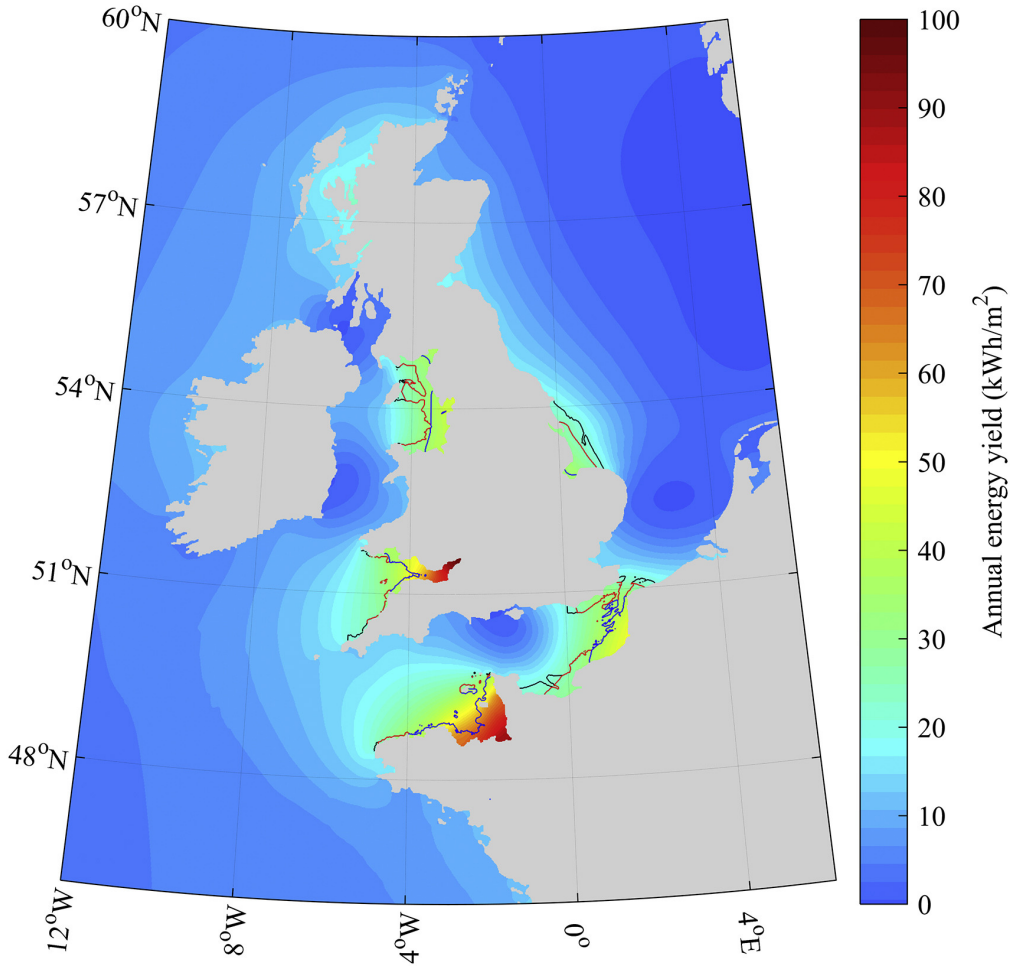

Figure 2.13: The tidal range energy resource of the northwest European shelf. The area landward of the black contour is the region in which the annual yield is above 50 kWh/m^2 (Neill et al. 2018).

Figure 2.14: The La Rance barrage which is located on the French side of the English Channel.

Table 2.3: Characteristics of operational tidal barrage schemes (edited from Neill et al. 2018). The Annapolis Royal Generating Station, Canada was a 20 MW ebb only barrage which closed down in 2019.

Power Plant	Year	Capacity (MW)	Basin area (km^2)	Operational mode
La Rance, France	1966	240	22	Two-way with pumping
Kislaya Guba, Russia	1968	1.7	2	Two-way
Jiangxia, China	1985	3.9	2	Two-way
Lake Sihwa, Korea	1994	254	30	Flood only

The UK has a long history of exploring the potential for TRS, with early investigations into the feasibility of the Severn Barrage conducted in 1925 (Langston et al. 2010). Repeated proposals for a Severn Barrage were consistently rejected due to high costs and environmental concern (James et al. 2014). In recent years, development of tidal lagoons and barrages at sites along east coast of the Irish Sea, Bristol Channel and the west coast of the North Sea has been widely investigated (Table 2.4).

A review by the UK's ex-minister of energy (The Hendry Review; Hendry 2017) strongly supported tidal energy, Hendry (2017) endorsed the development of a small-scale "pathfinder" project. The Swansea Bay Tidal Lagoon gained significant support (as a pathfinder) due to its small size (10 km^2 impoundment area), advanced state of development and proximity to the Baglan substation (part of the National Grid). However in 2018, the project was rejected by the UK government on the ground of "value for money" (BBC 2018). To date, a TRS is yet to be commissioned in the UK, with most projects dismissed due to environmental concerns. However, UK-based research has made significant contributions to understanding optimal design and operation of TRS, as well as predicting hydro-environmental impacts of barrages and lagoons.

2.3.4 Characteristics of Tidal Range Schemes

One of the main barriers to TRS development is the high economic cost associated with the civil engineering work required to construct the embankment and cofferdams. It takes decades for the electricity from a TRS to become cost competitive with other sources. For instance, the La Rance Barrage (which has been

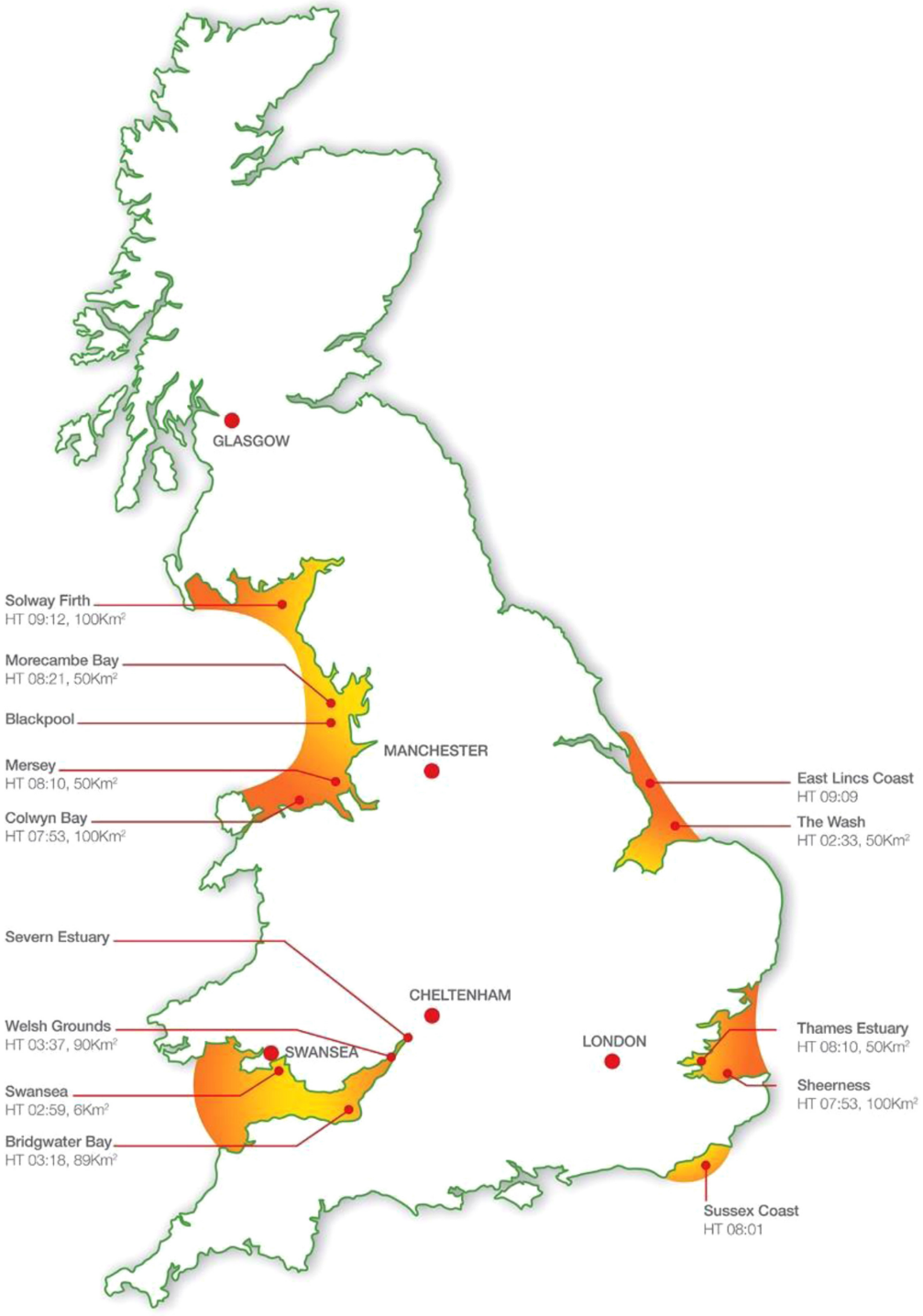

Figure 2.15: Potential tidal range energy sites around the Britain (Waters & Aggidis 2016*a*).

Table 2.4: Technically feasible tidal range locations around the UK coastline (Neill et al. 2018).

Site	Type	Mean tidal range (m)	Basin area (km^2)	Proposed capacity (MW)	Estimated annual output (TWh)
Severn	Barrage	7.0	520	8,640	17
Mersey	Barrage	6.5	61	700	1.5
Wyre	Barrage	6.0	5.8	47	0.09
Conwy	Barrage	5.2	5.5	33	0.06
Swansea	Lagoon	–	–	320	–
Newport	Lagoon	–	–	750	–
Bridgewater	Lagoon	–	–	2,000	–
Cardiff	Lagoon	–	–	1,800–2,800	–
Colwyn Bay	Lagoon	–	–	1,500	–
Blackpool	Lagoon	–	–	1,000	–

operational for 55 years) took 20 years to amortise the inital cost and become competitive with offshore wind and nuclear (Hendry 2017).

The lifespan of a TRS is often reported as 120 years (three to four times longer than wind and solar farms; Waters & Aggidis 2016*a*). With turbine replacement every 40 years and proper maintenance, it is likely that a TRS could be operational for significantly than 120 years. However, the construction phase involves mining and transporting the vast quantity of material (required to for embankment construction), estimated to have large CO_2 footprint (Kelly et al. 2012). Albeit, the remaining operational lifetime of a tidal energy power plant is non-polluting. This operational longevity reduces the lifetime CO_2 emissions – tidal energy ranks similar to offshore wind and nuclear (Table 2.5).

Two recent novel publications assessed the scope of retrofitting existing infrastructure with turbines to create tidal power plants. Negahdari et al. (2023) considered using storm surge barriers as barrages, and Hanousek et al. (2023) proposed that disused docks around the UK could be transformed into lagoons.

In the context of TRS, Multiple Use of Space (MUS) refers to the integration of other services within a the development. For the proposed lagoon in Swansea Bay, MUS included a large aqua-culture facility to improve water quality, leisure activities such as a boating centre and a tourism centre. MUS ultimately provides sustainable long-term jobs, and a sense of involvement and ownership of renewable energy projects.

Table 2.5: Technologies used to produce electricity and their associated CO2 emissions (Hendry 2017).

Technology	Median lifetime emissions (gCO_2/kWh)
Currently commercially available technologies	
Coal – PC	820
Gas – combined cycle	490
Biomass – co-firing	740
Biomass – dedicated	230
Geothermal	38
Hydropower	24
Nuclear	12
Concentrated Solar Power	27
Solar PV (rooftop)	41
Solar PV (utility)	48
Wind onshore	11
Wind offshore	12
Pre-commercial technologies	
CCS – Coal – Oxyfuel	160
CCS – Coal – PC	220
CCS – Coal – IGCC	200
CCS – Gas – Combined Cycle	170
Ocean (including wave and tidal)	17

As discussed in Section 2.1, the well established renewable energy technologies (i.e wind and solar) are subject to stochastic and intermittent power generation. The electricity produced by a TRS is intermittent (with a load factor of 22 – 35%; Hammons 1993) and variable. However, tidal range energy has the greatest potential (out of current renewable energy technologies) to deliver predictable, dispatchable and load-following generation (Neill & Hashemi 2018).

Strategies to reduce intermittency have been devised. One approach is to install a multiple out-of-phase tidal energy project (Neill et al. 2018). Despite inaccurate claims that baseload generation is possible (e.g. Yates et al. 2013*a*), across the UK high energy tidal range and stream sites are generally phase, resulting in periods of low/no generation. For example high tide in the eastern Irish Sea occurs approximately 6-hour after the Severn Estuary, therefore a TRS at each location would be at peak load during similar times. Neill et al. (2016) showed that the high energy tidal stream sites across Europe are also in phase (approximately a quarter diurnal difference). In the case of both tidal stream and tidal range, small low energy sites need to be considered to achieve a more continuous output. Mackie et al. (2020) concluded that continuous output can be attained for 241 days per year from three Irish Sea lagoons, it would however require subsidisation, being less economical than simply maximising power output.

Energy storage is the main challenge with intermittent energy production. Hybrid systems which link tidal power generation to a hydrogen storage system to meet specific power demand patterns (Procter et al. 2022). Pumping is a strategy used to attain the highest power generation consistently throughout the month, it involves transferring additional water inside the basin using the bulb turbines. Pumping is used at the La Rance power station, it has improved electricity yield by approximately 10% (De Laleu 2009).

To date, the most renowned barrier to TRS development has been the environmental impacts. This is especially apparent in the UK where multiple tidal barrage and lagoon proposals (e.g. Severn Barrage and Swansea Bay Lagoon) have been rejected in-part due to uncertainty around the severity of potential environmental issues. It is widely acknowledged that TRS can cause significant perturbations to shelf sea processes (Fig. 2.16).

Hydro-environmental impacts include the alteration of the hydrodynamic regime which directly impacts

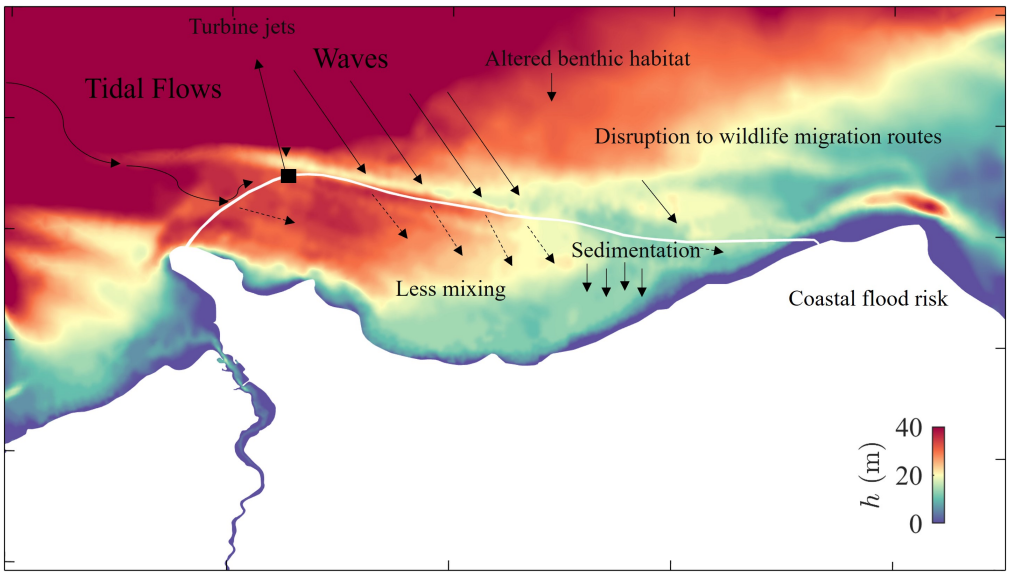

Figure 2.16: Hydro-environmental impacts of TRS, these impacts are commonly predicted in hydrodynamic simulations.

tidal range, residual currents, the intertidal area. Changing the residual current patterns has knock-on consequences for sediment transport pathways and suspended sediment concentrations. Water column properties (e.g. dissolved oxygen and salinity) will be modified, through changes in the suspended sediment concentrations (e.g. Fig. 2.17). Furthermore, reduced mixing rates can cause poor water quality inside the lagoon, due to the a lack of dilution and dispersion of effluents. Concerns have been raised regarding the impacts of fish, in particular migratory species as well as the wading bird species which may suffer from a change in intertidal area. The accuracy and reliability of the predicted hydro-environmental impacts relies solely on the standard of the numerical modelling approach.

2.4 Modelling Tidal Range Schemes

With no operational tidal lagoons, their hydro-environmental impacts cannot be directly measured. Therefore, the assessment of tidal lagoon proposals relies on the use of either (i) *numerical* (Neill et al. 2018) or (ii) *physical* models (e.g. James et al. 2014). In many instances, numerical models are advantageous –

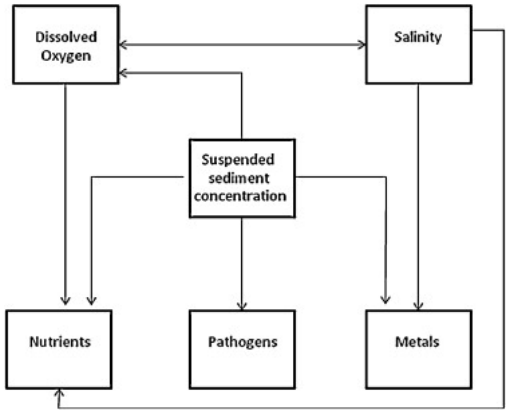

Figure 2.17: Interactions between suspended sediment concentrations and other water column properties (Kadiri et al. 2012)

.

they are more cost competitive and versatile. One key drawback of physical models is that the scale of the model is often constrained by the laws of dynamic similarity (Hughes 1993). As a result, numerical models are commonly used in many stages of TRS development from the initial resource assessment to environmental impact studies.

Hydrodynamic and morphodynamic models have been applied to solve problems in the realm of coastal processes since the 1980s (Van Rijn 2013). Numerical models provide a mathematical representation of real world processes such as sediment transport. Solutions are obtained by solving partial differential equations at discrete grid points. A combination of numerical solutions are often used and empirical equations can be implemented to parameterise sub-grid and neglected processes (i.e. turbulence).

To obtain reliable results from a numerical model care must be taken when selecting the model type, parameters and input data. Numerical models must be extensively validated using observational data. Once a fully validated ambient model is established, a TRS can be incorporated into the model. This yields a powerful tool to explore different aspects of TRS development before a significant financial commitment is made (Neill & Hashemi 2018).

Individual numerical modelling techniques range from highly simplified theoretical and zero-dimensional

models to multi-dimensional hydro-environmental models (Fig. 2.18; Angeloudis & Falconer 2017). In TRS development, the specific approach is chosen based upon the modelling objective. Simplified zero-dimensional (0D, e.g. Prandle 1984) and one-dimensional (1D) models are commonly used in preliminary resource assessments and optimisation analysis. Using a 0D model, it is possible to simulate the overall performance of a tidal structure given the tidal conditions, operational sequence and turbine performance. 0D models are essential when finding optimal operation parameters (e.g. start and end head – for flexible head generation, number of turbines and sluice gates). A less common 1D approach can be used to simulate the flow across the width of the TRS.

To understand the large-scale regional flow and surface elavation changes, a 2D (depth-averaged) model is common. Hydrodynamic models such as EFDC, Delft3D, ADCIRC, Thetis and TELEMAC have been widely used in the quantification of tidal range resource and the hydro-environmental impacts assessments of TRS (Neill et al. 2018). In depth-averaged 2D models, multi-scale processes such as tidal, wind-wave, biochemical, sedimentological and morphological processes can be simulated over a broad range of spatial scales; continental shelf (1000s km) to estuary (10s km) scales. To model complex flow structures (in vertical and horizontal space) over a local-scale (e.g. in the turbine wake region) a 3D model is required. To the authors knowledge, a 3D model is yet to be used to simulate a TRS at regional scale, due to the immense computational demands. The computational demands of 2D and 3D models often require the use of high performance computers to perform simulations.

2.4.1 Structure Representation

In depth-averaged 2D models, the dynamic structure which operate within the TRS can be represented in the numerical model in various ways. The operation of a TRS involves three key structures: (i) *turbines* and (ii) *sluice gates* (iii) *embankments*. Turbines and sluice gates are dynamic structures which transition between pre-determined modes of operation, responding to changes in the head across the structure.

In TELEMAC-2D, turbines and sluice gates are commonly parameterised by using a user-modified version of the culvert function; a subroutine which calculates the flow between two adjacent nodes. At pre-

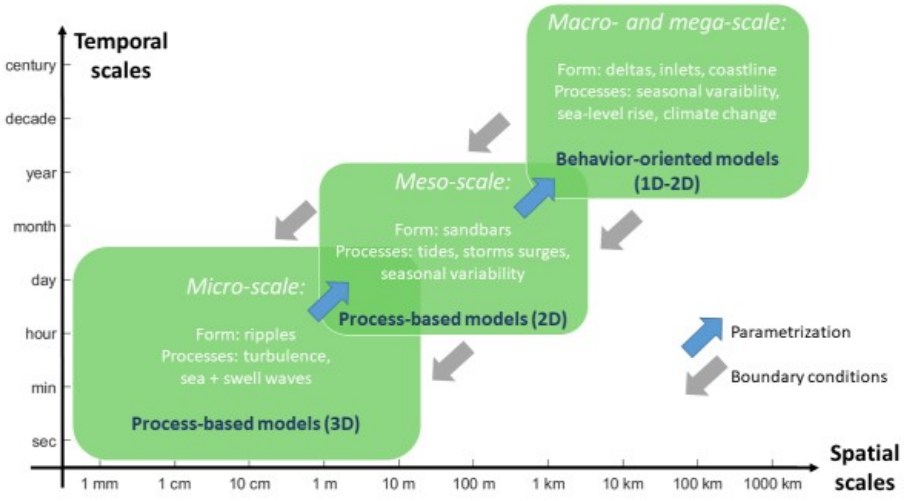

Figure 2.18: The spatio-temporal scales associated with each model type (Yates 2019).

specified points in the tidal cycle, when sufficient water head exists across the structure, water is transferred through the turbine sections. Typically, the flow rate for sluice gates are estimated by using the orifice equation (Equation 1.2). However, to fully comprehend the near-field spatio-temporal flow patterns and improve tidal power prediction technology, there is recent interest in the use of 3D simulations (e.g. Kim & Woo 2023).

The discharge and power output for the turbines are parameterised from digitised performance curves typical of double-regulated bulb turbines (e.g. Angeloudis & Falconer 2017). Due to ignorance of vertical flow structure in the 2D model, the flow behaviour in the near vicinity of turbine is poorly simulated. Jeffcoate (2013) found that it typically took a length of 20 turbine diameters downstream for depth-averaged simulations to give a good approximation of the flow.

Representation of the embankment in hydrodynamic models can be achieved using one of two method: domain decomposition (e.g. Angeloudis, Falconer, Bray & Ahmadian 2016) and bed-level rise (e.g. Carroll et al. 2009). The domain decomposition method splits the model domain into two or more subdomains (described in detail by Angeloudis, Falconer, Bray & Ahmadian 2016), the embankment is represented as

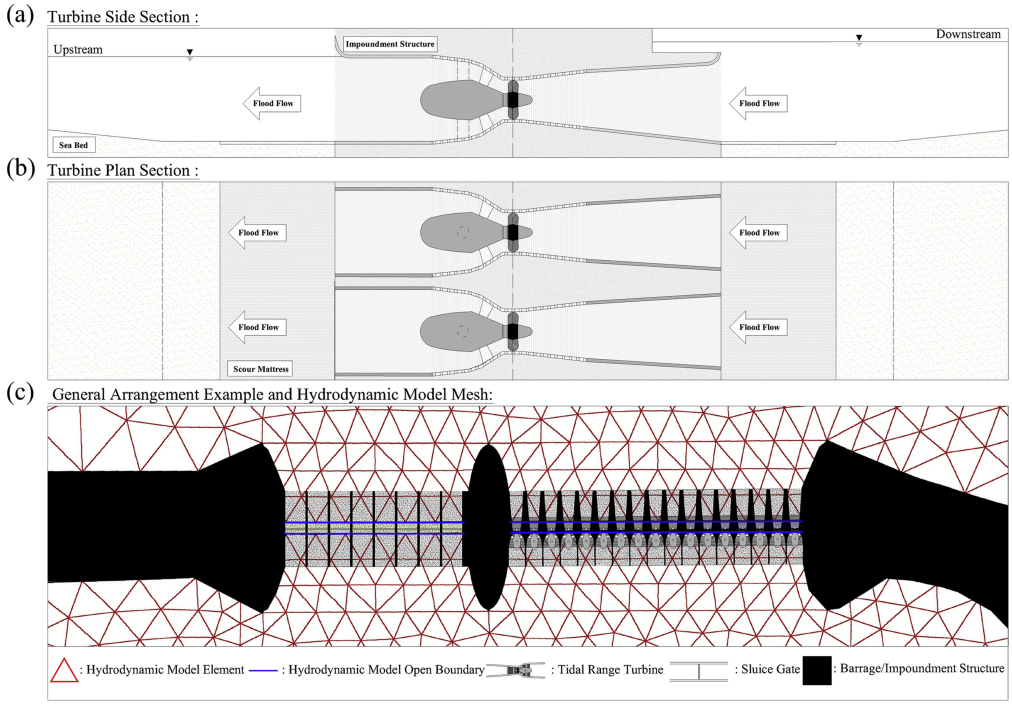

Figure 2.19: Schematic illustration of the general design of turbine caissons for: (a) a cross-section view, (b) a plan view, and (c) turbines representation in a 2D hydrodynamic model (Angeloudis, Falconer, Bray & Ahmadian 2016).

an internal barrier – its treatment within the hydrodynamic model is comparable to other solid boundaries (Fig. 2.19). The bed-level rise method considers the embankment as a bathymetric feature, this method allows the simulation of the slope of the embankment with a fine mesh resolution it is also possible to simulate overtopping. Guo (2022) tested each approach in a idealised lagoon/model domain, concluding that the domain decomposition method maintains accuracy whilst maximising computational efficiency. However, Guo (2022) dismissed the bed-rise method on the premise that additional algorithms must be implemented to protect against parasitic overflows (water trapped on the crest of the embankment), this could however be avoided by ensuring that the embankment height is sufficiently large (although unrealistic). Whilst exploring the far-field effects of TRS, Zhou, Pan & Falconer (2014*b*) extended the open boundary of to the edge of the continental shelf. Subsequent research has shown that the location of the open bound-

aries can have a significant effect on tidal dynamics (e.g. Zhou, Pan & Falconer 2014*a*). Open boundaries must be located sufficiently far from the structure so that the forcing conditions are unaffected by the presence of a TRS, this is known as the 'open boundary problem' and was first described by Garrett & Greenberg (1977). As discussed (Section 2.2.1), tidal waves are reflected at the continental shelf due to the sudden change in water depth (Zhou, Pan & Falconer 2014*a*) and resonant effects arise when the continental shelf width approaches $\frac{1}{4}$ of the tidal wavelength. Open boundary sensitivity analysis has been previously conducted by Zhou, Pan & Falconer (2014*a*) and Mackie et al. (2021) for numerical simulations of tidal barrages and lagoons. In Fig. 2.20, Mackie et al. (2021) shows the how the location of the open boundary effects the predicted impact of multiple tidal lagoons on tidal amplitudes and velocities.

2.4.2 Hydrodynamic Impacts

TRS sites are often characterised by sensitive and complex coastal ecosystems (such as estuaries), disruptions to these ecosystems could cause large changes in the distribution, population or type of benthic and pelagic species (Baker et al. 2020). These impacts are determined by the characteristics of the local marine environment and the TRS design (Mackie et al. 2021), thus applying findings from TRS to another TRS is challenging. Simulations of individual TRS are required to gain any degree of certainty regarding the potential hydro-environmental responses (Pethick et al. 2009). Furthermore, understanding the combined effects and potential interactions of multiple, geographically proximal, tidal lagoons is the key to successfully deploying a fleet tidal lagoons.

Large-scale TRS have been predicted to alter water levels and current velocities within, and in the region of, the impoundment. The operation of a TRS reduces the tidal range within the impoundment, with more significant changes occurring in the case of barrages compared to lagoons (Xia et al. 2010). Using a three-way coupled TELEMAC-2D model (tides, waves and sediment transport), Carroll et al. (2009) predicted the morphological impact of the Mersey Barrage (implemented using the bed-level rise method). In agreement with similar studies, simulations predicted a 60% reduction in tidal range within the impoundment and a regime shift to a net landward sediment transport direction, reducing the water volume of the es-

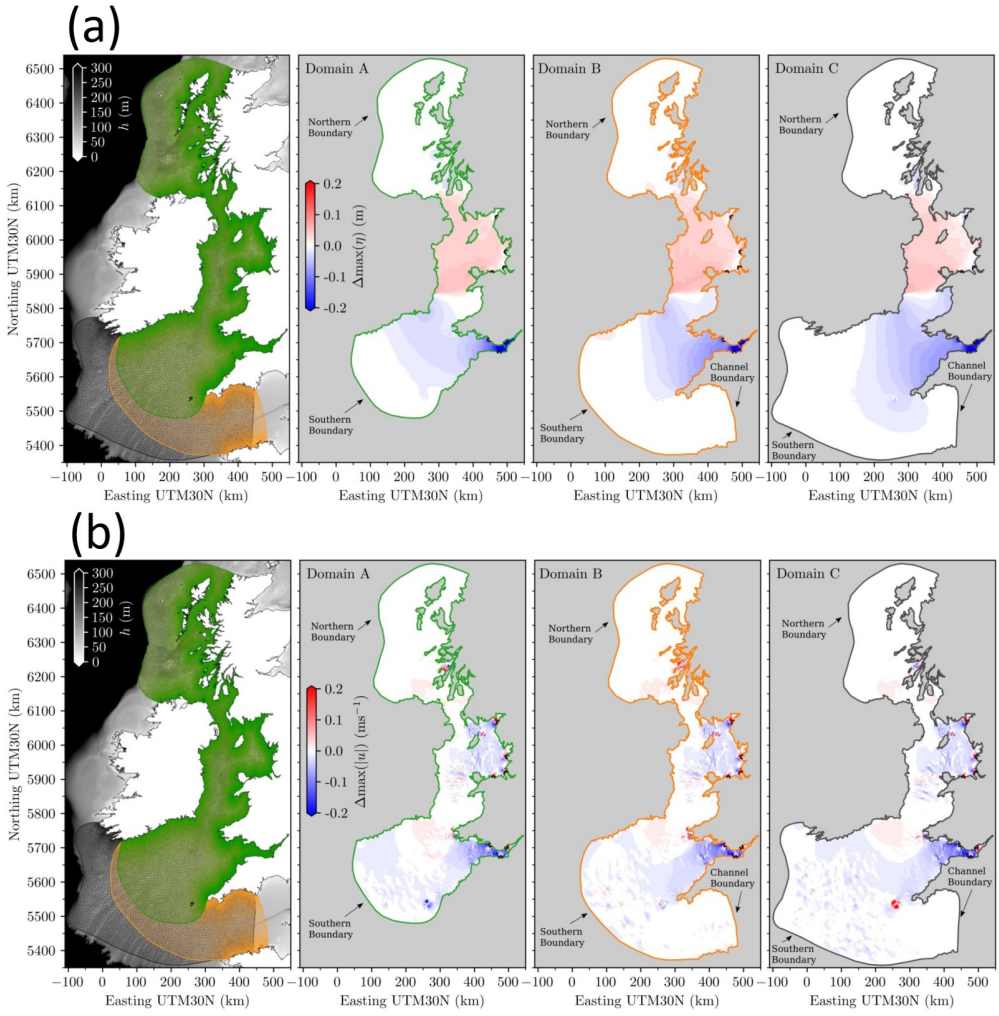

Figure 2.20: The effects of three different open boundary locations on (a) tidal amplitude and (b) tidal velocity (edited from Mackie et al. 2021)

tuary over time. A decreased tidal range within the impoundment can significantly reduce the intertidal area – a key habitat and feeding zone for wading bird species. Guo (2022) predicted that the NWTL would reduce the inter-tidal area by 20 km^2 and in the case of a Severn Barrage, Zhou, Falconer & Lin (2014) predicted that the intertidal area would reduce by 80.5 km^2.

Xia et al. (2010) used Delft3D to simulate the Cardiff-Weston Barrage, Shoots Barrage and the Fleming Lagoon in the Severn Estuary. In the case of a Cardiff-Weston Barrage, at Avonmouth upstream of the barrage site, current velocity was predicted to reduce from 2.5 ms^{-1} (without a barrage) to 1.3 ms^{-1} and the maximum water levels upstream of the barrage were predicted to decrease by 0.3–1.2 m. The Shoots Barrage was predicted to decrease upstream water levels by 0.3-1.0 m, whilst amplifying the maximum water levels downstream of the barrage by typically 20–30 cm. In comparison, the Fleming lagoon was reported to have negligible influence on hydrodynamic processes within the estuary.

The Impacts of Multiple TRS

Mackie et al. (2021) used a consistent lagoon design to understand the response of coastal systems to the co-location of multiple tidal lagoons using the Thetis modelling software. Results suggested that the hydrodynamic impacts of Irish Sea lagoons (North Wales and North-west English coast) were of lower magnitude and more localised, whereas lagoons located in the Severn Estuary had a regional impact owing to the constrained estuarine coastline of the Bristol Channel. In these constrained areas, a tidal lagoon has a larger blockage effect, which reduced the near-resonant state estuarine system and increased cumulative effects with the co-location of additional lagoons. Results suggested a linear cumulative relationship between increasing the number of tidal lagoons and the associated hydro-environmental impacts.

Cornett et al. (2013) conducted a comprehensive study into the hydrodynamic effects of tidal lagoons (coastally attached and offshore) in the Bay of Fundy. In TELEMAC-2D, nineteen hypothetical scenarios which each included one to six lagoons were simulated. In agreement with Mackie et al. (2021), they found significant variation in hydrodynamic impacts between locations. Additionally, it was concluded that the operational mode appears to have little influence on the magnitude of far-field hydrodynamic impacts. A strong lin-

ear relationship is also found between the scale of the lagoon development (in the Minas Basin) and the attenuation in the speed of the depth-averaged currents (in the Minas Passage), with more ambitious developments causing larger attenuation.

Near-turbine Impacts

One major concern associated with the operation of TRS is the entrenchment of scour channels and depositional formations in the vicinity of the turbines. Vortices (or re-circulation zones) can develop either in the near-turbine region or within the impoundment. These zones can lead to fast morphological change due to the stagnation of the water column in centre of the vortices and subsequent deposition of suspended material (e.g. sediments and pollutants). It is important to accurately predict the formation of vortices because they are effective vectors for entrainment and mixing of sand (potentially creating sandbanks), nutrients and pollutants (Vouriot et al. 2019). High influx and subsequent deposition of sediment within the lagoon increases dredging costs. Consequently, dredging is predicted to account for a significant proportion of lagoon maintenance cost, it is therefore crucial to mitigate against deposition within the impoundment (Ahmadian et al. 2010). In addition, sedimentation inside the lagoon can directly reduce the water capacity of the lagoon and in-turn reduce the total electricity generation (Neill et al. 2016).

However, not all studies have predicted the formation of significant sized vorticies within the impounded area (e.g. Ahmadian et al. 2010). Factors such as lagoon length/width ration, inlet width, bathymetry, the model type and parameters all contribute to the formation of these eddies (Vouriot et al. 2019). Falconer et al. (2009) included a momentum conservation aspect to the model which potentially increases the validity of these results. Ahmadian et al. (2010) hypothesised that spacing the turbines apart will mitigate against the formation of vortices, however turbines are often constrained by bathymetry (due to ecological issues with using smaller turbines) therefore the applicability of this solution is lagoon specific.

When water is passing through the turbines and sluices gates local flow velocities can significantly exceed natural levels (Angeloudis, Ahmadian, Falconer & Bockelmann-Evans 2015; Guo 2022), these flows can exert significant bed shear stresses leading to scour and entrenchment of channels in the turbine wake re-

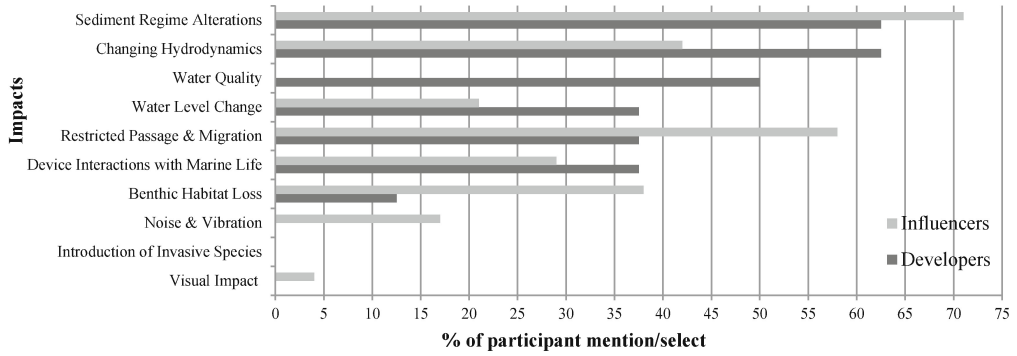

Figure 2.21: High priority environmental impacts – identified from a survey of industry influencers and developers (Elliott et al. 2018).

gion (Guo 2022). Scour around the turbines has the potential to undermine structural integrity. The water head, specification, location and number of turbines and sluice gates will determine the extent to which flow velocities are increased.

2.4.3 Research Gaps

In the past, uncertainty around environmental impacts has hindered the development of the tidal range industry. A lack of social and economic support for tidal barrage and, more recently, tidal lagoon projects can be attributed to a knowledge gap in the potential environmental interactions of TRS. Some environmental impacts are perceived as larger, more significant, barriers to TRS development than others. Elliott et al. (2018) conducted a survey to gain insights into the perspectives of stakeholders in the lagoon-industry. Both groups independently identified sediment regime alterations as the largest barrier to tidal lagoon developments (Fig. 2.21). A subsequent systematic literature review by Elliott et al. (2018), identified sediment regime changes as the area with the least academic research (Fig. 2.22). Given the assumption that the impacts with the least research attention have fewer established solutions, a research gap surrounding lagoon-driven sediment regime/transport changes and potential solutions likely exists (Elliott et al. 2018).

Uncertainty regarding sediment regime could be reduced by improving hydrodynamic modelling tools.

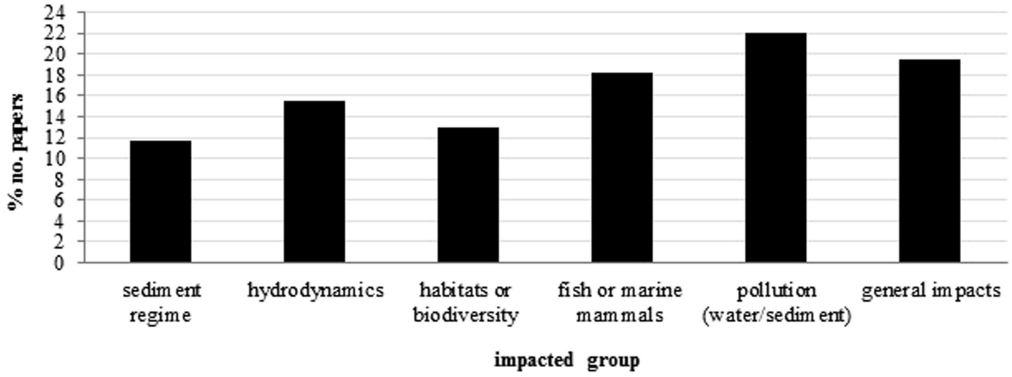

Figure 2.22: The quantity of published tidal lagoon environmental impact research categorised by specific subject area (Elliott et al. 2019).

More specifically, both Guo (2022) and Carroll et al. (2009) highlighted the need for a spatially variable sediment distribution to improve to accuracy and reliability of morphological evolution simulations. To date, such simulations have been parameterised with a spatially heterogeneous grain size distribution, this may lead to dramatically inaccurate estimations of sediment transport rates in the presence of a tidal lagoon (Carroll et al. 2009).

The effect of a tidal lagoon on the Lowest Astronomical Tide (LAT) and Highest Astronomical Tide (HAT) are yet to be explored. The water levels associated with the HAT can significantly increase the global risk of coastal flooding (Haigh et al. 2011), whilst the LAT can have important implications for navigation. Determining the HAT and LAT requires a minimum of a 19 year tidal elevation dataset (Byun & Hart 2019), to fully resolve interannual cycles such as (e.g. the 18.61 year nodal cycle). We hypothesise that significant changes could arise due to the modification of multiple tidal constituents. Furthermore, other long-term processes, which are not captured in the simulation time of 2D hydrodynamic models, such a sea-level rise are yet to be studied in the context of a tidal lagoon (Ahmadian et al. 2010).

2.5 North Wales Tidal Lagoon Site

The North Wales coast is well suited to the development of a tidal lagoon, the site has a combination of advantages: (1) a large tidal range resource (65-80 GWh km^{-2}; Mackie et al. 2021), (2) the regions bathymetry provides ideal conditions for a cost-effective embankment construction (due to the adjacent shallow and deep waters; Fig. 2.16), (3) good grid inter-connectivity will minimise transmission loss (4) the potential to mitigate coastal flood risk along the impounded coastline (although it still remains uncertain as to whether this is beneficial overall, e.g. Lyddon et al. 2015).

Various studies have simulated the hydrodynamic impacts of individual and a combination of tidal lagoons along the North Wales coast. In the literature, academics have used locations for the embankment of the NWTL. A lack of consensus around the optimal location or size of a lagoon can be attributed to the fact that a range of NWTL locations are yet to be simulated and compared using a consistent modelling setup. In Fig. 2.23 the NWTL locations used in previous studies have been complied. The most commonly modelled tidal lagoon is the Conwy lagoon which stretches from Llandudno to Rhyl – proposed by North Wales Tidal Energy (*North Wales Tidal Energy, North Wales Presents A World-Class Site for A Tidal Lagoon* n.d.).

Angeloudis, Ahmadian, Bockelmann-Evans & Falconer (2015) examined the near-field impacts of a ebb-only tidal lagoon which stretched from Old Colwyn to Prestatyn (Fig. 2.23, results indicated that the maximum water levels within the tidal lagoon would decrease by ≈ 0.5 m. A preliminary study by Angeloudis, Ahmadian, Falconer & Bockelmann-Evans (2015) simulated the combined operation of four tidal lagoons (locations shown in Fig. 2.23). Angeloudis, Ahmadian, Falconer & Bockelmann-Evans (2015) highlighted key gaps in tidal lagoon research, including optimisation of design parameters and far-field impacts. Angeloudis, Ahmadian, Falconer & Bockelmann-Evans (2016) expanded on Angeloudis, Ahmadian, Falconer & Bockelmann-Evans (2015), examining the differences between 0D and 2D modelling techniques. 0D modelling tends to overestimate he power generation of individual tidal lagoons by $\approx 5\%$, this increases to $\approx$ 30% when the combined operation of multiple tidal lagoons is simulated. Angeloudis, Ahmadian, Falconer

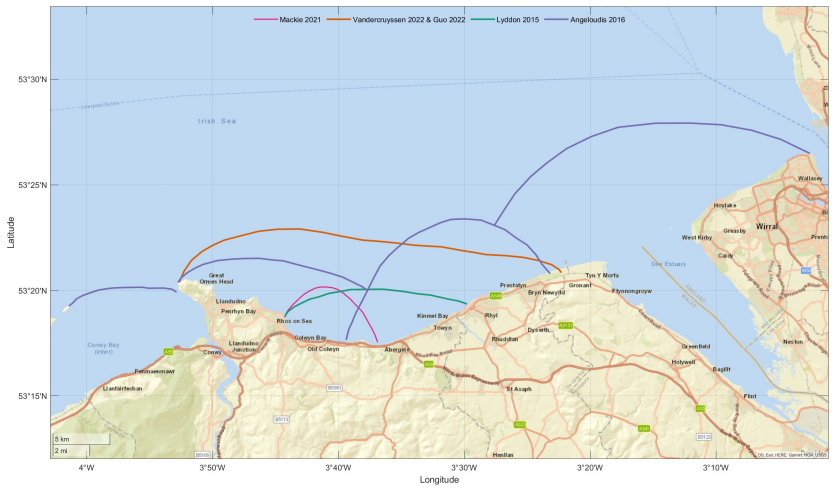

Figure 2.23: Potential North Wales tidal lagoon locations, each lagoon has been used in previous hydrodynamic modelling studies.

& Bockelmann-Evans (2016) attributed this overestimation to the altered tidal flow conditions which are account for in the 2D model, but not considered by the 0D model.

Extensive TELEMAC-2D modelling by Guo (2022) focused on the hydro-environmental impacts various UK-based tidal lagoons, one of which was located on the North Wales coast. Using a continental shelf scale domain, the effect on tidal constituents within the Irish Sea was examined. Amplitude and phase alterations to the N_2 were far-field, whereas the M_2 and S_2 were only affected in the near-field. Findings suggested that a NWTL would slightly reduce the high-water level in Liverpool Bay (-5 to -10 cm) while increasing it in Cardigan Bay (5 to 10 cm). Consequently, up to 20 km^2 of low-level intertidal mudflat would be lost, which could be mitigated by dredging work in the east towards Rhyl. Guo (2022) also noted that velocity fluctuations along the west coast of Anglesey (the maximum turbidity region – which provides a unique pelagic habitat) which could potentially cause negative interactions with future tidal stream turbine developments at the Holyhead Deep site.Guo (2022) and Angeloudis, Falconer, Bray & Ahmadian (2016) both predict a reduction in flow velocities and therefore bed shear stress in the wake of the lagoon, increas-

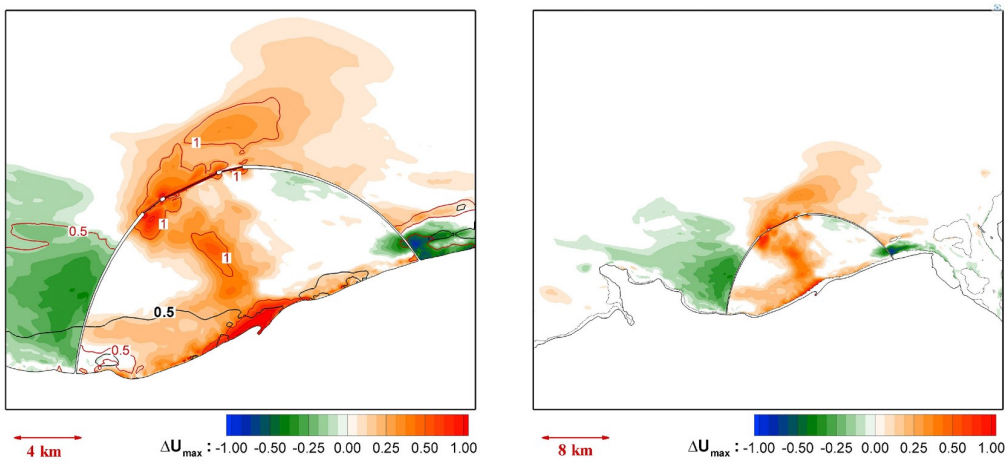

Figure 2.24: Change in average velocity due to the operation of the Clwyd lagoon (Angeloudis, Falconer, Bray & Ahmadian 2016).

ing sediment accumulation in estuaries such as the Dee and Mersey.

2.5.1 Hydrodynamics

The Irish Sea is a semi-enclosed water body located on the North-West European Continental Shelf. Two channels connect the Irish Sea to the Atlantic Ocean; the North Channel and St Georges Channel. In terms of size, the Irish Sea is approximately 300 km in length and 75-200 km in width, the mean water depth is 60 m with maximum depths reaching 275 m (McKay & Pattenden 1993; Olbert et al. 2010). The North Wales coastline boarders the eastern edge of the Irish Sea. The eastern Irish Sea is usually defined as the area to the east of the Isle of Man (approximately -4.5 W), it receives 70% of the total freshwater input from several estuaries (e.g. the Conwy, Dee, Mersey, Solway Firth and Morcambe. With an average water depth of around 30 m and a maximum depth of 55 m, the eastern Irish Sea is the shallow, but large, region of the Irish Sea, it represents 40% of the total area, but only 20% of the total water volume (Olbert et al. 2010).

The hydrodynamics of the Irish Sea are primarily driven by a standing wave tidal system, dominated by the M_2 and S_2 constituents. The tidal wave travels into the Irish Sea from the North and St. George's

Channel, generating tidal current velocities of the order 1.0 - 1.5 ms^{-1} (MacDowell 1997). There is a broad range in the magnitude of tidally-induced current velocities in the Irish Sea. Generally, velocities are increase along the shallower eastern Irish Sea (peak velocities are > 1.1 ms^{-1} in two locations, Wicklow Head and NW Anglesey; Robinson 1979; Horsburgh et al. 2000). In the eastern Irish Sea, the M_2 tide encounters shallow waters, energy is transferred by non-linear processes to higher harmonics generating the M_4 constituent (overtides). The combination of the M_2 and the M_4 creates tidal asymmetry and amplification along the North Wales coast, in particular in estuaries and semi-enclosed nearshore areas (Horrillo-Caraballo et al. 2021). The tidal regime is defined as macro, with a peak spring tidal range of 10 m in Liverpool Bay (Howarth 2005), and the flood-dominant tide exhibits velocities 1.2 times faster than the ebb velocities (Brown et al. 2016). This interaction largely determines the pattern of residual sediment transport pathways around the British Isles (Pingree & Griffiths 1979).

Wave conditions in the Irish Sea are generally moderate and seasonally-driven. The most energetic regions are found southeast Irish Sea (i.e. southwest coast of Britain). The eastern Irish Sea is heavily sheltered from Atlantic Swell, therefore, local wind-generated waves (approaching from the west) dominate the wave climate. Since 2002, the maximum wave height in Liverpool Bay was 5.4 m, with corresponding peak period of 12 s. Overall significant wave height did not exceed than 2 m for 93%, and less than 1 m for 68%, from 2002 to 2010 (Brown et al. 2010).

2.5.2 Human Activities

Over the past decades, the socio-economic importance of the Irish Sea has grown (Coughlan et al. 2021), supporting a variety of economic sectors including: transport, shipping, subsea cables, marine renewable energy, fishing and hydrocarbon extraction. Increased interest in offshore sources of renewable energy has led to expansion of the offshore wind sector, the shallow depths and energy resource of the Irish Sea provides good conditions for siting fixed-bottom renewable energy devices such as wind turbines and tidal stream turbines (Guinan et al. 2021). In 2017, offshore wind farms in the Irish Sea already produce 16% of total European offshore wind energy (DeCastro et al. 2019). There are currently eight offshore wind farm's

in the eastern Irish Sea (with a further four in planning), three tidal stream sites, five aggregate extraction areas as well as numerous oil and gas fields. Two major subsea electricity cables (the CeltixConnect and Greenlink interconnector) span across the bed of Irish Sea, a continuously growing number of minor subsea cables connect renewable energy sites to the mainland.

As discussed in Section 2.2.2, placing fixed structures into the marine environment significant perturbs sediment transport processes and can lead to scour. Numerical simulations have shown that tidal stream turbines cause significant wake and reduction in flow strength which may enhance bed shear stress and weaken residual sediment transport pathways (Li et al. 2017). Simulations of wind turbine monopiles have shown they cause perturbations to vertical mixing – these disturbances propagate over 1 km, reducing residual velocities by 5% (Cazenave et al. 2016).

2.6 The TELEMAC-MASCARET System

The open TELEMAC-MASCARET system (or TELEMAC) is a computational fluid dynamics tool comprised of several fine element computer programs (shown in Table 2.6). The TELEMAC system was developed by the National Hydraulics and Environment Laboratory of the Research and Development Directorate of the French Electricity Board, in collaboration with other research institutes. In 2010, after the creation of the TELEMAC-MASCARET Consortium, TELEMAC was changed to open-source format. Particular functions can be programmed into TELEMAC through the modification of individual subroutines (which are written in well-documented Fortran-90 code). Because the code is open-source, user-specific requirements can be satisfied, expanding the applicability of the TELEMAC software.

Input Files and Data

Each module requires a set of initial files to successfully complete a simulation, these files include the:

- *Steering file*: Analogous to a list of options, the steering file allows the user to define the input files, selected output variables and physical parameters.

Table 2.6: The modules included within the TELEMAC modelling suite.

Hydrodynamics
ARTEMIS: Wave agitation in harbours
MASCARET: One-dimensional flows
TELEMAC-2D: Two-dimensional flows – Saint-Venant equations
TELEMAC-3D: Three-dimensional flows – Navier-Stokes equations
TOMAWAC: Wave propagation in the coastal zone
Transport/Dispersion
GAIA: 2D sediment transport (latest release)
SISYPHE: 2D sediment transport
SEDI-3D: 3D suspended sediment transport
NESTOR: Simulation of dredging operations

- *Geometry file*: This file gives the geo-spatial information regarding the finite element mesh and bottom topography data.
- *Boundary conditions file*: The state of each boundary node is defined in this file, open boundaries are highlighted and the expected inputs are listed.
- *Fortran user file*: All user-modified subroutines are defined in this file.

2.6.1 TELEMAC-2D

TELEMAC-2D[3] is a powerful hydrodynamic modelling tool with a wide range of use cases that involve the simulation of rivers, estuaries and seas. TELEMAC-2D-simulates depth averaged flow velocities and free surface height on an unstructured grid. The TELEMAC-2D code solves the depth-averaged free surface flow equations first derived by Barré de Saint–Venant (known as the Saint-Venant equations; Barre 1871). The Saint-Venant equations result from the 2D simplification (integration over depth) of the Navier-Stokes

[3] `http://www.opentelemac.org/index.php/manuals/summary/13-telemac-2d/1058-telemac-2d-user-manual-en-v7p0`

fluid dynamics equations. The Saint-Venant equations implicitly assume hydrostatic pressure distribution, constant fluid density and depth-averaged velocity components (Vreugdenhil 1994; Lane 1998). Such an approach is valid when the horizontal-scale of the flow is significantly larger than the vertical-scale and baroclinic effects are negligible. The Saint-Venant equations are comprised of the continuity equation:

$$\frac{\partial h}{\partial t} + \mathbf{u} \cdot \nabla(h) + h \,\mathrm{div}(\mathbf{u}) = S_h \tag{2.6}$$

The momentum equations in the non-conservative form are as follows, momentum along x:

$$\frac{\partial u}{\partial t} + \mathbf{u} \cdot \nabla(u) = -g\frac{\partial Z}{\partial x} + S_x + \frac{1}{h}\,\mathrm{div}(h\nu_t \nabla u) \tag{2.7}$$

Momentum along y:

$$\frac{\partial v}{\partial t} + \mathbf{u} \cdot \nabla(v) = -g\frac{\partial Z}{\partial y} + S_y + \frac{1}{h}\,\mathrm{div}(h\nu_t \nabla v) \tag{2.8}$$

Tracer conservation:

$$\frac{\partial T}{\partial t} + \overrightarrow{u} \cdot \overrightarrow{\nabla} T = +S_T + \frac{1}{h} div(h\nu_T \overrightarrow{\nabla} T) \tag{2.9}$$

where h (m) is depth of water, u, v (ms^{-1}) are velocity components, T (gl^{-1} or ^oC) is passive (non-buoyant) tracer, g (ms^{-2}) is acceleration due to gravity, ν_t, ν_T ($\mathrm{m}^2\mathrm{s}^{-1}$) are momentum and tracer diffusion coefficients, Z (m) is free surface elevation, t (s) is time, x, y (m) are horizontal space coordinates, S_h (ms^{-1}) is a source or sink of fluid, S_x, S_y (ms^{-2}) are source or sink terms in dynamic equations, S_T ($\mathrm{gl}^{-1}\mathrm{s}^{-1}$) is the source or sink of tracer, h, u, v and T are the unknowns.

Small scale bedforms contribute to the overall bed roughness (as previously discussed in Section 2.2.2), however the models spatial resolution is insufficient to resolve these features. Therefore they must be parameterised into TELEMAC-2D. The user can select from various parameterisation methods, based on the approach used in previous modelling studies (Guo 2022), we test the sensitivity of our model to various coefficient values for Manning's law and Nikuradse's law.

2.6.2 Numerical Methods

In numerical modelling, discretisation is required to solve continuous functions (e.g. the Saint-Venant equations) at specific points in space and time. A selection from one of two numerical discretisation methods

can be made in TELEMAC-2D: *Finite Element Method* or *Finite Volume Method*.

The FEM approximates the unknown function over the entire domain. An approximate solution is achieved by first dividing the domain (in space) into a finite number of elements, and then assigning a set of simplified equations to each element. The individual sets are then systematically recombined into a global system of equations, that is solved using developed solution techniques and initial conditions (Logan 2002).

The flexible sub-division of the domain has several advantages. Firstly, due to its unstructured character, it can more accurately represent complex geometries (e.g. coastlines). A second advantage is the ability to increase the density of the elements in regions of interest, allowing for high resolution simulations whilst minimising computational requirements.

2.6.3 Rationale behind using TELEMAC-2D

The TELEMAC modelling suite was selected for this study for three reasons. Firstly, the use of the FEM facilitates the use of a unstructured grid which allows for a more accurate representation of complex coastal morphology. TELEMAC is efficient on high performance computers. Last of all, TELEMAC is written in Fortran 90, the code is open-source format which enables flexibility, experimentation and customisation of individual subroutines.

In this study, TELEMAC-2D was used to simulate the hydrodynamics in the model domain. The primary focus of the study is on the far-field hydrodynamic impacts of a TRS, rather than changes to the near-structure vertical profile. In our study area, vertical stratification is considered to have negligible influence on tidal dynamics and the horizontal scale of our study region is significantly larger than the vertical scale, therefore TELEMAC-2D (depth-averaged) hydrodynamic model was deemed suitable for this application.

2.7 Hydrodynamic Model Development

2.7.1 Model Geometry

Mesh generation was conducted using BlueKenue (Centre 2010). BlueKenue uses the Delaunay triangulation method to generate a mesh of non-uniform and non-overlapping triangles. Triangular unstructured mesh's have a flexible character and can seamlessly increase or decrease in density in the desired regions. Initially, two model domains were generated: the *Irish Sea Model* (ISM) and the *Continental Shelf Model* (CSM).

The extent of the ISM domain is defined by the co-ordinates 51N to 56N and 2.5W to 7W (Fig. 2.25). The ISM model domain used the Universal Transverse Mercator (UTM) Zone 30N coordinate system. After inital testing the ISM domain was unstable when simulating the operation of the TRS (in accordance with findings by Zhou, Pan & Falconer 2014*a*), the CSM was therefore used for all final simulations.

The CSM domain is delineated by the continental shelf break (where the water depths exceeds 300 m; Fig. 2.26). Work by Zhou, Pan & Falconer (2014*a*) and Mackie et al. (2021) informed the open boundary location used here. Because the domain spans multiple UTM Zones (29N, 30N), we use the Latitude/Longitude WGS84 ellipsoid system. The CSM model uses spherical coordinates to adjust the Coriolis effect in accordance with latitude.

In both models, NOAA's full resolution GSHHG coastline data [4] (Wessel & Smith 1996) was used to delineate the closed (coastline) boundary in the model domain. However, along the North Wales coastline, we use the Ordnance Survey coastline high water level outline for a higher resolution geometric representation. The mesh density in the North Wales region is a maximum of 30 m, whereas along other coastlines the resolution ranges from 250-1000 m, and in the offshore region the density is at a minimum of 3000 m. The mesh density was increased (to 500 m) at the landward edge of the open boundaries and reduced (to 6000 m), this allowed for TELEMAC-2D to resolve the tidal forcing at increase resolution in these complex coastal areas whilst reducing the number of open boundary nodes in deep, offshore areas. The complete

[4] `https://www.ngdc.noaa.gov/mgg/shorelines/data/gshhs/`

Table 2.7: Geometric properties of each CSM mesh for the different tidal lagoon scenarios.

Properties	S0	S1	S2	S3	S4	S5	S6
Number of nodes	319,646	343,680	340,878	338,193	334,197	332,126	326,628
Number of elements	608,032	653,885	648,498	643,466	635,675	631,799	621,219

configuration of mesh density regions are shown in Fig. 2.27

Isolated nodes are problematic in numerical simulations, they can be defined as nodes which are connected to one or zero neighbouring nodes. Isolated nodes occur when a coarse resolution mesh is generated over a high resolution coastline. Large islands outside of the North Wales coastal region were removed, the coastline was re-sampled to match the mesh resolution – this process removed isolated nodes.

2.7.2 Open Boundaries and Initial Conditions

There are two open boundaries in the CSM, the southern boundary (Celtic Sea) and the northern boundary (North Atlantic). Each open boundary is identified in the boundary conditions file (.clim), this informs the open boundary nodes with the required tidal input data (u, v, h). We force the tides in our model with the TPXO9.v5a database which is derived from Oregon State University Tidal Inversion Software (OTIS; (Egbert & Erofeeva 2002). TPXO9.v5a generally has a RMSE in the open ocean of <5 cm, the model is assimilated using data from TOPEX/Poseidon (Jason 1 and Jason 2) programmes.

Using Equation 2.2, 22 tidal constituents (M_2, S_2, N_2, K_2, K_1, O_1, P_1, Q_1, MM, MF, M_4, MN_4, MS_4, $2N_2$, S_1, $2Q_1$, J_1, L_2, M_3, MU_2, NU_2 and OO_1) were converted into u, v, h and input at the two open boundaries. Freshwater inputs (e.g. rivers and precipitation) were not included since they are unlikely to affect meso-scale tidal dynamics. Meteorological forcing (wind and waves) are neglected in our model, Fairley et al. (2014) demonstrated that TRS have a small effect on the ambient wave climate. Permanent marine structures (wind turbine monopiles, pier structures and hydrocarbon extraction rigs) were considered to have negligible effect on meso-scale tidal dynamics, therefore these structures were not represented in

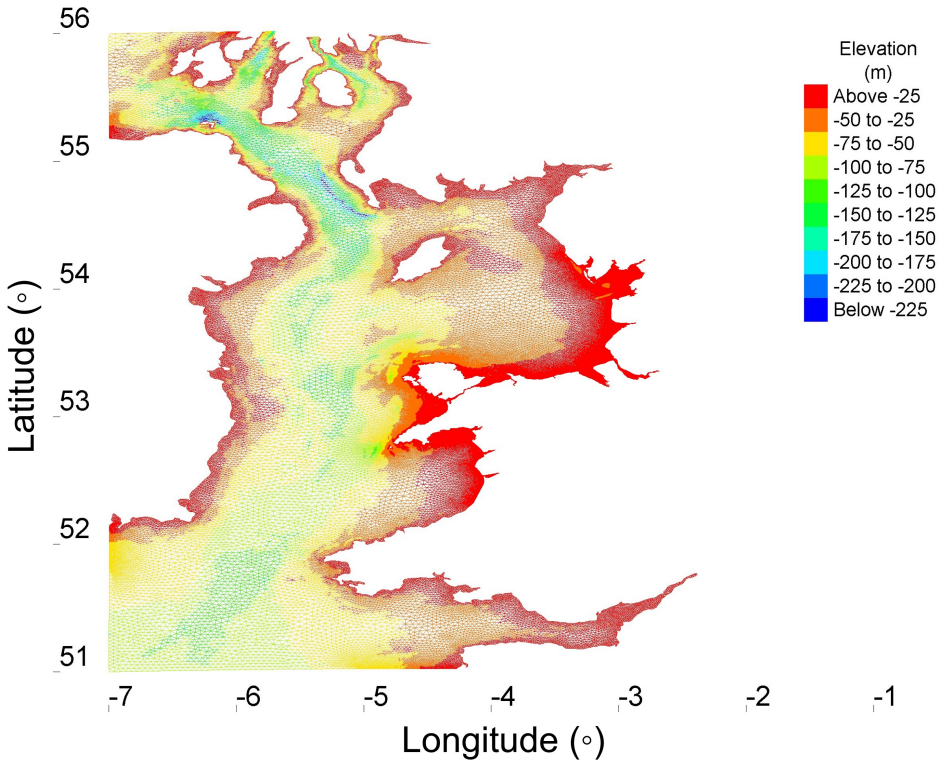

Figure 2.25: The ISM domain, mesh configuration and bed elevation (relative to MSL).

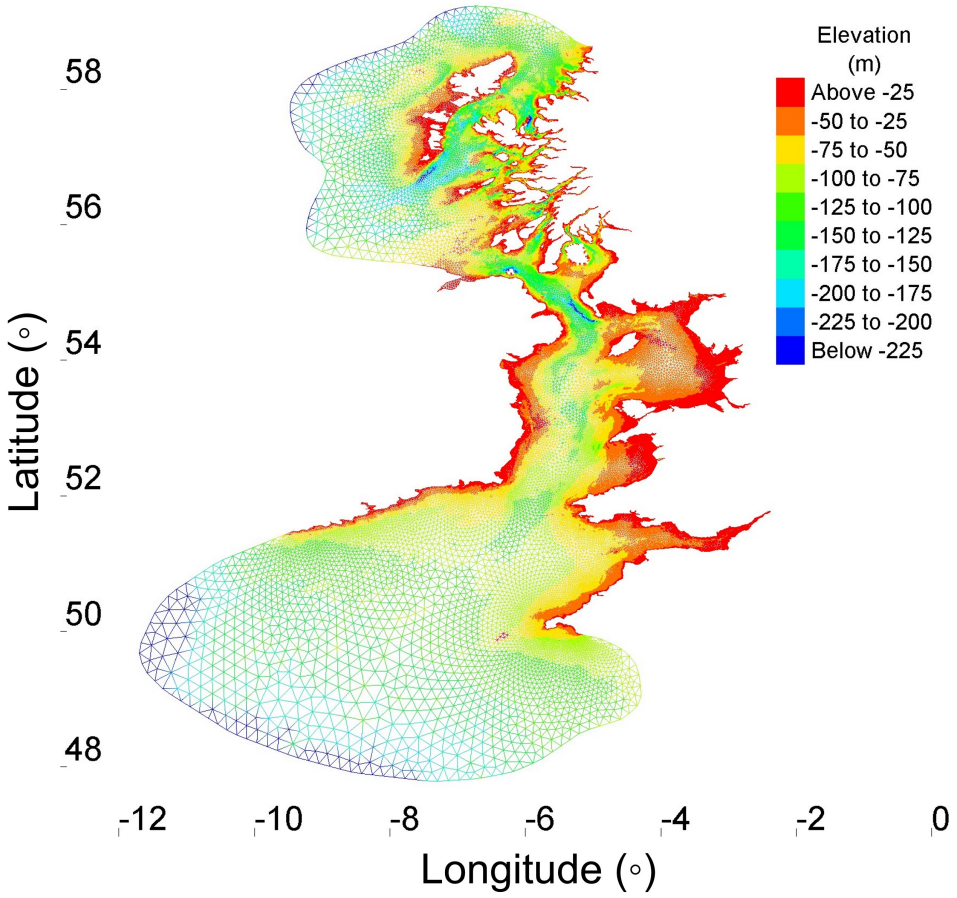

Figure 2.26: The CSM domain, mesh configuration and bed elevation (relative to MSL).

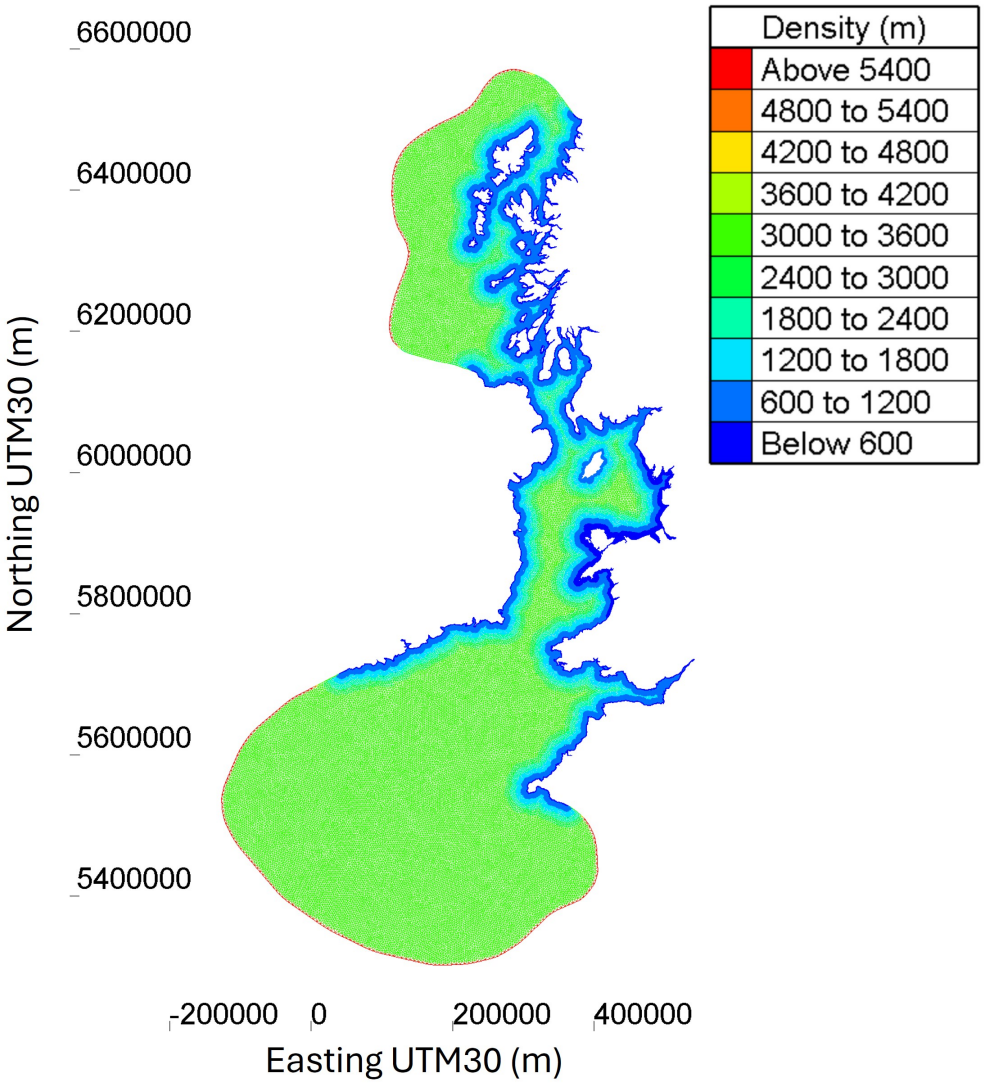

Figure 2.27: The CSM domain and mesh density.

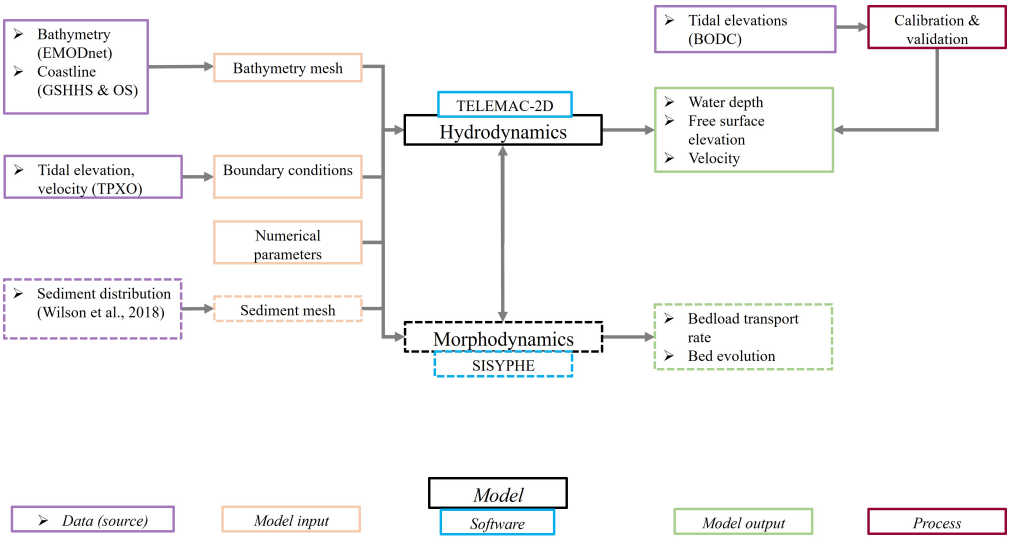

Figure 2.28: A schematic of the TELEMAC modelling setup. The dashed boxes show an additional configuration whereby the model could be coupled with the morphodynamic/sediment transport module SISYPHE.

the mesh.

2.7.3 Modelling Framework

The TELEMAC model (version v8p2r0) was run in parallel on Supercomputing Wales[5] using the modelling approach depicted in Fig. 2.28. The TELEMAC system module TELEMAC-2D (hydrodynamics) was used in this study. The simulation period was 30-days from (2018/04/01 00:00:00). When the simulation is initialised, the water level is constant across the domain. To obtain stable results, the model is given 3 days to 'spin-up' (from 2018/03/28 to 2018/03/31) prior to extracting any outputs.

2.7.4 Calibration and Validation

To calibrate and then validate the ambient model at discrete points, harmonic analysis was performed using the Matlab package T_tide (Pawlowicz et al. 2002). A timeseries of free surface elevation measurements

[5] `https://www.supercomputing.wales/`

were accessed from nine tidal gauge sites (operated by the British Oceanographic Data Centre; BODC 2017). At half-hourly intervals, the observed and modelled elevation of the free surface were compared, the modelled elevations were extracted from the most proximal (non-boundary) node to the tide gauge. The one month validation period ranged from 1/04/2018 00:00:00 to 30/04/2018 00:00:00. This period was selected for two reasons: (1) it coincided with the available ADCP data and, (2) it is of sufficient length to perform harmonic analysis.

It is important to note that the level of agreement between the observed and modelled water level is sensitive to other factors, which are not considered in the model. First of all, waves and meteorological conditions (e.g. air pressure) will have some effect on the water level measured at the tidal gauge, since these effects are not considered, we expect some deviation due to this. In addition, the locations used to extract the predicted tidal heights do not exactly match the actual gauge locations, this is due to the model grid resolution, which can poorly resolve bathymetry at the precise tide gauge locations. To separate the free surface elevation from the tidal signal, we compare the principle harmonic constituents M_2 and S_2.

2.8 Appendix

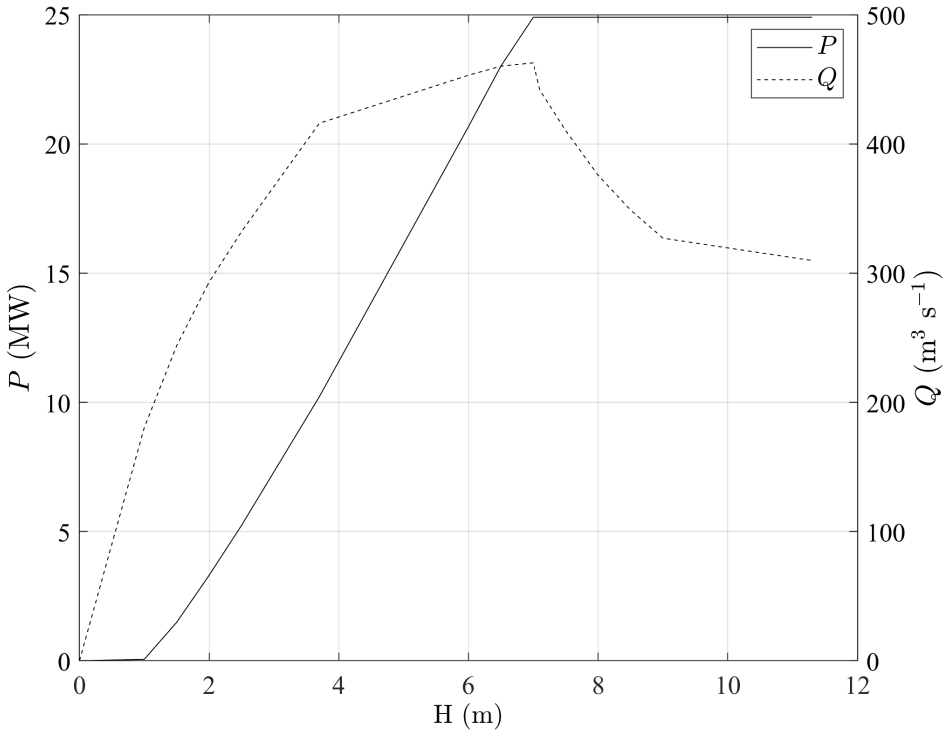

Figure 2.29: Hill chart parameterisation for a Anitz Hydro double regulated bulb turbine scaled to a diameter of 7.2 m with a 25 MW maximum output.

Table 2.8: Calibration results for different values of the Nikrudase coefficient. The lowest SI scores are highlighted in bold.

	SI				RMSE			
Coefficient	$\bar{\alpha}_{M2}$	$\bar{\phi}_{M2}$	$\bar{\alpha}S_2$	$\bar{\phi}S_2$	$\bar{\alpha}_{M2}$ (m)	$\bar{\phi}_{M2}$ (°)	$\bar{\alpha}_{S2}$ (m)	$\bar{\phi}_{S2}$ (°)
0.010	10.99	1.92	12.2	1.93	0.25	2.98	0.11	4.74
0.015	10.25	**1.9**	11.2	1.85	0.24	2.94	0.1	4.55
0.020	9.71	1.92	10.51	1.83	0.22	2.97	0.09	4.48
0.025	9.27	1.95	9.99	**1.82**	0.21	3.03	0.09	4.48
0.030	8.92	2	9.59	1.84	0.21	3.1	0.08	4.51
0.035	8.62	2.05	9.27	1.86	0.2	3.18	0.08	4.56
0.040	8.36	2.1	9.01	1.89	0.19	3.26	0.08	4.63
0.045	8.13	2.15	8.8	1.92	0.19	3.34	0.08	4.7
0.050	**7.93**	2.21	**8.64**	1.95	0.18	3.42	0.07	4.78

Table 2.9: Calibration results for different values of the Manning coefficient. The lowest SI scores are highlighted in bold. The coefficient value selected for model validation is underlined.

	SI				RMSE			
Coefficient	$\bar{\alpha}_{M2}$	$\bar{\phi}_{M2}$	$\bar{\alpha}_{S2}$	$\bar{\phi}_{S2}$	$\bar{\alpha}_{M2}$ (m)	$\bar{\phi}_{M2}$ (°)	$\bar{\alpha}_{S2}$ (m)	$\bar{\phi}_{S2}$ (°)
0.010	19.48	4.72	25.49	63.95	0.45	7.33	0.22	156.96
0.015	16.56	3.45	20.64	45.83	0.38	5.36	0.18	112.49
0.020	12.69	2.36	14.77	2.45	0.29	3.67	0.13	6.01
0.025	8.84	**2.3**	9.94	**2.06**	0.2	3.57	0.09	5.06
0.030	**6.82**	3.3	**9.27**	2.75	0.16	5.12	0.08	6.75
0.035	8.59	4.64	13.28	3.9	0.2	7.2	0.11	9.57
0.040	12.66	6.03	18.94	5.15	0.29	9.35	0.16	12.65
0.045	15.32	7.53	25.20	6.31	0.37	12.10	0.21	16.92
0.050	22.09	8.71	30.38	7.74	0.51	13.52	0.26	18.99

Table 2.10: Validation results at each of the 10 stations.

Station information					Validation results		
Number	Name	Latitude (N)	Longitude (W)	Datum (m)	R^2	RMSE (m)	Bias (m)
1	Llandudno	53° 19' 54.0"	03° 49' 30.8"	-3.85	0.994	0.325	-0.255
2	ADCP	53° 22' 32.6"	3° 43' 35.1"	N/A	0.995	0.188	0.002
3	Holyhead	53° 18' 50.2"	04° 37' 13.6"	-3.05	0.985	0.376	-0.311
4	Liverpool	53° 26' 58.9"	03° 01' 04.8"	-4.93	0.950	0.603	-0.231
5	Barmouth	52° 43' 08.6"	52° 43' 08.6"	-2.44	0.971	0.421	-0.324
6	Heysham	54° 01' 53.9"	02° 55' 13.5"	-4.90	0.964	0.583	-0.315
7	Port Erin	54° 05' 07.4"	04° 46' 05.0"	-2.81	0.984	0.232	-0.124
8	Fishguard	52° 00' 49.5"	04° 58' 59.4"	-2.44	0.983	0.439	-0.398
9	Bangor	54° 39' 53.1"	05° 40' 10.1"	-2.01	0.962	0.203	-0.092
10	Ilfracombe	51° 12' 39.5"	04° 06' 39.4"	-4.80	0.992	0.337	-0.252

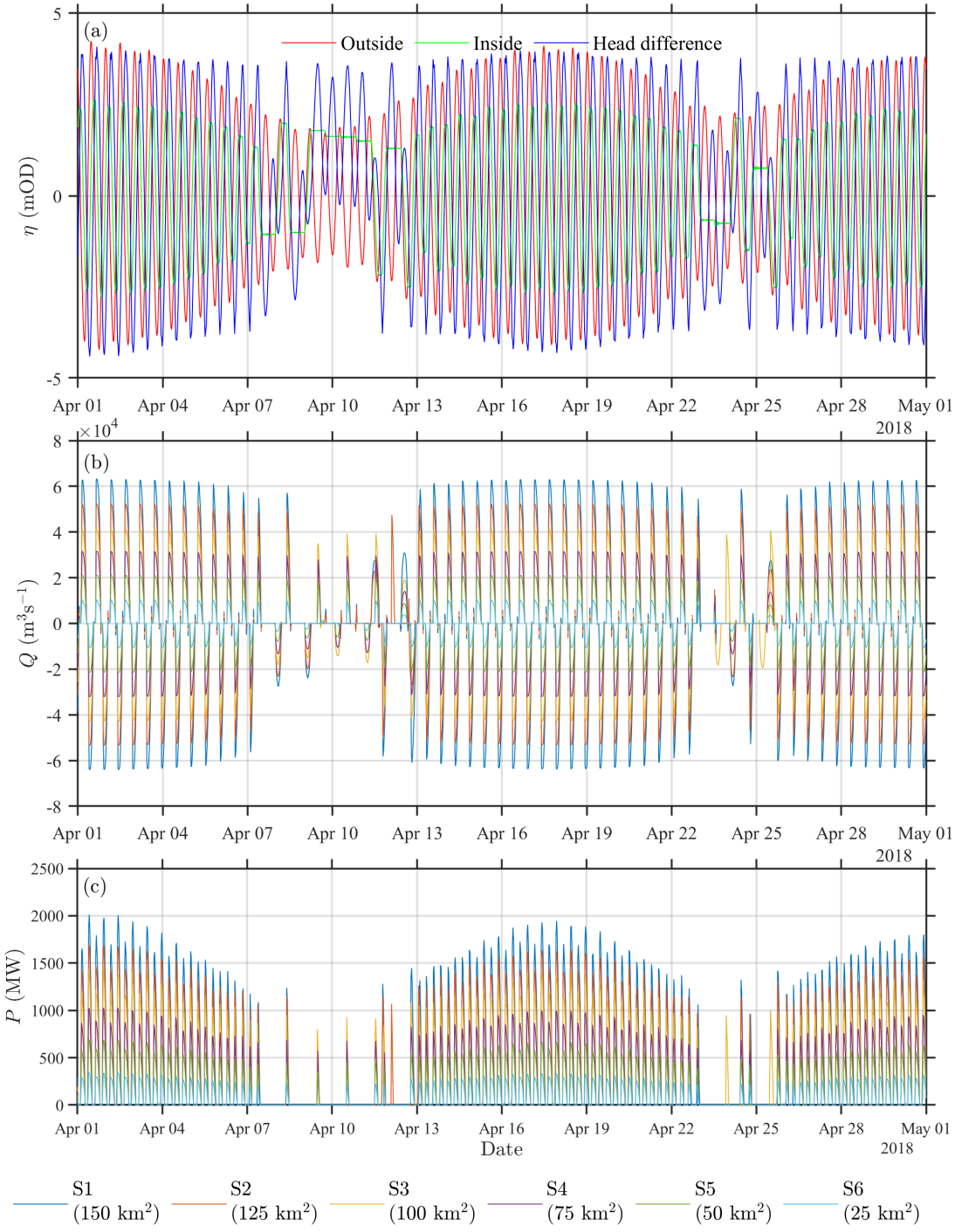

Figure 2.30: (a) Free surface elevation η within and outside the impoundment, the head difference across the structure. (b) Turbine discharge (Q) and (c) power output P for each tidal lagoon scenario. Note, the results span the full period of lagoon operation (which begins at hour 72 (01-04-2018), once the 3-day spin up period has ceased)

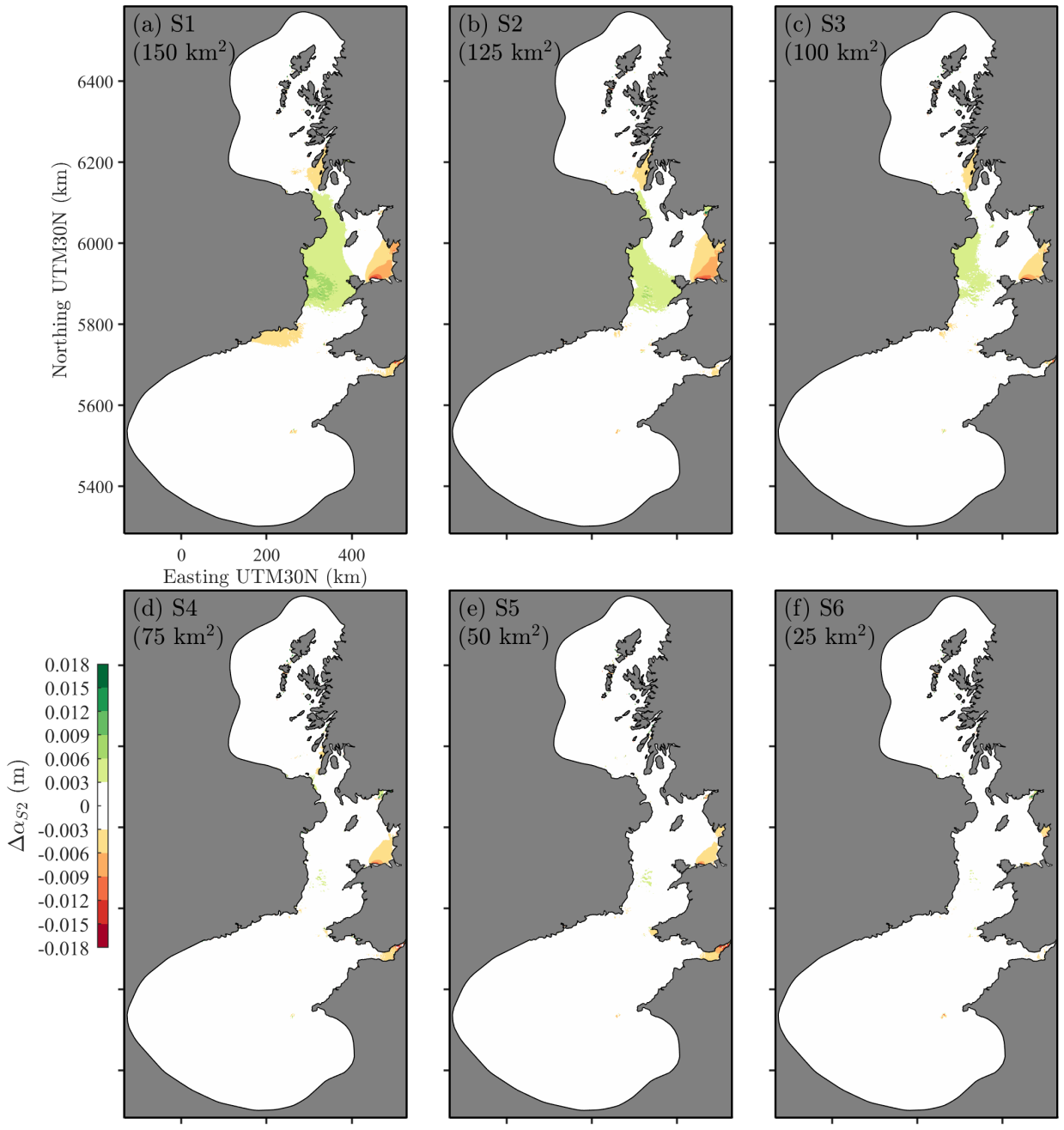

Figure 2.31: The predicted change in the amplitude of the S_2 constituent $\Delta\alpha_{S2}$ (m). Under each scenario (a) S1, (b) S2, (c) S3, (d) S4, (e) S5 and (f) S6, the results are interpolated to a 1×1 km grid for visualisation.

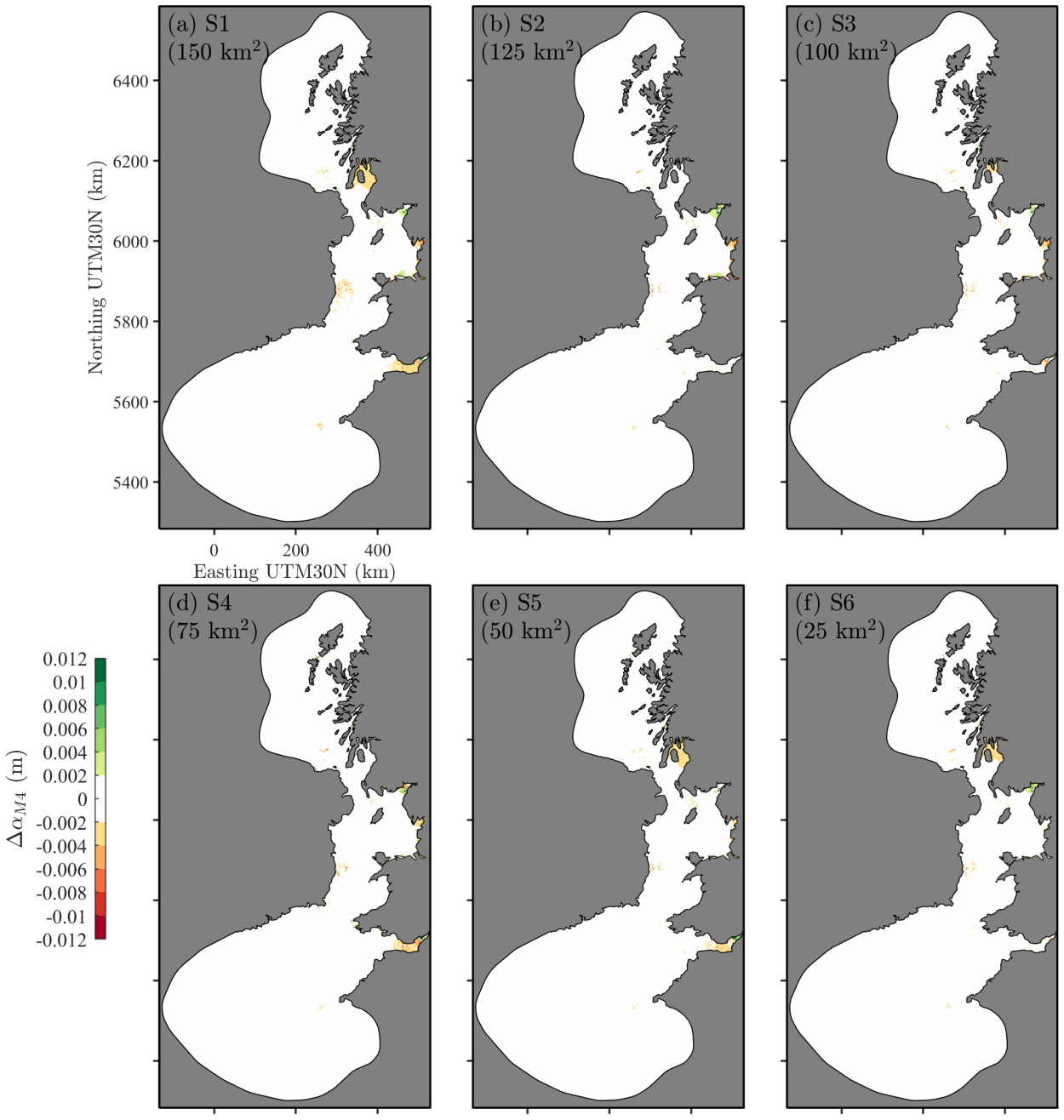

Figure 2.32: The predicted change in the amplitude of the M_4 constituent $\Delta\alpha_{M4}$ (m). Under each scenario (a) S1, (b) S2, (c) S3, (d) S4, (e) S5 and (f) S6, the results are interpolated to a 1×1 km grid for visualisation.

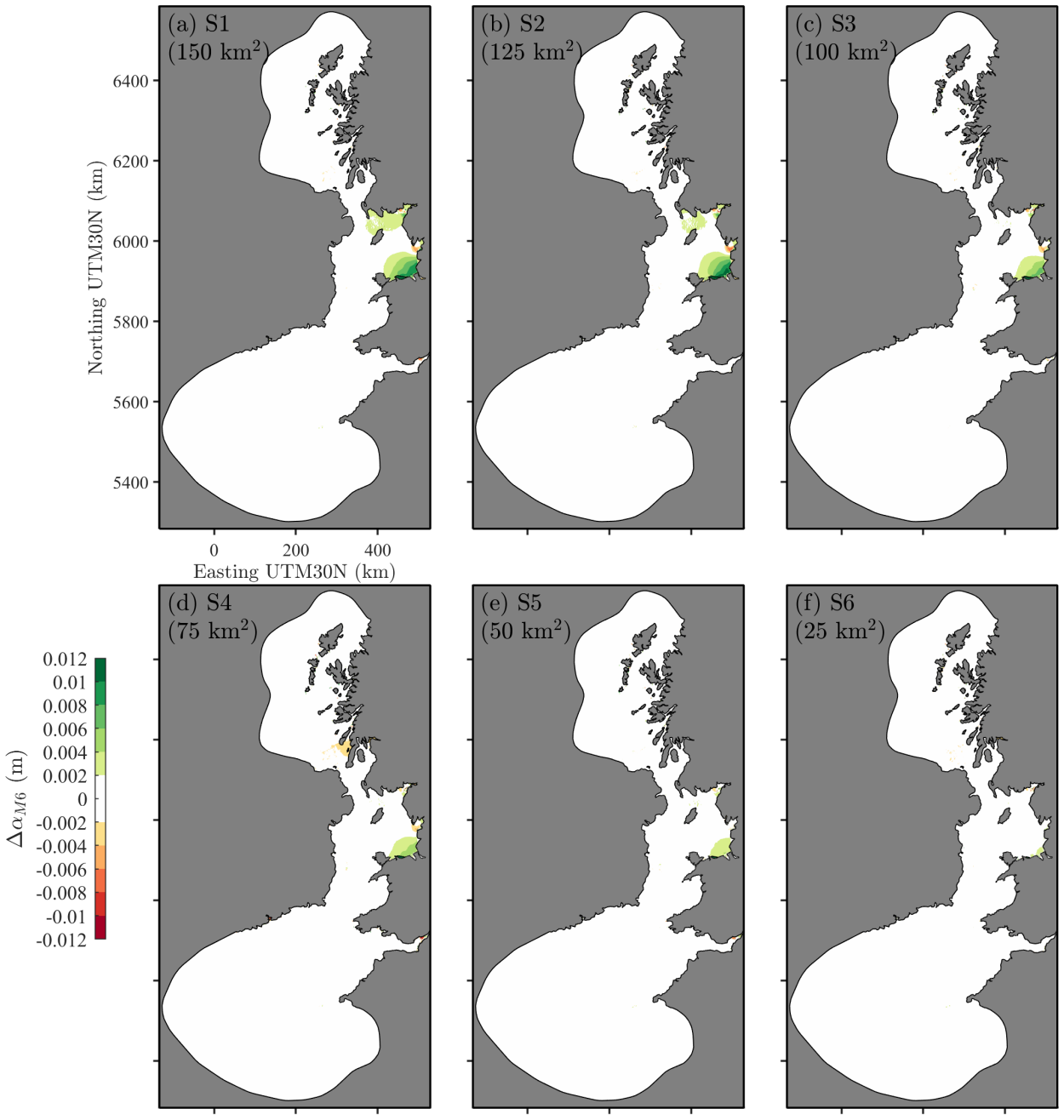

Figure 2.33: The predicted change in the amplitude of the M_6 constituent $\Delta\alpha_{M6}$ (m). Under each scenario (a) S1, (b) S2, (c) S3, (d) S4, (e) S5 and (f) S6, the results are interpolated to a 1×1 km grid for visualisation.

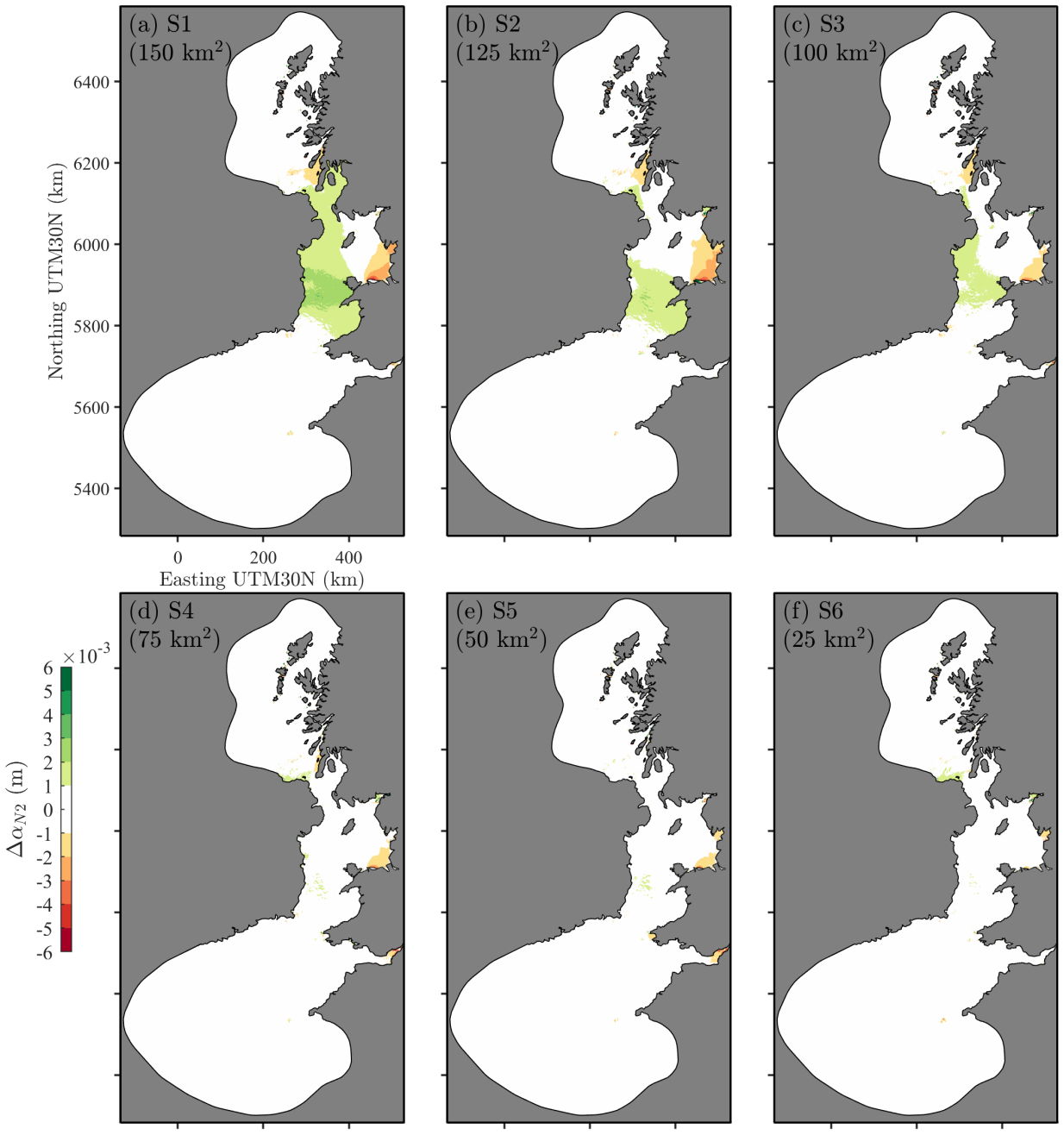

Figure 2.34: The predicted change in the amplitude of the N_2 constituent $\Delta\alpha_{N2}$ (m). Under each scenario (a) S1, (b) S2, (c) S3, (d) S4, (e) S5 and (f) S6, the results are interpolated to a 1×1 km grid for visualisation.

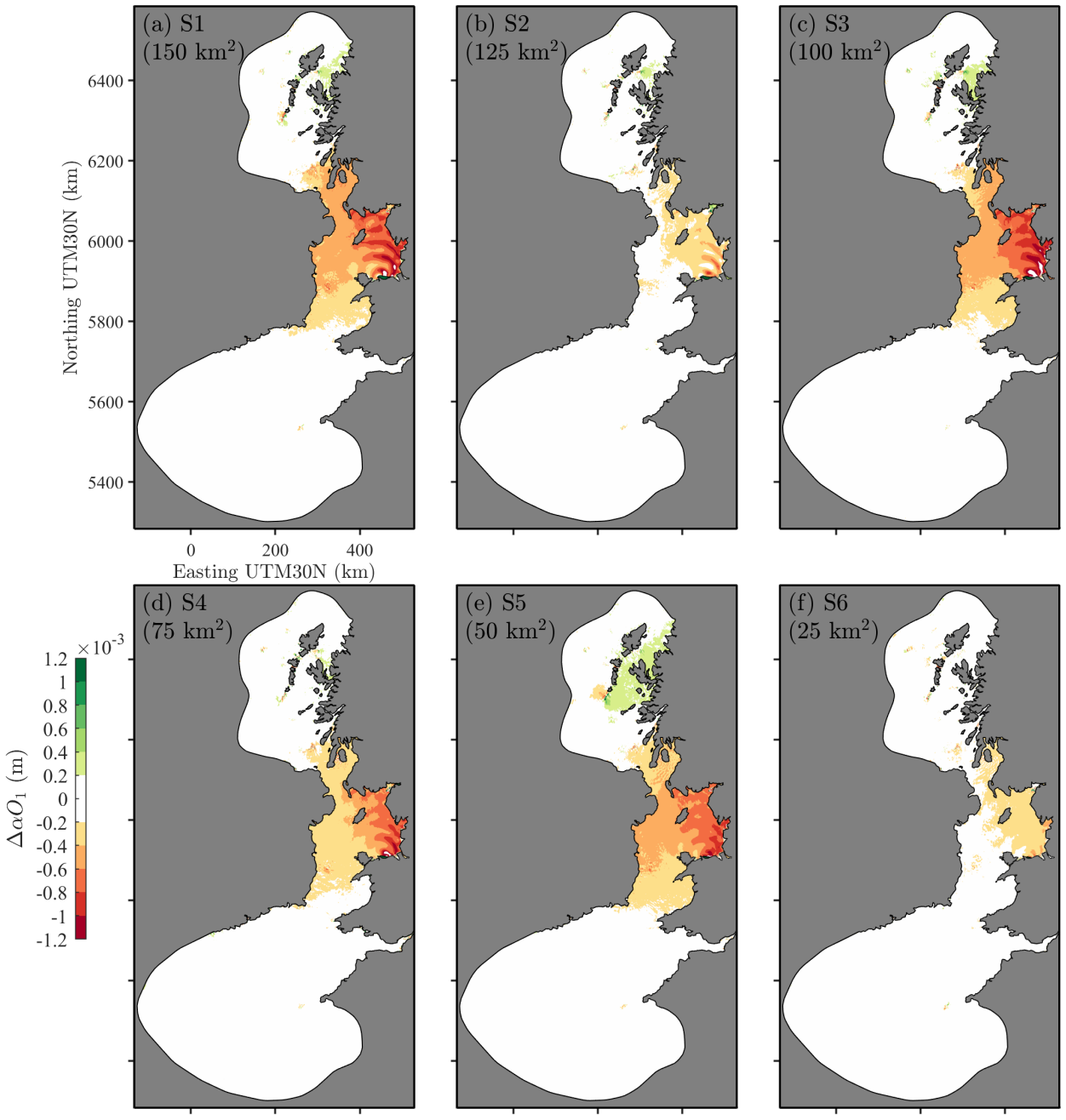

Figure 2.35: The predicted change in the amplitude of the O_1 constituent $\Delta\alpha_{O1}$ (m). Under each scenario (a) S1, (b) S2, (c) S3, (d) S4, (e) S5 and (f) S6, the results are interpolated to a 1×1 km grid for visualisation.

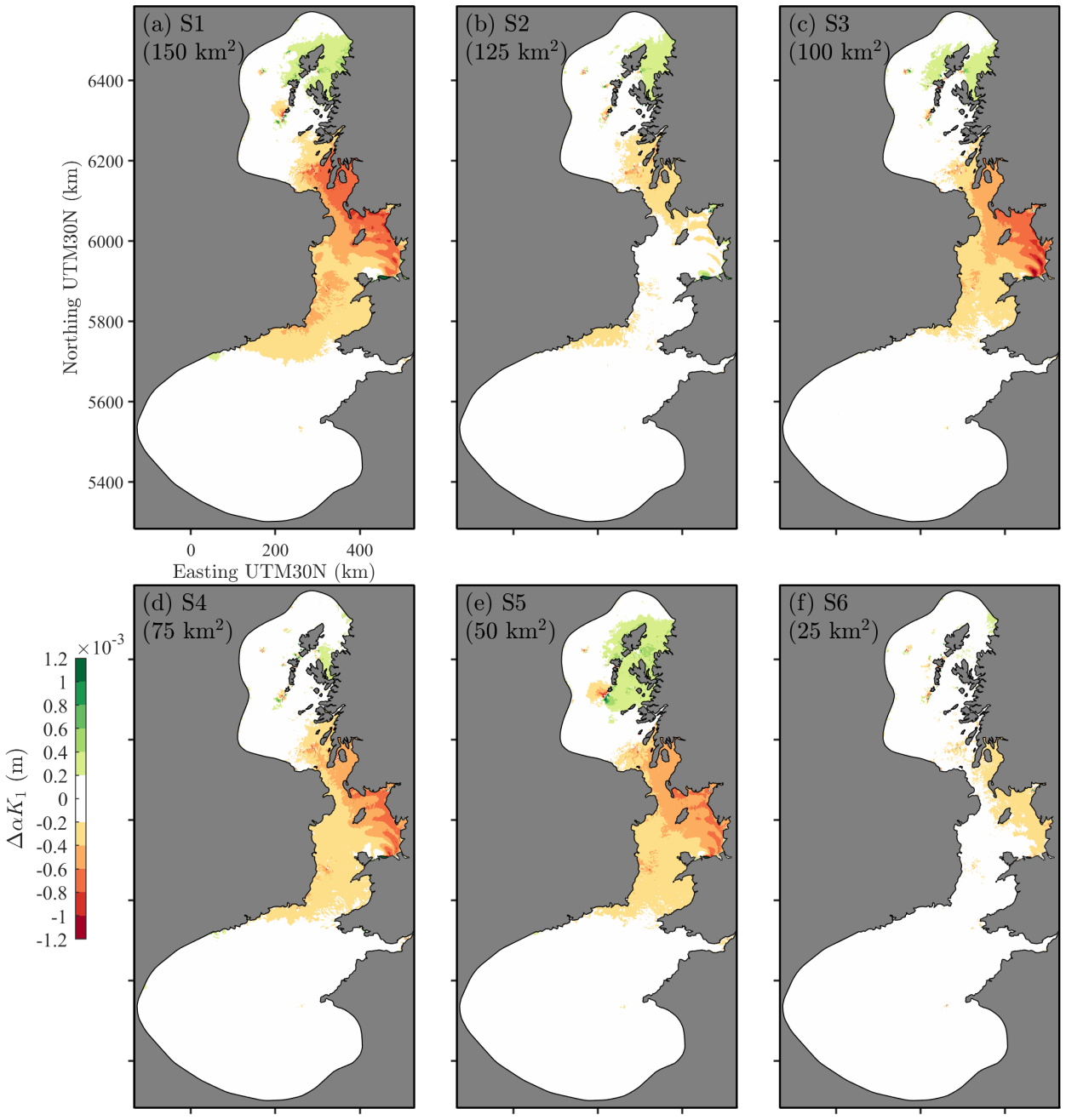

Figure 2.36: The predicted change in the amplitude of the K_1 constituent $\Delta\alpha_{K1}$ (m). Under each scenario (a) S1, (b) S2, (c) S3, (d) S4, (e) S5 and (f) S6, the results are interpolated to a 1×1 km grid for visualisation.

2.8.1 TELEMAC Steering File

/———————————————————————————-

/ GENERAL INFORMATIONS - OUTPUTS

/———————————————————————————-

GRAPHIC PRINTOUT PERIOD = 360

LISTING PRINTOUT PERIOD = 360

VALIDATION = NO

TIME STEP = 5

NUMBER OF TIME STEPS = 570240

MASS-BALANCE = YES

INFORMATION ABOUT SOLVER = YES

/———————————————————————————-

/ PARAMETERS SETTING

/———————————————————————————-

AIR PRESSURE = YES

LAW OF BOTTOM FRICTION =4

ROUGHNESS COEFFICIENT OF BOUNDARIES =0.030

FRICTION COEFFICIENT =0.030

BOTTOM SMOOTHINGS =1

TURBULENCE MODEL =3

CORIOLIS =YES

/———————————————————————————-

/ COORDINATES

/———————————————————————————-

SPHERICAL COORDINATES = YES

SPATIAL PROJECTION TYPE = 3

/———————————————————————————-

/ INITIAL CONDITIONS

/———————————————————————————-

INITIAL CONDITIONS = 'CONSTANT ELEVATION'

INITIAL ELEVATION = 0.0

/———————————————————————————-

/ BOUNDARY CONDITIONS

/———————————————————————————-

OPTION FOR TIDAL BOUNDARY CONDITIONS = 1;1

TIDAL DATA BASE = 2

MINOR CONSTITUENTS INFERENCE = YES

ORIGINAL DATE OF TIME = 2018;03;29

ORIGINAL HOUR OF TIME = 00;00;00

PRESCRIBED ELEVATIONS = 0;0

PRESCRIBED FLOWRATES = 0;0

PRESCRIBED VELOCITIES = 0;0

COEFFICIENT TO CALIBRATE TIDAL RANGE = 1.05

OPTION FOR LIQUID BOUNDARIES = 2;2

/———————————————————————————-

/ NUMERICAL PARAMETERS

/———————————————————————————-

DISCRETIZATIONS IN SPACE =12;11

CONTINUITY CORRECTION = YES

NUMBER OF PRIVATE ARRAYS =1

TREATMENT OF THE LINEAR SYSTEM =2

FINITE VOLUME SCHEME =0

SUPG OPTION =1;1;1;1

PARALLEL PROCESSORS =40

/———————————————————————————————-

/ ACCURACY AND SOLVERS

/———————————————————————————————-

TIDAL FLATS =YES

OPTION FOR THE TREATMENT OF TIDAL FLATS =1

TIDE GENERATING FORCE =NO

TREATMENT OF NEGATIVE DEPTHS =1

TREATMENT OF THE LINEAR SYSTEM =2

ACCURACY OF EPSILON =1.E-9

ACCURACY OF K =1.E-9

CONTINUITY CORRECTION =YES

C-U PRECONDITIONING =YES

INITIAL GUESS FOR H =1

INITIAL GUESS FOR U =1

MAXIMUM NUMBER OF ITERATIONS FOR K AND EPSILON =50

MAXIMUM NUMBER OF ITERATIONS FOR SOLVER =100

OPTION FOR THE SOLVER FOR K-EPSILON MODEL =2

PRECONDITIONING =2

PRECONDITIONING FOR K-EPSILON MODEL =2

SOLVER =3

SOLVER ACCURACY =1.E-6

SOLVER FOR K-EPSILON MODEL =1

SOLVER OPTION =2

/———————————————————————

/ NUMERICAL PARAMETERS, VELOCITY-CELERITY-HEIGHT

/———————————————————————

IMPLICITATION FOR DEPTH = 0.6

IMPLICITATION FOR VELOCITY = 0.6

Bibliography

Agency, I. E. (2009), *World energy outlook*, OECD/IEA Paris.

Aggidis, G. & Feather, O. (2012), 'Tidal range turbines and generation on the Solway Firth', *Renewable Energy* **43**, 9–17.

Agnew, D. (2010), '6 earth tides', *Treatise Geophys.* **3**, 163.

Ahmad, T. & Zhang, D. (2020), 'A critical review of comparative global historical energy consumption and future demand: The story told so far', *Energy Reports* **6**, 1973–1991.

Ahmadian, R., Falconer, R. & Lin, B. (2010), 'Hydro-environmental modeling of proposed Severn Barrage, UK', *Proceedings of the Institution of Civil Engineers-Energy* **163**(3), 107–117.

Angeloudis, A., Ahmadian, R., Bockelmann-Evans, B. & Falconer, R. (2015), 'Numerical modelling of a tidal lagoon along the North Wales coast', *Renewable energies offshore* pp. 139–145.

Angeloudis, A., Ahmadian, R., Falconer, R. A. & Bockelmann-Evans, B. (2016), 'Numerical model simulations for optimisation of tidal lagoon schemes', *Applied Energy* **165**, 522–536.

Angeloudis, A., Ahmadian, R., Falconer, R. & Bockelmann-Evans, B. (2015), Combined potential and impacts of tidal lagoons along the North Wales coast, *in* 'IAHR World Congress'.

Angeloudis, A. & Falconer, R. A. (2017), 'Sensitivity of tidal lagoon and barrage hydrodynamic impacts and energy outputs to operational characteristics', *Renewable Energy* **114**, 337–351.

Angeloudis, A., Falconer, R. A., Bray, S. & Ahmadian, R. (2016), 'Representation and operation of tidal energy impoundments in a coastal hydrodynamic model', *Renewable Energy* **99**, 1103–1115.

Angeloudis, A., Kramer, S. C., Hawkins, N. & Piggott, M. D. (2020), 'On the potential of linked-basin tidal power plants: An operational and coastal modelling assessment', *Renewable Energy* **155**, 876–888.

Apel, J. R. (1987), *Principles of ocean physics*, Academic Press.

Arnell, N. W., Lowe, J. A., Challinor, A. J. & Osborn, T. J. (2019), 'Global and regional impacts of climate change at different levels of global temperature increase', *Climatic Change* **155**, 377–391.

Aubrey, D. & Speer, P. (1985), 'A study of non-linear tidal propagation in shallow inlet/estuarine systems Part I: Observations', *Estuarine, coastal and shelf science* **21**(2), 185–205.

Baker, A. L., Craighead, R. M., Jarvis, E. J., Stenton, H. C., Angeloudis, A., Mackie, L., Avdis, A., Piggott, M. D. & Hill, J. (2020), 'Modelling the impact of tidal range energy on species communities', *Ocean & Coastal Management* **193**, 105221.

Baker, C. (1991), 'Tidal power', *Energy Policy* **19**(8), 792–797.

Barclay, V. M., Neill, S. P. & Angeloudis, A. (2023), 'Tidal range resource of the Patagonian Shelf', *Renewable Energy* **209**, 85–96.

Barre, D. S.-V. (1871), 'Theory of unsteady water flow, with application to river floods and to propagation of tides in river channels', *French Academy of Science* **73**, 148–154.

BBC (2018).

URL: *https://www.bbc.co.uk/news/uk-wales-south-west-wales-44589083*

BEIS (2023), 'Energy trends: UK electricity'. accessed 2023-04-16.

URL: *https://www.gov.uk/government/statistics/electricity-section-5-energy-trends*

Benton, T. G., Froggatt, A., Wellesley, L., Grafham, O., King, R., Morisetti, N., Schröder, P. et al. (2022), 'The Ukraine war and threats to food and energy security', *Chatham House—International Affairs Think Tank* **4**.

Bianchi, M., Chopin, F., Farme, T., Franz, N., Fuentevilla, C., Garibaldi, L. & Laurenti, A. (2014), 'FAO: the state of world fisheries and aquaculture', *Food and Agriculture Organization of the United Nations: Rome, Italy* pp. 1–230.

Blakely, C. P., Ling, G., Pringle, W. J., Contreras, M. T., Wirasaet, D., Westerink, J. J., Moghimi, S., Seroka, G., Shi, L., Myers, E. et al. (2022), 'Dissipation and bathymetric sensitivities in an unstructured mesh global tidal model', *Journal of Geophysical Research: Oceans* **127**(5), e2021JC018178.

BODC, C. (2017), 'UK tide gauge network data'.

Borthwick, A. G. (2016), 'Marine renewable energy seascape', *Engineering* **2**(1), 69–78.

Boßmann, T. & Staffell, I. (2015), 'The shape of future electricity demand: Exploring load curves in 2050s Germany and Britain', *Energy* **90**, 1317–1333.

Bowers, D., Gaffney, S., White, M. & Bowyer, P. (2002), 'Turbidity in the southern irish sea', *Continental Shelf Research* **22**(15), 2115–2126.

BP (2021), 'Statistical review of world energy 2021'.

Bray, S., Ahmadian, R. & Falconer, R. A. (2016), 'Impact of representation of hydraulic structures in modelling a Severn Barrage', *Computers & Geosciences* **89**, 96–106.

Breugem, W. A. (2022), Wetting and drying improvements in TELEMAC (part 1), *in* 'XXVIIIth TELEMAC User Conference', p. 35.

Brown, J. M., Norman, D. L., Amoudry, L. O. & Souza, A. J. (2016), 'Impact of operational model nesting approaches and inherent errors for coastal simulations', *Ocean Modelling* **107**, 48–63.

Brown, J. M., Souza, A. J. & Wolf, J. (2010), 'An 11-year validation of wave-surge modelling in the Irish Sea, using a nested POLCOMS–WAM modelling system', *Ocean modelling* **33**(1-2), 118–128.

Burrows, R., Yates, N., Hedges, T., Li, M., Zhou, J., Chen, D., Walkington, I., Wolf, J., Holt, J. & Proctor, R. (2009), Tidal energy potential in UK waters, *in* 'Proceedings of the Institution of Civil Engineers-maritime Engineering', Vol. 162, Thomas Telford Ltd, pp. 155–164.

Butikov, E. I. (2002), 'A dynamical picture of the oceanic tides', *American Journal of Physics* **70**(10), 1001–1011.

Byun, D.-S. & Hart, D. E. (2019), 'On robust multi-year tidal prediction using T_TIDE', *Ocean Science Journal* **54**, 657–671.

Carroll, B., Li, M., Pan, S., Wolf, J. & Burrows, R. (2009), Morphodynamic impacts of a tidal barrage in the Mersey Estuary, *in* 'Coastal Engineering 2008: (In 5 Volumes)', World Scientific, pp. 2743–2755.

Cartwright, D. & Tayler, R. (1971), 'New computations of the tide-generating potential', *Geophysical Journal International* **23**(1), 45–73.

Casotto, S. & Biscani, F. (2004), A fully analytical approach to the harmonic development of the tide-generating potential accounting for precession, nutation, and perturbations due to figure and planetary terms, *in* 'AAS/Division of Dynamical Astronomy Meeting# 35', Vol. 35, pp. 08–05.

Cazenave, P. W., Torres, R. & Allen, J. I. (2016), 'Unstructured grid modelling of offshore wind farm impacts on seasonally stratified shelf seas', *Progress in oceanography* **145**, 25–41.

Centre, C. H. (2010), 'Blue Kenue–reference manual.'.

Commission, S. D. et al. (2007), 'Turning the tide: Tidal power in the UK'.

Cornett, A., Cousineau, J. & Nistor, I. (2013), 'Assessment of hydrodynamic impacts from tidal power lagoons in the Bay of Fundy', *International Journal of Marine Energy* **1**, 33–54.

Coughlan, M., Guerrini, M., Creane, S., O'Shea, M., Ward, S. L., Van Landeghem, K. J., Murphy, J. & Doherty, P. (2021), 'A new seabed mobility index for the Irish Sea: Modelling seabed shear stress and classifying sediment mobilisation to help predict erosion, deposition, and sediment distribution', *Continental Shelf Research* **229**, 104574.

Cowell, P. J. & Thom, B. G. (1994), 'Morphodynamics of coastal evolution', *Coastal evolution: Late Quaternary shoreline morphodynamics* pp. 33–86.

Čož, N., Ahmadian, R. & Falconer, R. A. (2019), 'Implementation of a full momentum conservative approach in modelling flow through tidal structures', *Water* **11**(9), 1917.

Cronin, J., Anandarajah, G. & Dessens, O. (2018), 'Climate change impacts on the energy system: A review of trends and gaps', *Climatic change* **151**, 79–93.

Cummins, P. F. & Oey, L.-Y. (1997), 'Simulation of barotropic and baroclinic tides off northern British Columbia', *Journal of Physical oceanography* **27**(5), 762–781.

Dabrowski, T. & Hartnett, M. (2008), 'Modelling travel and residence times in the eastern Irish Sea', *Marine Pollution Bulletin* **57**(1-5), 41–46.

DataMap Wales (2022), 'DataMap Wales'. Accessed on January 16, 2024.
URL: *https://datamap.gov.wales*

Davies, A. G., Robins, P., Austin, M. & Walker-Springett, G. (2023), 'Exploring regional coastal sediment pathways using a coupled tide-wave-sediment dynamics model', *Continental Shelf Research* **253**, 104903.

Davies, A. & Robins, P. (2017), 'Residual flow, bedforms and sediment transport in a tidal channel modelled with variable bed roughness', *Geomorphology* **295**, 855–872.

de Haas, H., van Weering, T. C. & de Stigter, H. (2002), 'Organic carbon in shelf seas: Sinks or sources, processes and products', *Continental Shelf Research* **22**(5), 691–717.

De Laleu, V. (2009), La Rance Tidal Power Plant. 40-year operation feedback–lessons learnt, *in* 'BHA Annual conference.¡ www. british-hydro. org/downloads/La% 20Rance-BHA-Oct', Vol. 202009.

DeCastro, M., Salvador, S., Gómez-Gesteira, M., Costoya, X., Carvalho, D., Sanz-Larruga, F. & Gimeno, L. (2019), 'Europe, China and the United States: Three different approaches to the development of offshore wind energy', *Renewable and Sustainable Energy Reviews* **109**, 55–70.

Department for Business, E. & Strategy, I. (2020), 'National statistics: 2019 UK greenhouse gas emissions, provisional figures'.

Dronkers, J. (1986), 'Tidal asymmetry and estuarine morphology', *Netherlands Journal of Sea Research* **20**(2-3), 117–131.

Dronkers, J. J. (1964), 'Tidal computations in rivers and coastal waters'.

Dyer, K. R. & Huntley, D. A. (1999), 'The origin, classification and modelling of sand banks and ridges', *Continental shelf research* **19**(10), 1285–1330.

Egbert, G. D. & Erofeeva, S. Y. (2002), 'Efficient inverse modeling of barotropic ocean tides', *Journal of Atmospheric and Oceanic technology* **19**(2), 183–204.

Egbert, G. D. & Ray, R. D. (2000), 'Significant dissipation of tidal energy in the deep ocean inferred from satellite altimeter data', *Nature* **405**(6788), 775–778.

Egbert, G. D. & Ray, R. D. (2003), 'Semi-diurnal and diurnal tidal dissipation from TOPEX/Poseidon altimetry', *Geophysical Research Letters* **30**(17).

Elliott, K., Smith, H. C., Moore, F., van der Weijde, A. H. & Lazakis, I. (2018), 'Environmental interactions of tidal lagoons: A comparison of industry perspectives', *Renewable Energy* **119**, 309–319.

Elliott, K., Smith, H. C., Moore, F., van der Weijde, A. H. & Lazakis, I. (2019), 'A systematic review of transferable solution options for the environmental impacts of tidal lagoons', *Marine Policy* **99**, 190–200.

Engeland, K., Borga, M., Creutin, J.-D., François, B., Ramos, M.-H. & Vidal, J.-P. (2017), 'Space-time variability of climate variables and intermittent renewable electricity production – A review', *Renewable and Sustainable Energy Reviews* **79**, 600–617.

Estate, C. (2012), 'UK wave and tidal key resource areas project: Summary report', *Crown Estate: London, UK* .

Etemadi, A., Emami, Y., AsefAfshar, O. & Emdadi, A. (2011), 'Electricity generation by the tidal barrages', *Energy Procedia* **12**, 928–935.

Evans, P. & Langley, E. (2017), Impacts of a tidal lagoon on urban drainage and pollutant dispersion in a coastal embayment, *in* 'Proceedings of the 12th European Wave and Tidal Energy Conference, Cork, Ireland'.

Fahey, D., Doherty, S., Hibbard, K. A., Romanou, A. & Taylor, P. (2017), 'Physical drivers of climate change'.

Fairley, I., Ahmadian, R., Falconer, R. A., Willis, M. & Masters, I. (2014), 'The effects of a Severn Barrage on wave conditions in the Bristol Channel', *Renewable Energy* **68**, 428–442.

Falconer, R. A., Xia, J., Lin, B. & Ahmadian, R. (2009), 'The Severn Barrage and other tidal energy options: Hydrodynamic and power output modeling', *Science in China Series E: Technological Sciences* **52**(11), 3413–3424.

Franz, G., Delpey, M. T., Brito, D., Pinto, L., Leitão, P. & Neves, R. (2017), 'Modelling of sediment transport and morphological evolution under the combined action of waves and currents', *Ocean Science* **13**(5), 673–690.

Frau, J. P. (1993), 'Tidal energy: Promising projects: La Rance, a successful industrial-scale experiment', *IEEE Transactions on Energy Conversion* **8**(3), 552–558.

Fredsøe, J. (1993), 'Modelling of non-cohesive sediment transport processes in the marine environment', *Coastal Engineering* **21**(1-3), 71–103.

Garrett, C. & Greenberg, D. (1977), 'Predicting changes in tidal regime: The open boundary problem', *Journal of Physical Oceanography* **7**(2), 171–181.

Garrison, T. S. (2012), *Oceanography: An invitation to marine science*, Cengage Learning.

Gov, U. (2019), 'UK becomes first major economy to pass net zero emissions law, GOV. UK'.

Guinan, J., McKeon, C., O'Keeffe, E., Monteys, X., Sacchetti, F., Coughlan, M. & Nic Aonghusa, C. (2021), 'INFOMAR data supports offshore energy development and marine spatial planning in the Irish offshore via the EMODnet Geology portal', *Quarterly Journal of Engineering Geology and Hydrogeology* **54**(1), qjegh2020–033.

Guo, B. (2022), Hydro-environmental modelling and interaction of tidal lagoons around the UK coast, PhD thesis, Cardiff University.

Guo, B., Ahmadian, R., Evans, P. & Falconer, R. A. (2020), 'Studying the wake of an island in a macro-tidal estuary', *Water* **12**(5), 1225.

Guo, B., Ahmadian, R. & Falconer, R. A. (2021), 'Refined hydro-environmental modelling for tidal energy generation: West Somerset Lagoon case study', *Renewable Energy* **179**, 2104–2123.

Hadziabdic, P. & Rickards, L. (1999), 'Review of the Irish Sea (area 6) oceanography', *British Oceanographic Data Centre* pp. 1–135.

Haigh, I. D., Eliot, M. & Pattiaratchi, C. (2011), 'Global influences of the 18.61 year nodal cycle and 8.85 year cycle of lunar perigee on high tidal levels', *Journal of Geophysical Research: Oceans* **116**(C6).

Haines, A., Kovats, R. S., Campbell-Lendrum, D. & Corvalán, C. (2006), 'Climate change and human health: impacts, vulnerability and public health', *Public health* **120**(7), 585–596.

Hammons, T. J. (1993), 'Tidal power', *Proceedings of the IEEE* **81**(3), 419–433.

Hanousek, N. (2023), Numerical Modelling of Tidal Energy Devices and Structures as part of Net Zero, PhD thesis, Cardiff University.

Hanousek, N., Ahmadian, R. & Lesurf, E. (2023), 'Providing distributed electrical generation through retrofitting disused docks as tidal range energy schemes', *Renewable Energy* **217**, 119149.

Hendry, C. (2017), 'The role of tidal lagoons final report, 2016'.

Hervouet, J.-M. (2007), *Hydrodynamics of free surface flows: Modelling with the finite element method*, John Wiley & Sons.

Hicks, S. D. (2006), *Understanding tides*, US Department of Commerce, National Oceanic and Atmospheric Administration ....

Hillairet, P. & Weisrock, G. (1986), 'Optimizing production from the Rance Tidal Power Station.'.

Horrillo-Caraballo, J., Yin, Y., Fairley, I., Karunarathna, H., Masters, I. & Reeve, D. (2021), 'A comprehensive study of the tides around the Welsh coastal waters', *Estuarine, Coastal and Shelf Science* **254**, 107326.

Horsburgh, K., Hill, A., Brown, J., Fernand, L., Garvine, R. & Angelico, M. (2000), 'Seasonal evolution of the cold pool gyre in the western Irish Sea', *Progress in Oceanography* **46**(1), 1–58.

Howarth, M. (2005), Hydrography of the Irish Sea, *in* 'SEA6 Technical Report', Citeseer.

Hughes, S. A. (1993), *Physical models and laboratory techniques in coastal engineering*, Vol. 7, World Scientific.

Huthnance, J. (1980), 'On shelf-sea 'resonance'with application to Brazilian M3 tides', *Deep Sea Research Part A. Oceanographic Research Papers* **27**(5), 347–366.

IEA (2022), 'Renewables 2022'. License: CC BY 4.0.
URL: *https://www.iea.org/reports/renewables-2022*

IRENA, I. R. E. A. (2022), *Renewable power generation costs in 2020*, eBook Partnership.

IRENA, T. (2020), 'Renewable energy statistics 2022', *'* .

James, B., Roger, A. F., Christopher, E. & Reza, A. (2014), 'Physical and numerical modelling of the Severn Barrage', *Science China Technological Sciences* **57**, 1471–1481.

Jeffcoate, P. (2013), *Experimental and computational modelling of 3-D flow and bed shear stresses downstream from a multiple duct tidal barrage*, The University of Manchester (United Kingdom).

Jeffcoate, P., Stansby, P. & Apsley, D. (2017), 'Flow and bed-shear magnification downstream of a barrage with swirl generated in ducts by stators and rotors', *Journal of Hydraulic Engineering* **143**(2), 06016023.

Kadiri, M., Ahmadian, R., Bockelmann-Evans, B., Rauen, W. & Falconer, R. (2012), 'A review of the potential water quality impacts of tidal renewable energy systems', *Renewable and Sustainable Energy Reviews* **16**(1), 329–341.

Kelly, K., McManus, M. & Hammond, G. (2012), 'An energy and carbon life cycle assessment of tidal power case study: The proposed Cardiff–Weston Severn Barrage scheme', *Energy* **44**(1), 692–701.

Khojasteh, D., Lewis, M., Tavakoli, S., Farzadkhoo, M., Felder, S., Iglesias, G. & Glamore, W. (2022), 'Sea level rise will change estuarine tidal energy: A review', *Renewable and Sustainable Energy Reviews* **156**, 111855.

Kim, J. & Woo, S.-B. (2023), 'A numerical approach to the treatment of submerged water exchange processes through the sluice gates of a tidal power plant', *Renewable Energy* p. 119408.

Kvale, E. P. (2006), 'The origin of neap–spring tidal cycles', *Marine geology* **235**(1-4), 5–18.

Lane, S. N. (1998), 'Hydraulic modelling in hydrology and geomorphology: a review of high resolution approaches', *Hydrological processes* **12**(8), 1131–1150.

Langston, W., Jonas, P. & Millward, G. (2010), 'The Severn Estuary and Bristol Channel: A 25 year critical review', *Marine Pollution Bulletin* **61**(1-3), 1–4.

Leech, C. & Ahmadian, R. (2023), Hydro-environmental modelling of the impacts of turbine layout and design considerations of tidal range schemes, Technical report, Copernicus Meetings.

Lewis, M., Horsburgh, K., Bates, P. & Smith, R. (2011), 'Quantifying the uncertainty in future coastal flood risk estimates for the uk', *Journal of Coastal Research* **27**(5), 870–881.

Li, X., Li, M., McLelland, S. J., Jordan, L.-B., Simmons, S. M., Amoudry, L. O., Ramirez-Mendoza, R. & Thorne, P. D. (2017), 'Modelling tidal stream turbines in a three-dimensional wave-current fully coupled oceanographic model', *Renewable Energy* **114**, 297–307.

Li, Y., Wang, Y., Yao, W., Gao, W., Fukuda, H. & Zhou, W. (2023), 'Graphical decomposition model to estimate hourly global solar radiation considering weather stochasticity', *Energy Conversion and Management* **286**, 116719.

Logan, D. L. (2002), *A first course in the finite element method*, Vol. 4, Thomson.

Lyddon, C., Plater, A., Brown, J., Prime, T. & Wolf, J. (2015), 'The impact of tidal lagoons on future flood risk on the North Wirral and Conwy coastline, UK'.

MacDowell, V. (1997), 'Irish nautical almanac'.

Mackie, L., Coles, D., Piggott, M. & Angeloudis, A. (2020), 'The potential for tidal range energy systems to provide continuous power: A UK case study', *Journal of Marine Science and Engineering* **8**(10), 780.

Mackie, L., Kramer, S. C., Piggott, M. D. & Angeloudis, A. (2021), 'Assessing impacts of tidal power lagoons of a consistent design', *Ocean Engineering* **240**, 109879.

Macmillan, D. H. (1966), *Tides*, American Elsevier Publishing Company.

Mandiá, D. & Nissi, M. (2022), 'EU saw 53,000 excess deaths in july amid record heatwave: Report - national', *Reuters Global News* .

Masselink, G., Hughes, M. & Knight, J. (2014), *Introduction to coastal processes and geomorphology*, Routledge.

Masson-Delmotte, V., Zhai, P., Pirani, A., Connors, S. L., Péan, C., Berger, S., Caud, N., Chen, Y., Goldfarb, L., Gomis, M. et al. (2021), 'Climate change 2021: The physical science basis', *Contribution of working group I to the sixth assessment report of the intergovernmental panel on climate change* **2**.

McKay, W. & Pattenden, N. (1993), 'The behaviour of plutonium and americum in the shoreline waters of the Irish Sea: Further observations from time-trend matching of Sellafield radiocaesium', *Estuarine, Coastal and Shelf Science* **21**, 471–480.

Mettam, C. (1978), 'Environmental effects of tidal power generating schemes', *Hydrobiological Bulletin* **12**, 307–321.

Mewis, P. (1993), 'A quasi bubble-function approach for shallow water waves', *Advances in Hydro-Science and Engineering* **1**, 768–774.

Minchinton, W. E. (1979), 'Early tide mills: Some problems', *Technology and Culture* **20**(4), 777–786.

Murphy, D. (2005), 'Excavations of a mill at Killoteran, Co. Waterford as part of the N-25 Waterford By-Pass Project'.

Negahdari, M. R., Ghaedi, A., Nafar, M. & Mohsen, S. (2023), 'Optimal planning of the barrage type tidal power plants equipped to the hydro-pumps', *Electric Power Systems Research* **220**, 109347.

Neill, S. P. (2023), 'Wave resource characterization and co-location with offshore wind in the Irish Sea', *Renewable Energy* p. 119902.

Neill, S. P. (2024), The future of ocean renewable energy, *in* 'Living with Climate Change', Elsevier, pp. 449–464.

Neill, S. P., Angeloudis, A., Robins, P. E., Walkington, I., Ward, S. L., Masters, I., Lewis, M. J., Piano, M., Avdis, A., Piggott, M. D. et al. (2018), 'Tidal range energy resource and optimization–past perspectives and future challenges', *Renewable Energy* **127**, 763–778.

Neill, S. P. & Hashemi, M. R. (2018), *Fundamentals of ocean renewable energy: Generating electricity from the sea*, Academic Press.

Neill, S. P., Hashemi, M. R. & Lewis, M. J. (2016), 'Tidal energy leasing and tidal phasing', *Renewable Energy* **85**, 580–587.

Neill, S. P., Jordan, J. R. & Couch, S. J. (2012), 'Impact of tidal energy converter (tec) arrays on the dynamics of headland sand banks', *Renewable Energy* **37**(1), 387–397.

Neill, S. P., Robins, P. E. & Fairley, I. (2017), 'The impact of marine renewable energy extraction on sediment dynamics', *Marine Renewable Energy: Resource Characterization and Physical Effects* pp. 279–304.

Neill, S. P. & Scourse, J. D. (2009), 'The formation of headland/island sandbanks', *Continental Shelf Research* **29**(18), 2167–2177.

Nerem, R. S., Beckley, B. D., Fasullo, J. T., Hamlington, B. D., Masters, D. & Mitchum, G. T. (2018), 'Climate-change – driven accelerated sea-level rise detected in the altimeter era', *Proceedings of the national academy of sciences* **115**(9), 2022–2025.

Newell, R., Raimi, D. & Aldana, G. (2019), 'Global energy outlook 2019: The next generation of energy', *Resources for the Future* **1**, 8–19.

NOAA (2021), 'Monthly global climate report for annual', `https://www.ncei.noaa.gov/access/monitoring/monthly-report/global/202113`.

North Wales Tidal Energy, North Wales Presents A World-Class Site for A Tidal Lagoon (n.d.). (Date accessed 30/11/2023).

URL: *https://www.northwalestidalenergy.com/concept*

NWTE, N. W. T. E. (2013), 'North Wales presents a world-class site for a tidal lagoon'. Accessed on January 18, 2024.

URL: *https://www.northwalestidalenergy.com/about*

Olbert, A. I., Hartnett, M. & Dabrowski, T. (2010), 'Assessment of Tc-99 monitoring within the western Irish Sea using a numerical model', *Science of the total environment* **408**(17), 3671–3682.

Pappas, K., Mackie, L., Zilakos, I., van der Weijde, A. H. & Angeloudis, A. (2023), 'Sensitivity of tidal range assessments to harmonic constituents and analysis timeframe', *Renewable Energy* **205**, 125–141.

Pawlowicz, R., Beardsley, B. & Lentz, S. (2002), 'Classical tidal harmonic analysis including error estimates in matlab using T_TIDE', *Computers & Geosciences* **28**(8), 929–937.

Perkins, S. E. (2015), 'A review on the scientific understanding of heatwaves—their measurement, driving mechanisms, and changes at the global scale', *Atmospheric Research* **164**, 242–267.

Pethick, J. S., Morris, R. K. & Evans, D. H. (2009), 'Nature conservation implications of a Severn Tidal Barrage–A preliminary assessment of geomorphological change', *Journal for Nature Conservation* **17**(4), 183–198.

Petley, S. & Aggidis, G. (2016), 'Swansea Bay tidal lagoon annual energy estimation', *Ocean Engineering* **111**, 348–357.

Pingree, R. & Griffiths, D. (1979), 'Sand transport paths around the British Isles resulting from M2 and M4 tidal interactions', *Journal of the Marine Biological Association of the United Kingdom* **59**(2), 497–513.

Polton, J. A., Palmer, M. R. & Howarth, M. J. (2011), 'Physical and dynamical oceanography of Liverpool Bay', *Ocean Dynamics* **61**, 1421–1439.

Pope, J. O., Brown, K., Fung, F., Hanlon, H. M., Neal, R., Palin, E. J. & Reid, A. (2022), 'Investigation of future climate change over the British Isles using weather patterns', *Climate Dynamics* **58**(9-10), 2405–2419.

Prandle, D. (1984), 'Simple theory for designing tidal power schemes', *Advances in water resources* **7**(1), 21–27.

Procter, A., Zhang, F. & Maddy, J. (2022), Control of a tidal lagoon power generation hydrogen storage system, *in* '2022 UKACC 13th International Conference on Control (CONTROL)', IEEE, pp. 30–37.

Pugh, D. (1981), 'Tidal amphidrome movement and energy dissipation in the Irish Sea', *Geophysical Journal International* **67**(2), 515–527.

Pugh, D. T. (1987), 'Tides, surges and mean sea level'.

Pugh, D. T. (1996), 'Tides, surges and mean sea-level'.

Ramanathan, V. & Feng, Y. (2008), 'On avoiding dangerous anthropogenic interference with the climate system: Formidable challenges ahead', *Proceedings of the National Academy of Sciences* **105**(38), 14245–14250.

Raynaud, D., Hingray, B., François, B. & Creutin, J. D. (2018), 'Energy droughts from variable renewable energy sources in european climates', *Renewable Energy* **125**, 578–589.

Ritchie, H., Roser, M. & Rosado, P. (2022), 'Energy', *Our World in Data* . https://ourworldindata.org/energy.

Robins, P. E. & Davies, A. G. (2010), 'Morphological controls in sandy estuaries: The influence of tidal flats and bathymetry on sediment transport', *Ocean Dynamics* **60**, 503–517.

Robins, P. E., Neill, S. P., Lewis, M. J. & Ward, S. L. (2015), 'Characterising the spatial and temporal variability of the tidal-stream energy resource over the northwest european shelf seas', *Applied Energy* **147**, 510–522.

Robinson, I. (1979), 'The tidal dynamics of the Irish and Celtic Seas', *Geophysical Journal International* **56**(1), 159–197.

Rogelj, J., Den Elzen, M., Höhne, N., Fransen, T., Fekete, H., Winkler, H., Schaeffer, R., Sha, F., Riahi, K. & Meinshausen, M. (2016), 'Paris Agreement climate proposals need a boost to keep warming well below 2 c', *Nature* **534**(7609), 631–639.

Ross, D. A. (1977), 'Introduction to oceanography', *(No Title)* .

Rourke, F. O., Boyle, F. & Reynolds, A. (2010), 'Tidal energy update 2009', *Applied energy* **87**(2), 398–409.

Schiermeier, Q. (2010), 'The real holes in climate science: Like any other field, research on climate change has some fundamental gaps, although not the ones typically claimed by sceptics. Quirin Schiermeier takes a hard look at some of the biggest problem areas', *Nature* **463**(7279), 284–288.

Schmidt, O., Melchior, S., Hawkes, A. & Staffell, I. (2019), 'Projecting the future levelized cost of electricity storage technologies', *Joule* **3**(1), 81–100.

Segura, E., Morales, R., Somolinos, J. & López, A. (2017), 'Techno-economic challenges of tidal energy conversion systems: Current status and trends', *Renewable and Sustainable Energy Reviews* **77**, 536–550.

Shmelev, S. E. & Van Den Bergh, J. C. (2016), 'Optimal diversity of renewable energy alternatives under multiple criteria: An application to the UK', *Renewable and Sustainable Energy Reviews* **60**, 679–691.

Simpson, J. H. & Sharples, J. (2012), *Introduction to the physical and biological oceanography of shelf seas*, Cambridge University Press.

Soulsby, R. (1997), 'Dynamics of marine sands'.

Speer, P. & Aubrey, D. (1985), 'A study of non-linear tidal propagation in shallow inlet/estuarine systems Part II: Theory', *Estuarine, Coastal and Shelf Science* **21**(2), 207–224.

Sverdrup, K. A., Duxbury, A. & Duxbury, A. C. (2006), 'Fundamentals of oceanography', *(No Title)* .

Taveira-Pinto, F., Rosa-Santos, P. & Fazeres-Ferradosa, T. (2020), 'Marine renewable energy'.

Todeschini, G. (2017), 'Review of tidal lagoon technology and opportunities for integration within the UK energy system', *Inventions* **2**(3), 14.

Toffoli, A. & Bitner-Gregersen, E. M. (2017), 'Types of ocean surface waves, wave classification', *Encyclopedia of maritime and offshore engineering* pp. 1–8.

Tousif, S. M. R. & Taslim, S. M. B. (2011), 'Tidal power: An effective method of generating power', *International Journal of Scientific & Engineering Research* **2**(5), 1–5.

Twidell, J. (2021), *Renewable energy resources*, Routledge.

Van Rijn, L. (2013), 'Simple general formulae for sand transport in rivers, estuaries and coastal waters', *Retrieved from www. leovanrijn-sediment. com* pp. 1–16.

Vollset, S. E., Goren, E., Yuan, C.-W., Cao, J., Smith, A. E., Hsiao, T., Bisignano, C., Azhar, G. S., Castro, E., Chalek, J. et al. (2020), 'Fertility, mortality, migration, and population scenarios for 195 countries and territories from 2017 to 2100: A forecasting analysis for the global burden of disease study', *The Lancet* **396**(10258), 1285–1306.

Vouriot, C. V., Angeloudis, A., Kramer, S. C. & Piggott, M. D. (2019), 'Fate of large-scale vortices in idealized tidal lagoons', *Environmental Fluid Mechanics* **19**, 329–348.

Vreugdenhil, C. B. (1994), *Numerical methods for shallow-water flow*, Vol. 13, Springer Science & Business Media.

Wakelin, S., Woodworth, P., Flather, R. & Williams, J. (2003), 'Sea-level dependence on the NAO over the NW European Continental Shelf', *Geophysical Research Letters* **30**(7).

Wang, Z. B. (1989), Mathematical modelling of morphological processes in estuaries, PhD thesis, Technische Universiteit Delft.

Wang, Z. B., Jeuken, M., Gerritsen, H., De Vriend, H. & Kornman, B. (2002), 'Morphology and asymmetry of the vertical tide in the Westerschelde Estuary', *Continental Shelf Research* **22**(17), 2599–2609.

Wang, Z. & Wang, Z. (2019), A review on tidal power utilization and operation optimization, *in* 'IOP Conference Series: Earth and Environmental Science', Vol. 240, IOP Publishing, p. 52015.

Waters, S. & Aggidis, G. (2016*a*), 'Tidal range technologies and state of the art in review', *Renewable and Sustainable Energy Reviews* **59**, 514–529.

Waters, S. & Aggidis, G. (2016*b*), 'A world first: Swansea Bay tidal lagoon in review', *Renewable and Sustainable Energy Reviews* **56**, 916–921.

Wave and Tidal Energy: Part of the UK's Energy Mix (n.d.).
URL: *https://www.gov.uk/guidance/wave-and-tidal-energy-part-of-the-uks-energy-mix-tidal-range-potential*

Wessel, P. & Smith, W. H. (1996), 'A global, self-consistent, hierarchical, high-resolution shoreline database', *Journal of Geophysical Research: Solid Earth* **101**(B4), 8741–8743.

Wright, L. D. (1995), 'Morphodynamics of inner continental shelves', *(No Title)* .

Xia, J., Falconer, R. A. & Lin, B. (2010), 'Impact of different operating modes for a Severn Barrage on the tidal power and flood inundation in the Severn Estuary, UK', *Applied Energy* **87**(7), 2374–2391.

Xue, J. (2021), Optimisation of tidal range schemes, PhD thesis, Cardiff University.

Xue, J., Ahmadian, R. & Falconer, R. A. (2019), 'Optimising the operation of tidal range schemes', *Energies* **12**(15), 2870.

Xue, J., Ahmadian, R. & Jones, O. (2020), 'Genetic algorithm in tidal range schemes' optimisation', *Energy* **200**, 117496.

Xue, J., Ahmadian, R., Jones, O. & Falconer, R. A. (2021), 'Design of tidal range energy generation schemes using a Genetic Algorithm model', *Applied Energy* **286**, 116506.

Xuemin, C. (1985), 'Tidal power in China', *Water Power and Dam Construction* **37**, 33–6.

Yates, M. L. (2019), Coastal Wave Hydrodynamics and Morphological Evolution, PhD thesis, Université Paris-Est.

Yates, N., Walkington, I., Burrows, R. & Wolf, J. (2013*a*), 'Appraising the extractable tidal energy resource of the UK's western coastal waters', *Philosophical Transactions of the Royal Society A: Mathematical, Physical and Engineering Sciences* **371**(1985), 20120181.

Yates, N., Walkington, I., Burrows, R. & Wolf, J. (2013*b*), 'The energy gains realisable through pumping for tidal range energy schemes', *Renewable Energy* **58**, 79–84.

Zhang, T., Hanousek, N., Qadrdan, M. & Ahmadian, R. (2022), 'A day-ahead scheduling model of power systems incorporating multiple tidal range power stations', *IEEE Transactions on Sustainable Energy* **14**(2), 826–836.

Zhang, W., Cao, Y., Zhu, Y., Zheng, J., Ji, X., Xu, Y., Wu, Y. & Hoitink, A. (2018), 'Unravelling the causes of tidal asymmetry in deltas', *Journal of Hydrology* **564**, 588–604.

Zhou, J., Falconer, R. A. & Lin, B. (2014), 'Refinements to the EFDC model for predicting the hydro-environmental impacts of a barrage across the Severn Estuary', *Renewable Energy* **62**, 490–505.

Zhou, J., Pan, S. & Falconer, R. A. (2014*a*), 'Effects of open boundary location on the far-field hydrodynamics of a Severn Barrage', *Ocean Modelling* **73**, 19–29.

Zhou, J., Pan, S. & Falconer, R. A. (2014*b*), 'Optimization modelling of the impacts of a Severn Barrage for a two-way generation scheme using a Continental Shelf model', *Renewable Energy* **72**, 415–427.